

2012

Vertical Field Switching Blue Phase Liquid Crystals For Field Sequential Color Displays

Hui-Chuan Cheng
University of Central Florida

 Part of the [Electromagnetics and Photonics Commons](#), and the [Optics Commons](#)

Find similar works at: <https://stars.library.ucf.edu/etd>

University of Central Florida Libraries <http://library.ucf.edu>

This Doctoral Dissertation (Open Access) is brought to you for free and open access by STARS. It has been accepted for inclusion in Electronic Theses and Dissertations, 2004-2019 by an authorized administrator of STARS. For more information, please contact STARS@ucf.edu.

STARS Citation

Cheng, Hui-Chuan, "Vertical Field Switching Blue Phase Liquid Crystals For Field Sequential Color Displays" (2012). *Electronic Theses and Dissertations, 2004-2019*. 2462.
<https://stars.library.ucf.edu/etd/2462>

VERTICAL FIELD SWITCHING BLUE PHASE LIQUID CRYSTALS FOR FIELD SEQUENTIAL COLOR DISPLAYS

by

HUI-CHUAN CHENG

B.S. National Taiwan University, Taiwan, 2000

M.S. National Taiwan University, Taiwan, 2005

A dissertation submitted in partial fulfillment of the requirements
for the degree of Doctor of Philosophy
in the College of Optics and Photonics
at the University of Central Florida
Orlando, Florida

Fall Term
2012

Major Professor: Shin-Tson Wu

©2012 Hui-Chuan Cheng

ABSTRACT

Low power consumption is a critical requirement for all liquid crystal display (LCD) devices. A field sequential color (FSC) LCD was proposed by using red (R), green (G) and blue (B) LEDs and removing the lossy component of color filters which only transmits ~30% of the incoming white light. Without color filters, FSC LCDs exhibit a ~3X higher optical efficiency and 3X higher resolution density as compared to the conventional color filters-based LCDs. However, color breakup (CBU) is a most disturbing defect that degrades the image quality in FSC displays. CBU can be observed in stationary or moving images. It manifests in FSC LCDs when there is a relative speed between the images and observers' eyes, and the observer will see the color splitting patterns or rainbow effect at the boundary between two different colors.

In Chapter 2, we introduce a five-primary display by adding additional yellow(Y) and cyan(C) colors. From the analysis and simulations, five primaries can provide wide color gamut and meanwhile the white brightness is increased, as compared to the three-primary. Based on the five-primary theorem, we propose a method to reduce CBU of FSC LCDs by using RGBYC LEDs instead of RGB LEDs in the second section. Without increasing the sub-frame rate as three-primary LCDs, we can reduce the CBU by utilizing proper color sequence and weighting ratios. In addition, the color gamut achieves 140% NTSC and the white brightness increases by more than 13%, as compared to the three-primary FSC LCDs.

Another strategy to suppress CBU is using higher field frequency, such as 540 Hz or even up to 1000 Hz. However, this approach needs liquid crystals with a very fast response time (<1 ms). Recently, the polymer-stabilized blue-phase liquid crystal (PS-BPLC) draws great attentions

because of improved temperature range which enables the applications for photonic devices and displays. PS-BPLC is a good candidate for FSC LCDs because of its submillisecond gray-to-gray response time, no need for alignment layer, and isotropic dark state. So far, almost all the BPLC devices utilize planar or protruded in-plane switching (IPS) electrode configuration. The structure of planar IPS is relatively simple, but the operating voltage is too high for thin-film transistor (TFT) addressing. Moreover, high voltage causes deformation of polymer network and induces a noticeable hysteresis. Protruded IPS is helpful for lowering the operating voltage, but the manufacturing process becomes more sophisticated.

In Chapter 3, we propose a vertical field switching (VFS) mode for blue phase LCDs. The simple structure of VFS cell generates uniform vertical fields on the BPLC materials. From our experimental results, the operation voltage can be reduced to $\sim 10V_{\text{rms}}$ while eliminating the hysteresis. We also defined a critical field below which hysteresis does not occur. Above critical field, lattice distortion and other irreversible phase transition processes would occur. As a result, the associated response time would be slower. Therefore, VFS mode also shows faster response time than IPS mode. The operating voltage can be further reduced by choosing an optimized cell gap and a larger oblique incident angle in VFS blue phase LCDs.

In Chapter 4, we propose several compensation mechanisms to improve the viewing angle of VFS blue-phase LCDs. The compensation principles are analyzed and simulation results evaluated. Because VFS blue-phase LCD processes several advantages over IPS blue-phase LCD and conventional LCDs, it could become a strong contender for next-generation display technology.

ACKNOWLEDGMENTS

I would like to express my gratitude to those who have made contributions to this work and who have offered help during my study and research.

Thank my advisor Prof. Shin-Tson Wu for his guidance, encouragement, and patience in the past few years. I also appreciate all the help from Prof. Wu's wife. The time staying in Orlando has become the best memory in my life.

I am grateful to my committee members Prof. Patrick L. LiKamWa, Prof. Winston V. Schoenfeld, and Prof. Thomas X. Wu for their support and valuable comments.

I would also like to thank my outstanding colleagues in the photonics and display group for their discussions, inspirations, and assistance in my research. I treasure the opportunity to work in such a great family led by Prof. Wu.

Moreover, I would like to thank Chi-Mei Optoelectronics (CMO) (Taiwan), Industrial Technology Research Institute (ITRI) (Taiwan), and AU Optronics (AUO) (Taiwan) for their financial support of my research at University of Central Florida.

Finally and most importantly, I want to thank my parents and sister in Taiwan for their support and the love they have shown all throughout my life.

TABLE OF CONTENTS

LIST OF FIGURES	viii
LIST OF TABLES	xii
CHAPTER 1: MULTI-PRIMARY COLOR DISPLAY	1
1.1 Introduction of Liquid Crystal Display	1
1.2 Multi-Primary Colors	4
1.2.1 Introduction.....	4
1.2.2 Principles and Simulations.....	5
1.3 Five-Primary LCDs and Comparison.....	13
1.4 Summary	18
CHAPTER 2: FIELD SEQUENTIAL COLOR DISPLAY	19
2.1 Introduction	19
2.2 Color Breakup	20
2.3 Multi-Primary FSC LCDs	22
2.4 Discussions and Conclusions	35
CHAPTER 3: BLUE PHASE LIQUID CRYSTAL DISPLAYS	37
3.1 Blue Phase Liquid Crystal.....	37
3.1.1 Introduction.....	37
3.1.2 Planar In-Plane Switching BPLCD.....	39

3.2	Reducing Voltage for Blue Phase Liquid Crystal Display	41
3.3	Vertical Field Switching BPLCD	44
3.3.1	Device Structure.....	44
3.3.2	Experiments and Simulations	48
3.4	Summary	61
CHAPTER 4: WIDE VIEWING ANGLE OF VFS BPLCD.....		62
4.1	Light Leakage in VFS BPLCD	62
4.2	Film Compensation Principles	65
4.3	Wire-Grid Polarizer for VFS BPLCDs.....	82
4.4	E-type Analyzer for VFS BPLCDs	85
4.5	Discussions.....	88
CHAPTER 5: SUMMARY		89
LIST OF REFERENCES		92
LIST OF PUBLICATIONS.....		101

LIST OF FIGURES

Figure 1.1 Device structure of a transmissive TFT LCD pixel with RGB sub-pixels.....	2
Figure 1.2 Color gamut triangles with a different green primary.	6
Figure 1.3 Transmission spectra of (a) conventional RGB color filters and (b) five-primary RGBYC color filters we developed.	7
Figure 1.4 Emission spectra of a conventional CCFL and WG CCFL.	8
Figure 1.5 Simulated color gamut of RGB (dashed lines) and RGBYC (solid lines) primaries using a MVA LCD.	9
Figure 1.6 Image analysis for gray level distributions. (a) A fruit basket, (b) Lotus in a pond, and (c) a pasture and sky.....	13
Figure 1.7 Photos from a 32" MVA LCD TV prototype. Left column: five-primary (RGBYC); right column: conventional RGB primaries. Backlight: CCFL in both systems.	14
Figure 1.8 Measured data for the RGB and RGBYC MVA LCD TVs.	15
Figure 1.9 Simulated color gamut of RGBYC-primary with conventional CCFL (dashed lines) and RGBYC with WG CCFL (solid lines) in a MVA LCD.	17
Figure 2.1 Optical transmittance of each component in LCDs.....	19
Figure 2.2 Working principle of the field-sequential-color display.	20
Figure 2.3 The reason of color breakup.	21
Figure 2.4 Rainbow effect caused by color breakup.....	21
Figure 2.5 Two-dimension time and location diagram. The upper parts of each diagram represent the moving white objects with width of W pixels. The lower parts are simplified CBU patterns	

without considering the brightness variation. The slant dashed arrows show the eyes tracking along the movement of object.....	24
Figure 2.6 Simulated CBU for three-primary display. (a) White object, (b) Frame rate = 540Hz, (c) Frame rate = 180Hz, (d) Frame rate = 60Hz.	24
Figure 2.7 LED spectra and luminance intensities. (Ref. Nichia Co.).....	26
Figure 2.8 MacAdam Limit boundaries for the CIE 1931 color space chromaticity diagram.	27
Figure 2.9 Simulated CBU with different color appearing sequence.	28
Figure 2.10 Simulated CBU with different color weighting ratios.....	29
Figure 2.11 Simulated CBU of yellow and cyan objects.....	31
Figure 2.12 Simulated CBU of two arbitrary colors. The bottom figures show compressed CBU after adjusting the color weighting ratios.....	32
Figure 2.13 Color coordinates and gamut for five-primary LCDs.	33
Figure 3.1 Double-twist alignment of LC molecules and cubic structure.	38
Figure 3.2 Operation principle of a planar IPS BPLCD between crossed polarizers: (a) $E=0$, and (b) $E>0$	40
Figure 3.3 Device structure of the proposed VFS-BPLCD.	45
Figure 3.4 Structures of (a) bottom coupling film, (b) top coupling film, (c) turning film with regular-angle prisms, and (d) turning film with round-shape prisms.	48
Figure 3.5 Experimental setup for characterizing the VFS cell.....	49
Figure 3.6 Measured VT curves and hysteresis of IPS and VFS cells. $\lambda=633$ nm.	50
Figure 3.7 Measured phase retardation vs. electric field intensity under different applied voltages. $\lambda=633$ nm.	52

Figure 3.8 Measured response time of (a) IPS cell and (b) VFS cell. $\lambda=633$ nm.	53
Figure 3.9 Simulated VT curves under different cell gap ($d=1\mu\text{m}$, $2\mu\text{m}$, and $5\mu\text{m}$) for the VFS cell. Incident angle= 70° and $\lambda=550\text{nm}$	56
Figure 3.10 Simulated operating voltage vs. cell gap at different incident angles of VFS cells. $\lambda=550$ nm and Kerr constant is assumed to be $K\sim 7.5\text{nm/V}^2$	58
Figure 3.11 Simulated operating voltage vs. cell gap at different Kerr constants.	59
Figure 3.12 Possible crosstalk in a VFS BP-LCD.	60
Figure 4.1 Directional backlight's angular distribution.	63
Figure 4.2 Polar coordinate of the VFS-BPLCD.	63
Figure 4.3 Change in the effective angle between the polarizer and the analyzer: (a) normal observation ($\theta=0^\circ$), (b) oblique observation ($\theta=70^\circ$); (c) simulated isocontrast contours.	65
Figure 4.4 Biaxial film-compensated VFS BPLCD: (a) device configuration, (b) compensation principle on Poincare sphere, and simulated isocontrast contours at incident angle $\theta=70^\circ$ (c) and $\theta=60^\circ$ (d). $\lambda=550$ nm.....	68
Figure 4.5 Simulated isocontrast contours of biaxial film-compensated VFS BPLCD: (a) $\phi=40^\circ$ and -40° and (b) $\phi=30^\circ$ and -30°	70
Figure 4.6 Isocontrast contours and film configurations of a VFS BPLCD with incident angle $\theta=60^\circ$	71
Figure 4.7 Optical configuration of the proposed VFS BPLCD: (a) film configuration, (b) compensation principle, and (c) isocontrast contours.....	72
Figure 4.8 Optical configuration of a VFS BPLCD with 4 biaxial films: (a) film configuration, (b) compensation principle, and simulated isocontrast contours at $\theta=70^\circ$ (c) and $\theta=60^\circ$ (d).....	74

Figure 4.9 Biaxial and A/C-films compensated VFS BPLCD: (a) film configuration, (b) compensation principle, and (c) simulated isocontrast contours.	77
Figure 4.10 Film-compensated VFS BPLCD with bottom coupling film laminated to the polarizer: (a) film configuration, (b) compensation principle, and (c) simulated isocontrast contours.	79
Figure 4.11 Another version of biaxial and A/C-films compensated VFS BPLCD: (a) film configuration, (b) compensation principle, and (c) simulated isocontrast contours.	81
Figure 4.12 Schematic drawing of a wire-grid polarizer.	82
Figure 4.13 Optical configuration of the proposed VFS-BPLCD, (a) film configuration, (b) compensation principle, and (c) simulated isocontrast contours.	84
Figure 4.14 Schematic drawing of an (a) O-type polarizer and (b) E-type polarizer.	85
Figure 4.15 Proposed VFS BPLCD using an O-type polarizer and an E-type analyzer: (a) film configuration, (b) compensation principle, and (c) simulated isocontrast contours.	87

LIST OF TABLES

Table 1.1 Simulated results on the brightness and color coordinates of 3- and 5-primary LCDs. .	9
Table 1.2 Measured data for RGB and RGBYC displays.....	15
Table 1.3 Performance comparison of wide-gamut CCFL, RGB LEDs and our five-primary LCDs.	16
Table 1.4 Simulation results on display brightness and color coordinates of our 5-primary MVA LCD using conventional CCFL and WG CCFL.	17
Table 2.1 Color ratios for standard illuminant D65	26
Table 2.2 Color ratios and color shift in IPS mode LCDs	30
Table 2.3 The required LED numbers for showing white color (CIE illuminant D65).....	34

CHAPTER 1: MULTI-PRIMARY COLOR DISPLAY

1.1 Introduction of Liquid Crystal Display

Liquid crystal (LC) was first discovered by an Austrian botanical physiologist, Friedrich Reinitzer, in 1888. LCs can flow as liquids and have optical birefringence as crystals. In addition, LCs could interact with electric or optical field. Therefore, LCs have been widely used in electro-optic and optical devices.

Among all the applications of liquid crystals, displays are most pervasive. The active matrix liquid crystal displays (LCDs) have thin profile, lightweight, low power consumption, and high resolution, and have successfully displaced cathode ray tubes. A revolution for portable electronic devices has started. Nowadays, LCDs are widely used in our daily lives, such as smartphones, laptops, monitors, televisions, projectors, instrument panels, and signage, etc. So far, this field has grown into a 100-billion dollar industry [1] [2].

Figure 1.1 shows a typical structure of a transmissive TFT LCD. A LCD panel is comprised of a backlight module and a cell module. Generally, a LC cell is formed between two glass substrates and plural pixels with switching thin-film-transistors (TFTs) are formed on the inner surface of the bottom substrate to provide driving voltages. The LC cell is further sandwiched between two crossed linear polarizers, which together function as a spatial light modulator to control the light transmittance in order to obtain different gray levels [3].

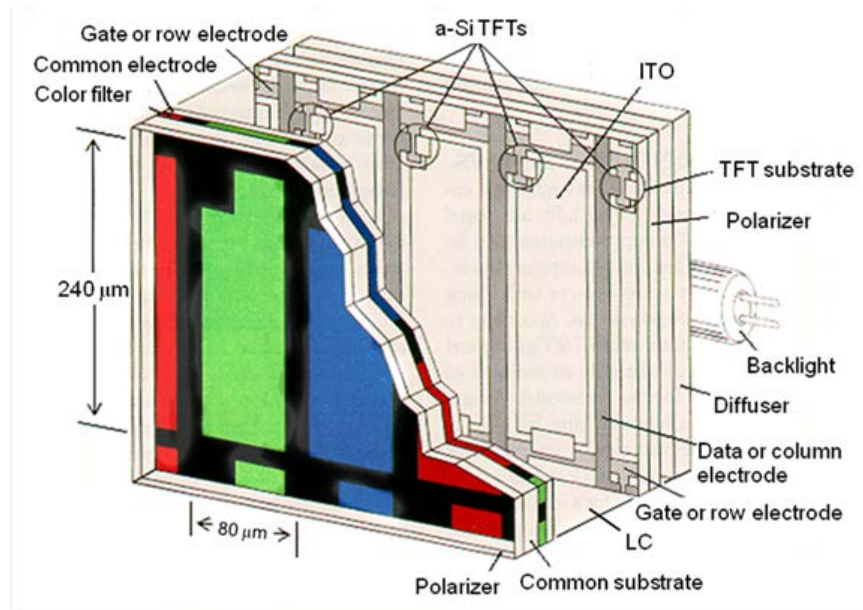


Figure 1.1 Device structure of a transmissive TFT LCD pixel with RGB sub-pixels.

In most LCD devices, nematic LC material is commonly employed because of its good physical and optical properties, e.g., simple alignment, natural grayscales, high contrast, and reasonably fast response time. The nematic LC molecules have no positional order, but they have certain long-range orientational order, thus macroscopically they behave like a uniaxial crystal. In recent years, the nematic-based LCD technology has advanced dramatically in many aspects like wide viewing angle using optical compensation films, vivid color using LED light sources, high contrast ratio using dynamic backlight, low power consumption using backlight recycling techniques, and fast response time using low viscosity LC materials and thinner cell gap fabrication techniques.

Presently, the gray-to-gray response time of a nematic LCD is about 5 ms which is still inadequate for motion-blur-free picture qualities. To reduce motion blurs, high frequency frame

refreshing technique such as 240 Hz or even 480 Hz refreshing rate is emerging and is expected to dominate in the near future for flat-panel LCD TVs. For 480 Hz refreshing rate, the preferred gray-to-gray response time should be less than 2 ms. The LC response time is proportional to the square of the cell gap employed. The state-of-the-art cell gap of LCD TV is around 3.5 μm . Reducing the cell gap to below 3- μm would improve the response time, but the fabrication yield is compromised. In other words, the response time using a nematic LC material is approaching to its physical limit.

The inadequate LC response time also limits the widespread applications of field sequential color (FSC) displays where spatial color filters can be removed so that the light efficiency and resolution density are tripled. In addition, nematic LC materials require surface treatment, such as rubbing the polyimide (PI) layer, in order to produce a uniform pretilt angle and strong anchoring energy. Moreover, the alignment treatment of nematic LCs will also reduce the contrast ratio of the display. For example, in a LCD using a homogeneous alignment like those in an IPS (in-plane-switching) [4] [5] or FFS (fringe-field-switching) cell [6], surface rubbing is needed and the alignment surface will have many micro rubbing grooves. In practice, these grooves are not easy to be controlled uniformly, which in turn cause irregular alignments near the surface. Because the nematic LC materials are uniaxial, certain light leakage will occur even the LC molecules are aligned a little bit off from the designed direction. Therefore, a new LC material that does not require surface alignment layer like the nematic material is highly preferred.

In summary, a new LC material with fast response time to enable FSC LCDs and no alignment layer needed for easier fabrications would be important for next-generation LCDs.

1.2 Multi-Primary Colors

1.2.1 Introduction

For most LCDs, wide viewing angle, high contrast ratio, fast response time, high brightness, low power consumption, and wide color gamut are important metrics. Recently, dramatic progress in LCD performance has been made in all aspects. The demand for a higher color gamut is ever increasing. Since the natural objects and cinema are significantly more colorful than the CRT TV standard, there is an urgent need to produce wider color gamut in order to reproduce the original colors with high fidelity.

In a conventional three-primary [i.e., red (R), green (G), and blue (B)] LCD with CCFL (cold cathode fluorescent lamp) as backlight, its color gamut is ~72% NTSC, which is comparable to a CRT but inferior to a plasma display (~95%). Several backlight related technologies have been developed for enhancing the color gamut of LCDs. 1) Laser diodes [7]. Although laser diodes provide very pure primary colors, there are still no perfect solutions for the speckle pattern produced by interference [8]. 2) RGB light emitting diodes (LEDs) [9]. Due to a relatively narrow bandwidth of LEDs, the color gamut as wide as ~120% has been achieved [10], [11]. A slim LCD TV using edge-lit LED has been recently introduced to commercial products. However, the heat sink design, lifetime of each color, and cost are still the major concerns. 3) Wide gamut CCFL (WG CCFL) [12] is also under development by many manufacturers, but it is not yet widely adopted because of the shorter lifetime and lower optical efficiency.

Another strategy for widening color gamut is to use more saturated RGB color filters (CFs). However, this approach suffers a drastic decrease in optical efficiency because the

employed CFs have a narrower transmission bandwidth which leads to a lower transmittance.

Using multi-primary colors (more than RGB) to widen the color gamut has been demonstrated in projection displays [13] and some direct-view LCDs [14] [15] [16] [17]. However, the display brightness is reduced and cost increased because of increased number of color pixels and fabrication complications.

We propose a practical five-primary technique that not only widens the color gamut but also increases the white brightness. We will first discuss the operation principles, and show some simulation and confirming results using a 32" LCD TV with five-primary colors (RGB plus yellow and cyan).

1.2.2 Principles and Simulations

As abovementioned, we can use highly saturated RGB color filters to enlarge the color gamut. However, this method reduces display brightness dramatically because of the lower transmittance of each color. Thus, it is not a preferred approach from the energy saving viewpoint. Figure 1.2 depicts the color gamut curves of LCDs using two types of RGB primaries but at a different green primary. As shown by the dotted triangle, if we want to get good coverage of yellow then we cannot display a vivid cyan. On the contrary, if we shift the green point to cover more cyan, then we lose the fidelity of yellow, as the solid triangle shows. Therefore, using three primaries is not practical to get high brightness and wide color gamut (i.e. good color reproduction) as well.

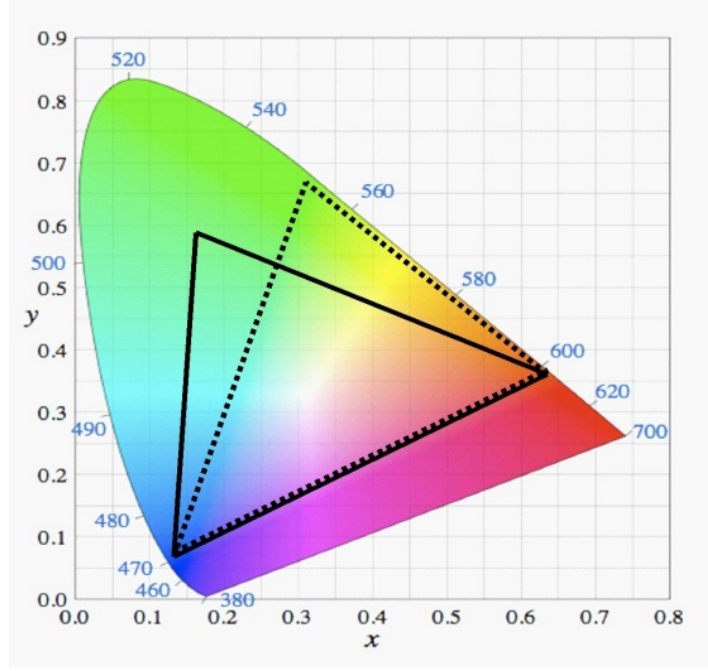


Figure 1.2 Color gamut triangles with a different green primary.

To overcome the limitation of RGB primaries, we propose here a five-primary LCD by including yellow and cyan color filters. Figure 1.3(a) shows the transmission spectra of conventional RGB color filters and Figure 1.3(b) depicts the transmission spectra of our five primaries. The spectrum of yellow CF covers a portion of red and part of green in order to get more saturated yellow than the combination of standard green and red color filters shown in Figure 1.3(a). Similarly, the cyan CF covers a portion of green and blue to get highly saturated cyan color. Meanwhile, we used a more saturated green color filter; its full-width-half-maximum is ~ 75 nm, as compared to ~ 100 nm for a typical green color filter. The narrower bandwidth makes the green color more saturated, but its transmittance is lower. There are two other important guidelines while choosing the primaries: 1) the white point at color temperature of D65, and 2) the proper relative luminance for each primary. According to the MacAdam limits

[1], the color solid describes the colors near monochromatic can only achieve a very low luminance level except yellow. It also states the relative luminance of different color for objects. After having taken the MacAdam limits and practical color filter manufacturing capability into consideration, we optimized the color filter design and chose five-primary CF spectra as depicted in Figure 1.3(b).

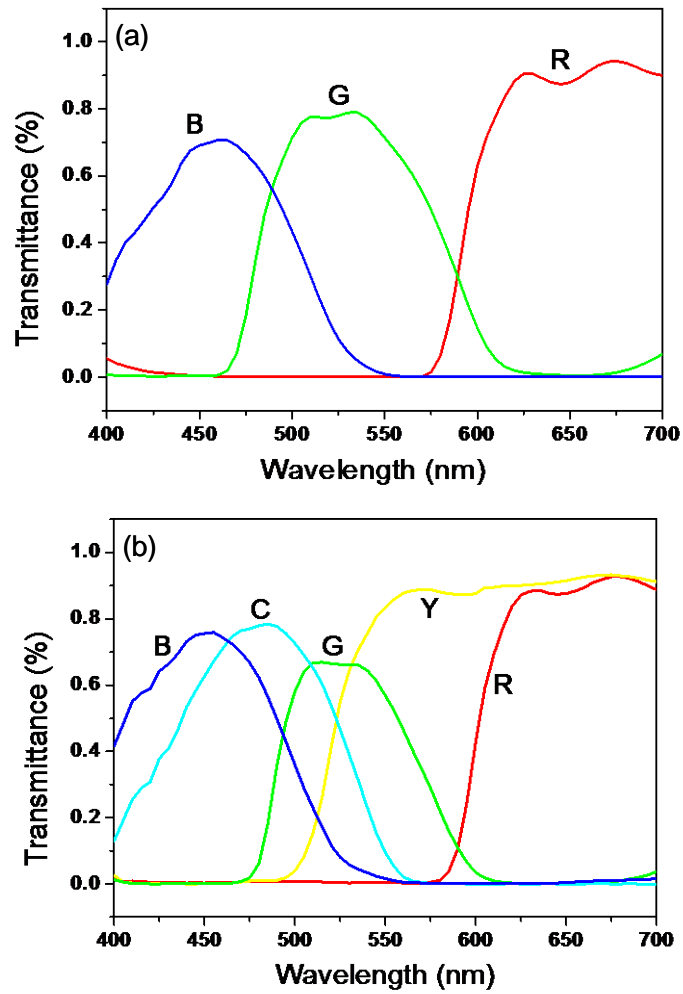


Figure 1.3 Transmission spectra of (a) conventional RGB color filters and (b) five-primary RGBYC color filters we developed.

There are several kinds of color pixel arrangement and size designs [18]. In our simulations and application, we adopted the same sub-pixel size of three-primary for our five-primary approach because it is preferred by LCD manufacturers. We first used conventional CCFL (Figure 1.4) as backlight source and consider the transmission spectra of polarizers and liquid crystal in multi-domain vertical alignment (MVA) mode [19] [20]. Figure 1.5 shows our simulated color gamut for RGB and RGBYC MVA LCD TVs.

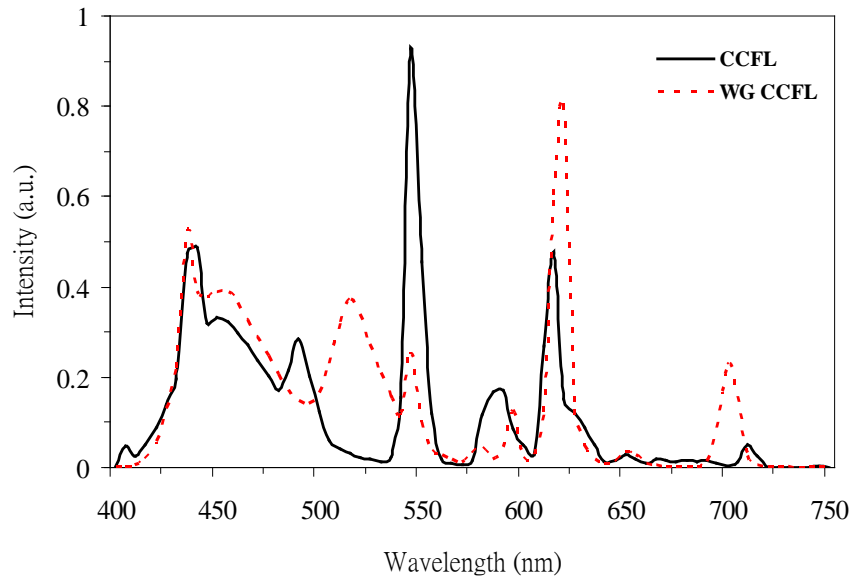


Figure 1.4 Emission spectra of a conventional CCFL and WG CCFL.

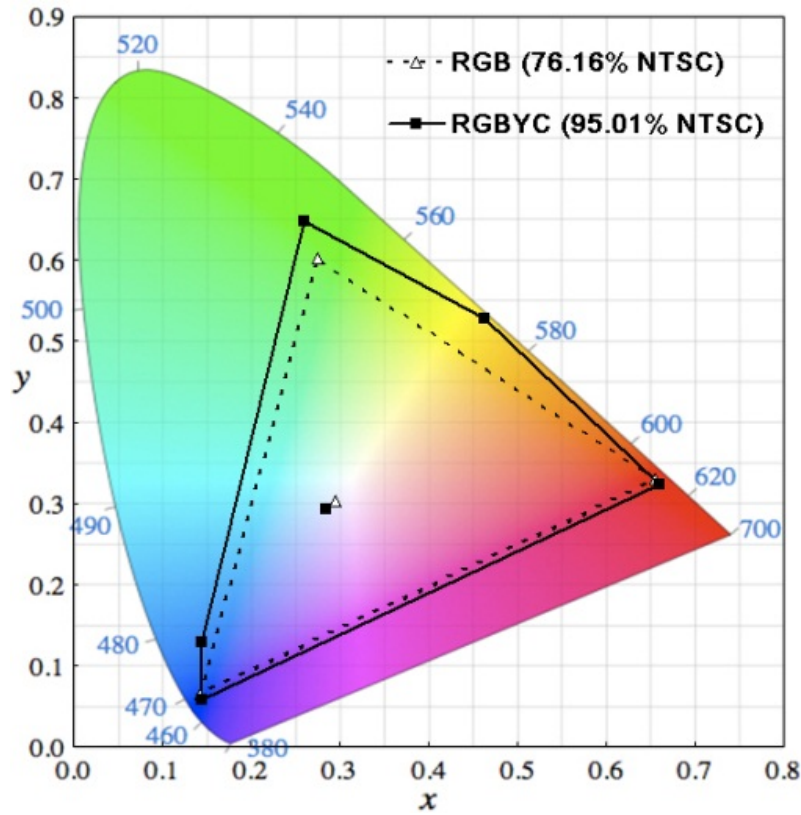


Figure 1.5 Simulated color gamut of RGB (dashed lines) and RGBYC (solid lines) primaries using a MVA LCD.

Table 1.1 Simulated results on the brightness and color coordinates of 3- and 5-primary LCDs.

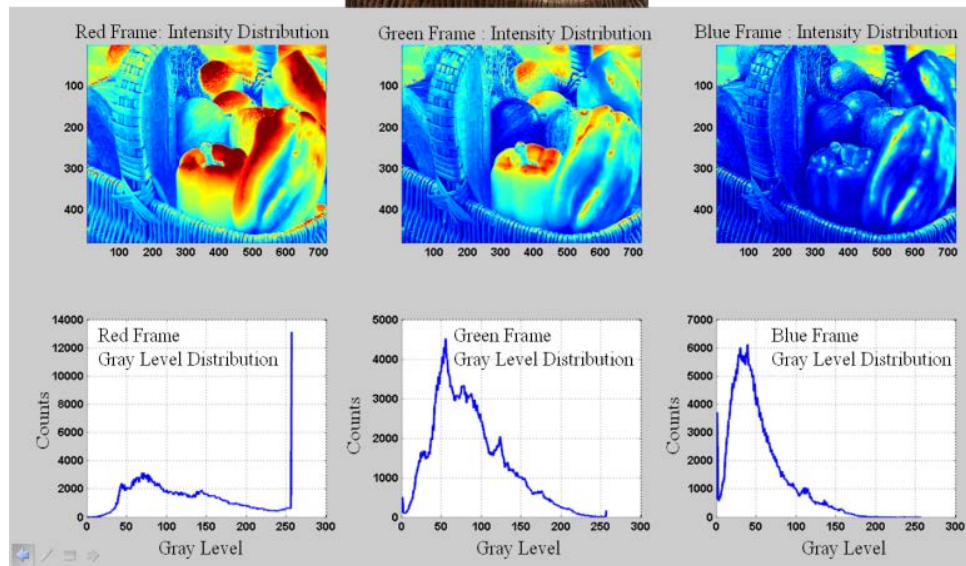
Three primary				Five primary			
Color	Luminance (nit)	Chromaticity		Color	Luminance (nit)	Chromaticity	
		x	y			x	y
W	450.00	0.30	0.30	W	532.27	0.28	0.29
R	102.50	0.66	0.33	R	50.95	0.66	0.32
G	304.91	0.28	0.60	Y	258.01	0.46	0.53
B	42.58	0.14	0.06	G	138.37	0.26	0.65
				C	59.60	0.14	0.13
				B	25.34	0.15	0.06

Table 1.1 lists the simulated color coordinates and luminance for each primary. From Table 1.1, the color gamut of conventional RGB LCDs is ~76% NTSC. With five primaries, the color gamut increases to 96% NTSC with the same CCFL backlight as Figure 1.5 shows. Moreover, the white luminance is increased by 21% for the five-primary LCD. The increase of white luminance is mainly contributed by the additional yellow and cyan colors. Because we employ more saturated CFs and our RGB pixel numbers are just 60% as compared to a conventional RGB display, we would expect a reduction of RGB luminance for the five-primary display. When the five-primary LCD displays a single primary color, say R, G, or B, the luminance would be lower than that of the three-primary one. However, in real situation, an object that reflects single color or narrow spectral bandwidth (i.e., pure color) will have a very low luminosity. It means the images rarely just show RGB primaries at the highest gray level. In fact, in a RGB-primary display the green luminance should be relatively high because of the need to produce bright yellow and standard white after combining with R and B. While in our five-primary LCD, we could afford to have a more saturated green primary to trade for a wider color gamut because we already have yellow primary.

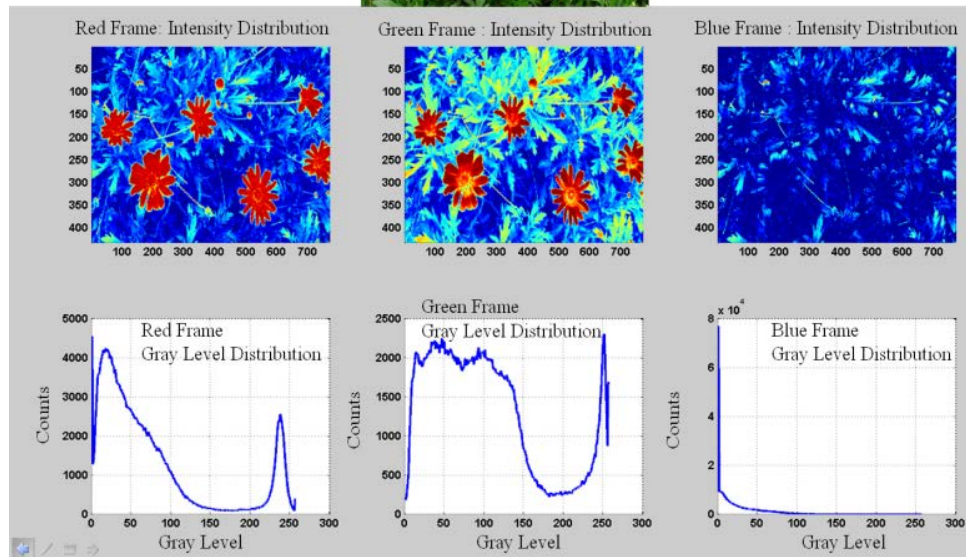
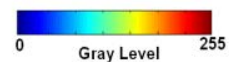
To validate these assumptions, we chose some colorful and representative photos for image analysis. Figure 1.6 shows three photos of the pixel color with respect to gray level distribution. We found in most cases the RGB sub-pixels are usually in the middle range between the maximum (255) and minimum (0) gray levels. The situation of high gray levels usually just happens when displaying yellow objects, e.g., the flowers shown in Figure 1.6(b), or the bright white, e.g., the sky shown in Figure 1.6(c). We realize that all the primaries need to be at the highest gray level while displaying higher luminosity of yellow or white. It means the luminance

for RGB can be lowered if we have other sources to show yellow and white. Our five-primary design overcomes this problem well because it provides a higher yellow and white brightness than the conventional RGB LCDs due to the extra yellow and cyan. Although the luminance of our RGB colors is lower, it is still high enough to show and reproduce most colored images. When displaying the RGB color contents of an image, we can also adjust the gamma curve to get a better contrast ratio and brightness. According to the metamerism theory [1], there are unlimited choices of weighting ratios for five primaries to reproduce a particular mixed color. In the optimization process, we could choose a higher weighting ratio for Y, G, and C to reproduce a particular color since these three colors have a higher brightness. Therefore, after optimization of color conversion and gamut mapping from three-primary color space into five-primary signals, the decreased RGB brightness would not be a big issue in our five-primary LCDs. On the contrary, we find that five-primary LCDs exhibiting a higher brightness than RGB LCDs when displaying full color images.

(a)



(b)



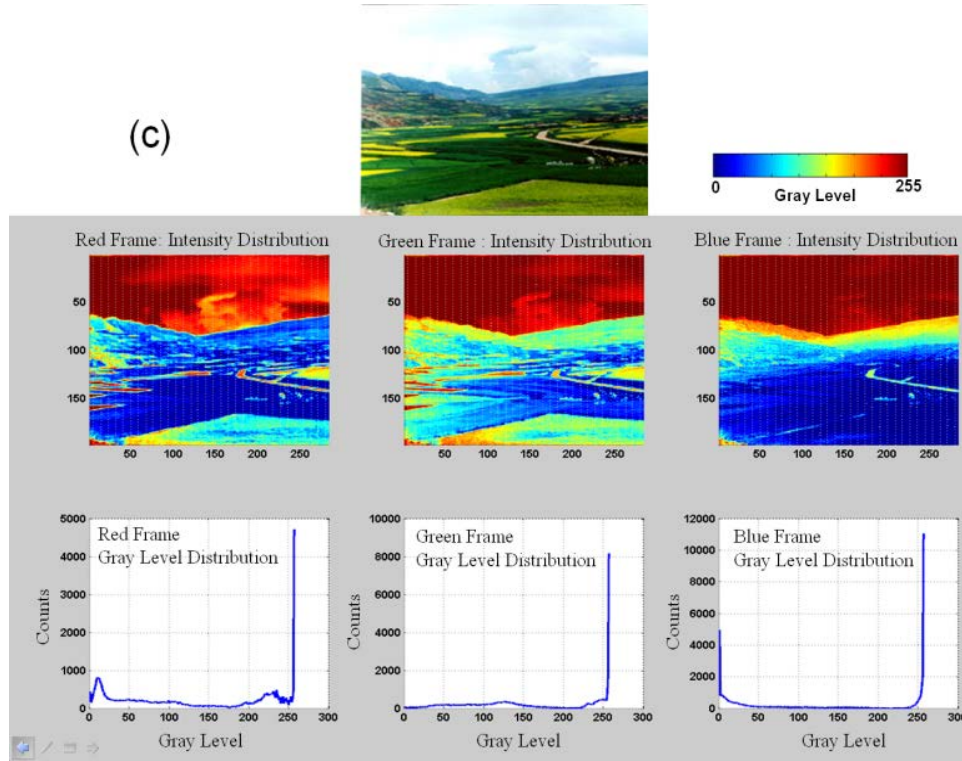


Figure 1.6 Image analysis for gray level distributions. (a) A fruit basket, (b) Lotus in a pond, and (c) a pasture and sky.

1.3 Five-Primary LCDs and Comparison

Because most input image signals are in three-component format, such as RGB and YCbCr [21], a color conversion algorithm is needed in order to convert the three-primary input into five-primary signals. To do so, we applied the same algorithm developed for multi-primary projection TVs to LCD TVs [22].

Figure 1.7 shows some pictures taken from the 32" five-primary LCD TV prototype. The images of the five-primary LCD TV (left) look much more vivid and brighter than the traditional RGB LCD TV (right). The extra yellow and cyan primaries not only widen color gamut but also

provide very good color reproduction.

The measured data are shown in Figure 1.8 and Table 1.2. The color gamut is increased by 26% and the brightness of white point is also increased by 26%. The agreement between simulated and measured color gamut is within 5%. The possible errors might originate from the spectrum deviation in the mass production of color filters and CCFL.



Figure 1.7 Photos from a 32" MVA LCD TV prototype. Left column: five-primary (RGBYC); right column: conventional RGB primaries. Backlight: CCFL in both systems.

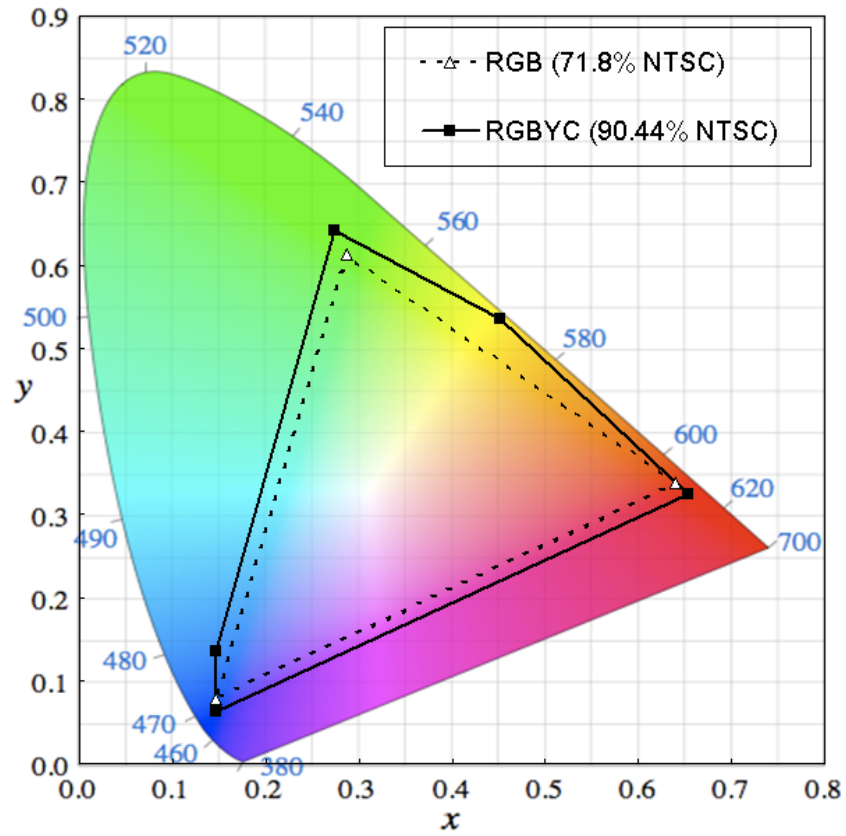


Figure 1.8 Measured data for the RGB and RGBYC MVA LCD TVs.

Table 1.2 Measured data for RGB and RGBYC displays.

Three primary				Five primary			
				Color	Luminance(nit)	Chromaticity	
						x	y
Color	Luminance(nit)	Chromaticity		W	568.50	0.30	0.33
		x	y	R	45.00	0.65	0.32
W	449.60	0.28	0.29	Y	290.60	0.45	0.54
R	93.50	0.64	0.34	G	163.80	0.27	0.64
G	293.20	0.29	0.61	C	50.90	0.15	0.14
B	61.20	0.15	0.08	B	26.50	0.15	0.06

As a promising solution for wide color gamut displays, we also compare the performance of our five-primary display with other competing approaches such as RGB-primary using wide gamut CCFL (WG CCFL) (Figure 1.4) and RGB LEDs. Results are summarized in Table 1.3. In our simulations using WG CCFL and RGB LED backlight in the RGB-primary system, the color gamut achieves ~90.23% and 120%, respectively. However, these three-primary based technologies still cannot reproduce good yellow and cyan colors like our five-primary LCD.

Table 1.3 Performance comparison of wide-gamut CCFL, RGB LEDs and our five-primary LCDs.

	WG CCFL	RGB LEDs	RGBYC Primaries
Gamut Value	○	◎	○
Gamut Shape / Color Reproduction	×	△	◎
Brightness Efficiency	×	×	◎
Cost	○	×	◎
Signal Processing / Color Conversion Algorithm	◎	◎	△

×:Poor; △: Fair; ○: Good; ◎: Excellent

We also simulated our five-primary MVA LCD using WG CCFL backlight; its emission spectrum is shown in Figure 1.4. Here, we assume the conventional CCFL and WG CCFL have the same luminosity. From our simulation results shown in Figure 1.9 and Table 1.4, we find that the color gamut reaches ~114.07% NTSC and, moreover, the brightness of white point increases ~7%. Although the yellow brightness is reduced by ~20%, other four primaries experience brightness increase. The better spectrum match between our five-primary CFs and WG CCFL is responsible for the significant increase in brightness. We believe that this could be the highest NTSC ratio ever achieved with such a high efficiency by using a WG CCFL backlight.

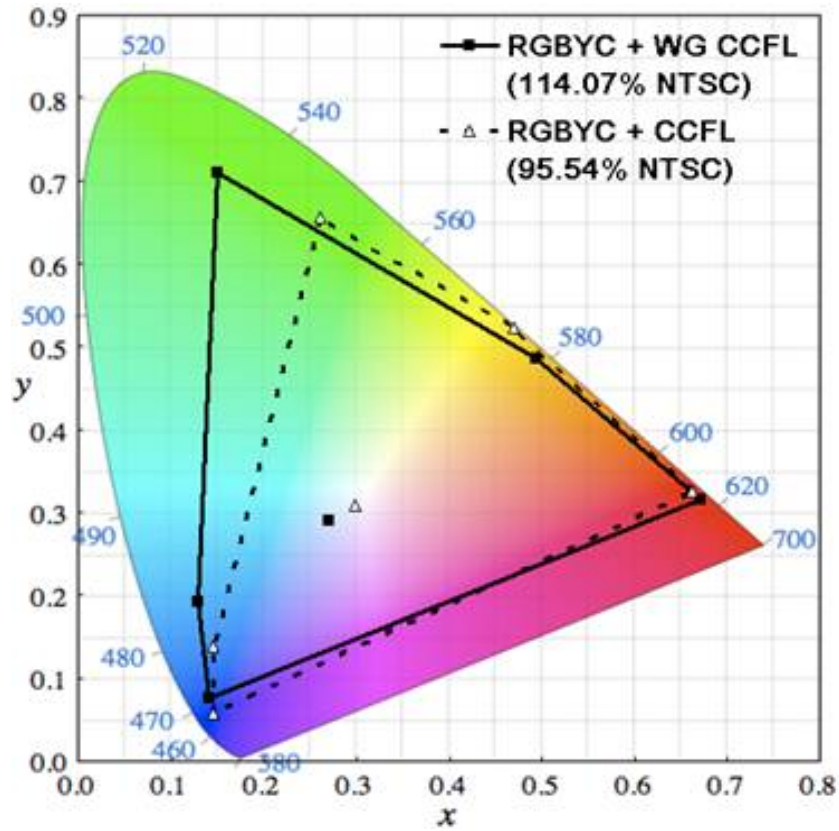


Figure 1.9 Simulated color gamut of RGBYC-primary with conventional CCFL (dashed lines) and RGBYC with WG CCFL (solid lines) in a MVA LCD.

Table 1.4 Simulation results on display brightness and color coordinates of our 5-primary MVA LCD using conventional CCFL and WG CCFL.

	RGBYC + CCFL	RGBYC + WG CCFL			Luminance Gain (Luminance ^b / Luminance ^a)
Color	Luminance ^a (nit)	Luminance ^b (nit)	Chromaticity		
			x	y	
W	532.27	571.27	0.27	0.29	107.33%
R	50.95	70.57	0.67	0.32	138.52%
Y	258.01	206.80	0.49	0.49	80.15%
G	138.37	145.40	0.15	0.71	105.08%
C	59.60	107.98	0.13	0.19	181.18%
B	25.34	38.03	0.14	0.08	150.05%

1.4 Summary

We have successfully developed and demonstrated a five-primary LCD TV prototype. Using the same CCFL backlight and pixel layout and dimension, the color gamut of our five-primary display is more than 90% NTSC without sacrificing brightness. This technology is promising for wide color gamut displays. Moreover, ~26% increase in white luminance give us a flexibility to reduce the light source density and power. Low power consumption is highly desirable from energy saving viewpoint. If a WG CCFL is employed, the color gamut of our five-primary MVA LCD is over 114%.

CHAPTER 2: FIELD SEQUENTIAL COLOR DISPLAY

2.1 Introduction

Low power consumption is a critical requirement for all liquid crystal displays, especially for portable electronic devices and large screen TVs. As Figure 2.1 shows, two most lossy components in a LCD system are polarizer and color filters. The polarizer transmits ~45% of the incident backlight, while each color filter only transmits ~30% of the incoming white light. Therefore, the overall transmittance is usually ~5% in a conventional LCD. To overcome the light loss from polarizer, backlight recycling using a reflective polarizer, such as 3M's Dual Brightness Enhancement Film (DBEF) has been widely implemented [23] [24].

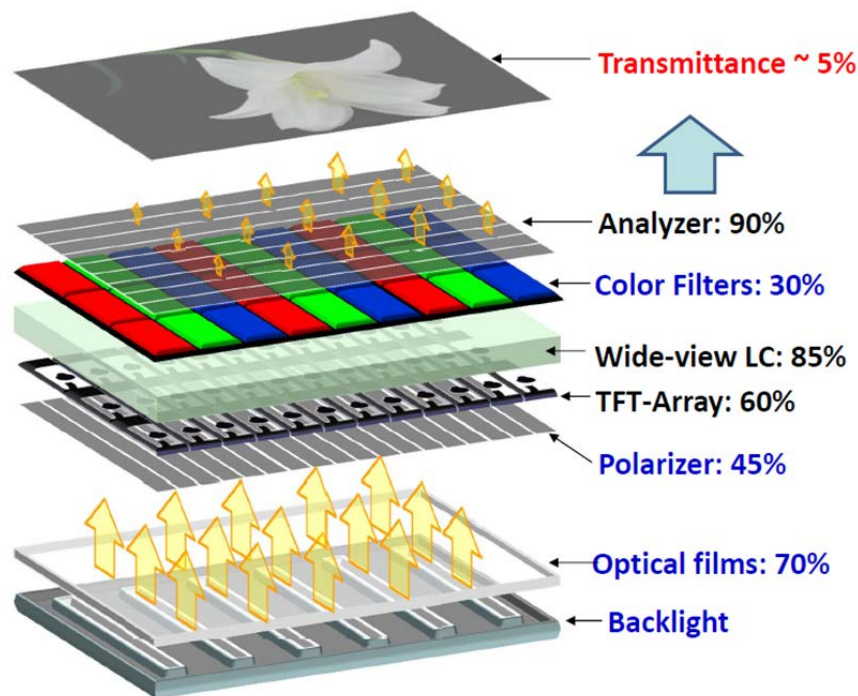


Figure 2.1 Optical transmittance of each component in a LCD.

To avoid the dramatic absorption loss from color filters, field-sequential-color (FSC) using red (R), green (G) and blue (B) LEDs has been proposed [25] [26] [27]. In a FSC LCD, each primary color appears sequentially. If the field's frequency is fast enough, the observer's eyes could integrate the sequential fields and perceive the original colored images as Figure 2.2 shows. By using the RGB LEDs backlight in FSC LCDs, we can remove the color filters in a conventional LCD. Therefore, a FSC LCD offers two important advantages over the color filters-based LCDs: 1) its optical efficiency is improved by $\sim 3X$, and 2) the device resolution density is improved by $3X$.



Figure 2.2 Working principle of the field-sequential-color display.

2.2 Color Breakup

In FSC LCDs, the frame rate would be tripled as compared to the conventional LCDs. Therefore, the response time of the LC materials should be at least $3X$ faster for the FSC LCDs. However, $3X$ faster of the response time is not enough for FSC LCDs in reality. A biggest challenge for FSC LCDs is the need of fast LC response time in order to suppress the color breakup (CBU) [28] [29] [30] [31] [32].

CBU is the most disturbing defect that degrades the image quality in FSC displays. It can

be observed in stationary or moving images. When our eyes trace a moving object, each sequential color (i.e., R, G, and B) image would project on our retina at different positions as Figure 2.3 shows. Therefore, when there is a relative speed between the images and observers' eyes, the observer will see the color splitting patterns or rainbow effect at the boundary between two different colors (Figure 2.4).

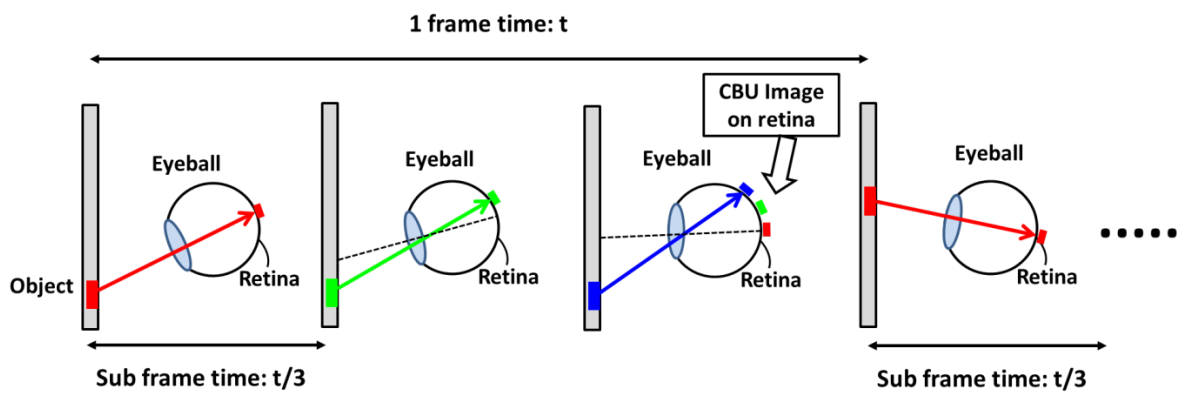


Figure 2.3 The reason of color breakup.



Figure 2.4 Rainbow effect caused by color breakup.

In order to reduce CBU, we can increase the field frequency to 540 Hz or even up to 1000 Hz [33]. This approach has been widely used in FSC projectors. However, for direct-view LCDs, higher field frequency would require new LC materials with very fast response time (i.e., less than 1ms).

Several other methods have also been proposed instead of using new LC materials. Such as inserting another color or black fields [34] [35], motion compensation technique [36], four color fields arrangement [37], and Stencil-FSC method [38]. However, most of these methods still require fast LC response time. Some methods even sacrifice the display brightness and some are restricted by the uncertainty of observers' motion.

In Chapter 1, we already introduce the principles of five-primary color (R, G, B, yellow (Y), and cyan (C)) LCD which has been shown to exhibit a very good color and brightness [17] [18] [39]. Because of the better color reproduction and optical efficiency, we extend the five-primary approach to FSC LCD. We propose a practical way to reduce CBU by using five-primary-color technique for direct-view FSC LCD without enhancing the frame rate. Meanwhile, our design not only widens the color gamut but also increases the white brightness, as compared to the three-primary LCD.

2.3 Multi-Primary FSC LCDs

The two-dimension time and location diagram is usually used to evaluate CBU (Figure 2.5). By integrating images of consecutive frames along the trace of saccadic eye motion, we can evaluate the color and brightness variations of rainbow-like CBU patterns. From the simulated CBU (Figure 2.6), it shows that the three-primary FSC displays with sub-frame frequency of 540

Hz (i.e., frame rate of 180 Hz) have the CBU width of N pixels. N is determined by the relative speed between the images and observers' eyes. Figure 2.6(b) and Figure 2.6(d) show the CBU width for higher and lower frame rates, respectively. We observe that the higher frame rate causes a less noticeable CBU. There is no doubt that increasing the frame rate is an effective way to suppress CBU. However, the requirement for fast LC response time makes this method a challenge.

According to the two-dimension time and location diagram shown in Figure 2.5(b), the CBU width for five-primary is $5/3$ times more than the three-primary under the same frame rate. Therefore, it is naturally expected that five-primary could suffer from larger CBU as compared to three-primary displays. Some psychophysical experiments about the comparison of CBU visibility between three-primary and five-primary displays have been reported [40]. Surprisingly, the results indicate that, most of the time, CBU for five-primary is less visible than three-primary. However, thus far there is no further study and systematic analysis for this result. In our simulations based on five-primary, we develop a method to compress CBU by optimizing the color sequence and weighting ratios.

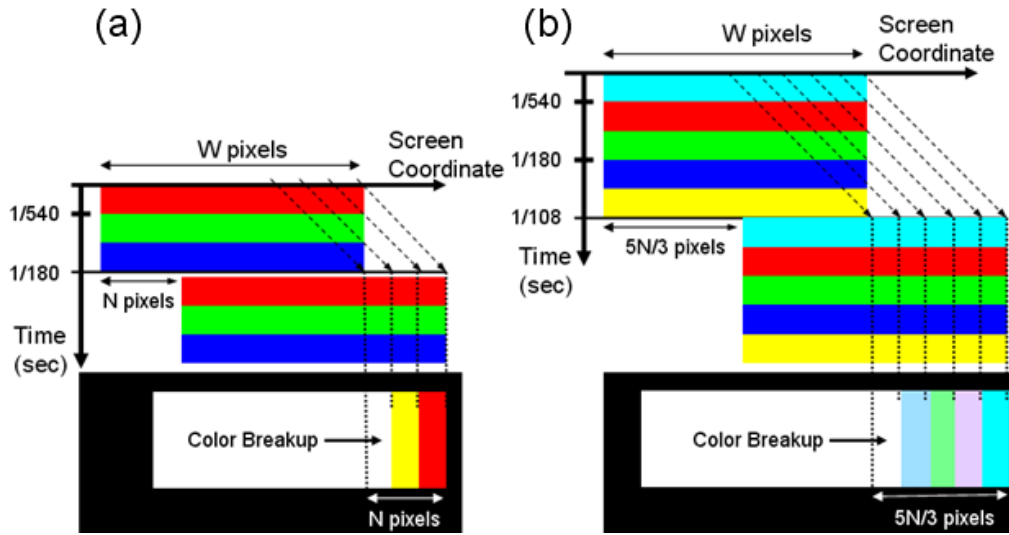


Figure 2.5 Two-dimension time and location diagram. The upper parts of each diagram represent the moving white objects with width of W pixels. The lower parts are simplified CBU patterns without considering the brightness variation. The slant dashed arrows show the eyes tracking along the movement of object.

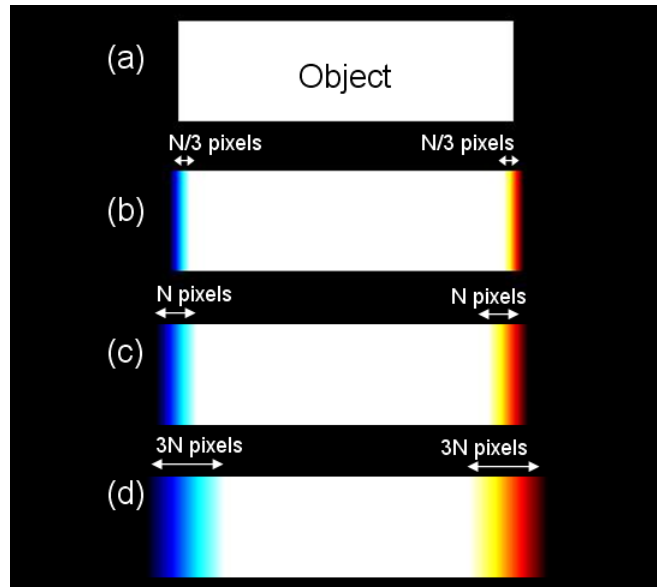
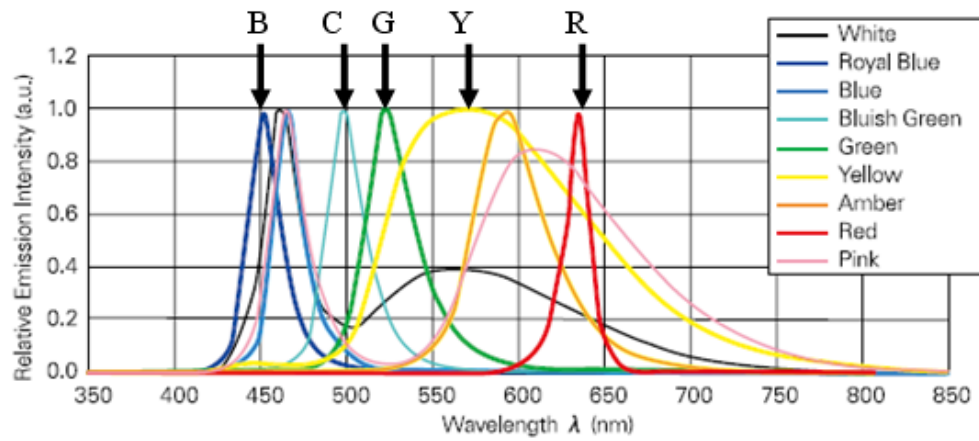


Figure 2.6 Simulated CBU for three-primary display. (a) White object, (b) Frame rate = 540Hz, (c) Frame rate = 180Hz, (d) Frame rate = 60Hz.

When a three-primary LCD displays a specific color, there is a unique color ratio corresponding to this color. However, there are numerous possibilities for five-primary. Here, we adopt the commercialized LEDs from Nichia in our simulations. The spectra and luminance intensity are shown in Figure 2.7. From Table 2.1, we find that there are many choices for the five-primary to reproduce the same white color coordinate of standard illuminant D65 (i.e., $x = 0.3127$, $y = 0.3290$). In order to choose the best solution among these infinite combinations, we take some basic rules and requirements into considerations. First, we abide to the MacAdam limits [1] which set the theoretical maximum relative reflection and brightness between a specific color and white under D65 illumination. From Figure 2.8, this theorem tells us a reasonable relationship of brightness between each primary should be $Y > G$, $G > R$, $G > B$, $G > C$, and $C > B$. Second, we consider the capability of LED brightness of different colors. In the real design of LED backlight, we tend to use the same numbers of LEDs for each primary. We also prefer each LED to work at its maximum luminance, so that we can minimize the number of LEDs. For example, if we choose a ratio of R:G:B to be 10:37:5, it is an acceptable ratio based on the brightness ratio of 10:37.7:9.3 shown in Figure 2.7. However, the ratio of 10:37:12 would not be a good choice because we need more blue LEDs to fulfill the design. Third, we would like to optimize the brightness. Table 2.1 also shows that different ratio would lead to a different brightness and we prefer the ratios with higher brightness. After considering the abovementioned three criteria, we obtain a set of ratios for R:G:B:Y:C to be 12.36:18.90:4.04:48.33:16.37.



	Red	Green	Blue	Yellow	Cyan
Luminance Intensity (mcd)	10k	37.7k	9.3k	6.15k	6.4k

Figure 2.7 LED spectra and luminance intensities. (Ref. Nichia Co.)

Table 2.1 Color ratios for standard illuminant D65

Three-primaryDisplay			
R (%)	G (%)	B (%)	W (%)
26.80	67.68	5.52	100.00

Five-primaryDisplay					
R (%)	G (%)	B (%)	Y (%)	C (%)	Brightness (a.u.)
1.11	8.38	4.96	78.03	7.52	128.16
10.96	22.10	4.58	51.45	10.91	194.36
15.46	37.40	4.99	36.28	5.88	275.61
13.32	22.78	4.17	44.66	15.07	223.89
13.33	20.90	4.08	45.80	15.89	218.35
12.14	20.53	4.29	48.73	14.31	205.20
12.36	18.90	4.04	48.33	16.37	206.91
⋮	⋮	⋮	⋮	⋮	⋮

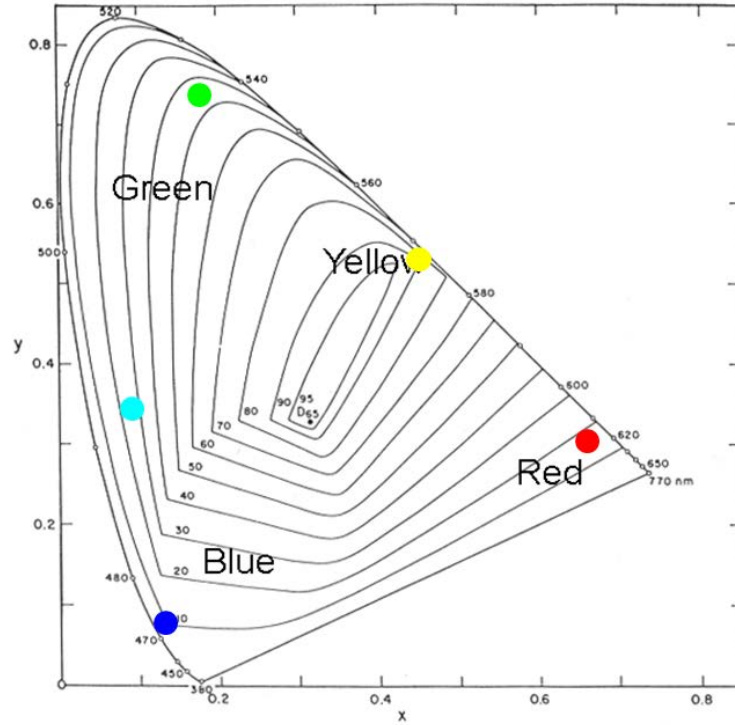


Figure 2.8 MacAdam Limit boundaries for the CIE 1931 color space chromaticity diagram.

Based on the preliminary color ratios, we simulate the CBU with different color order as Figure 2.9 shows. The left side shows the color order and the right side is the corresponding CBU patterns. In comparison to the CBU of three-primary in Figure 2.9(a), the five-primary has a broader CBU as we expected from time and location diagram (Figure 2.5(b)). However, we can find some better color orders that cause a weaker perceived CBU. For example, Figure 2.9(e) and Figure 2.9(f) exhibit a smaller CBU than those from Figure 2.9(b) to Figure 2.9(d). It is because the high brightness colors, such as yellow and cyan which are in the middle order, tend to merge with the white color of the object. Similarly, the lower brightness colors of red and blue tend to merge with the black background. Due to the lower color contrast and luminance contrast, we perceive that the CBU is compressed.

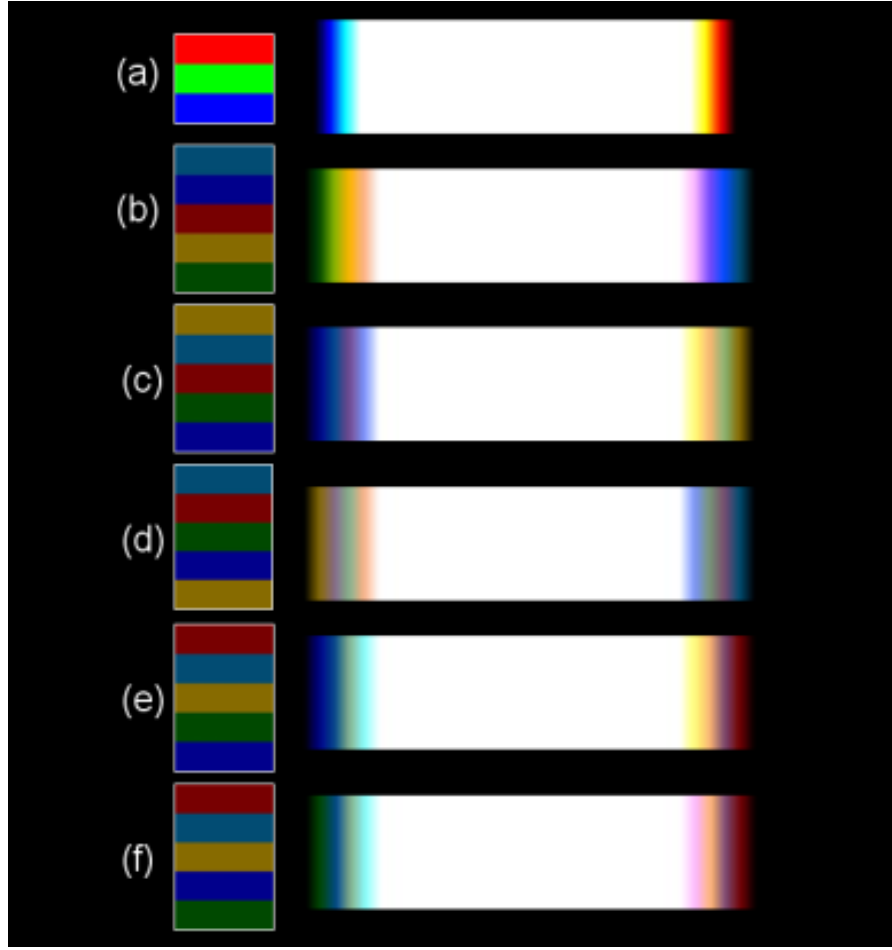


Figure 2.9 Simulated CBU with different color appearing sequence.

Although we can continue to optimize the color sequence of RCYGB or RCYBG, we still observe the CBU in five-primary FSC display. To further reduce CBU, we propose to boost the ratio of yellow and cyan brightness; meanwhile, to reduce the red, green, and blue ratios. From Figure 2.10(b) to Figure 2.10(e), the CBU is gradually suppressed when the ratio of red, blue, and green is decreased. The CBU reduction is more pronounced if we could get rid of green completely while reproducing white color. Because of the weaker red and blue colors, these colors are almost merged to the black background. Our eyes also tend to trace the brighter color

fields, such as yellow and cyan, thus, we feel these two colors are merged to the white object. Here, we rearrange the sequence of green to be the last in order to get the least CBU (Figure 2.10(e)). In comparison to the CBU of three-primary (Figure 2.10(a)), we effectively compress the CBU by adjusting the color order and weighting ratios.

When we want to realize the lower brightness ratio of R, B, or G, we use the liquid crystal cell to modulate the brightness instead of dimming or turning off the backlight. Therefore, the backlight emits each primary sequentially as the normal FSC backlight. There will be no need to change the electronic control of our five-primary backlight system.

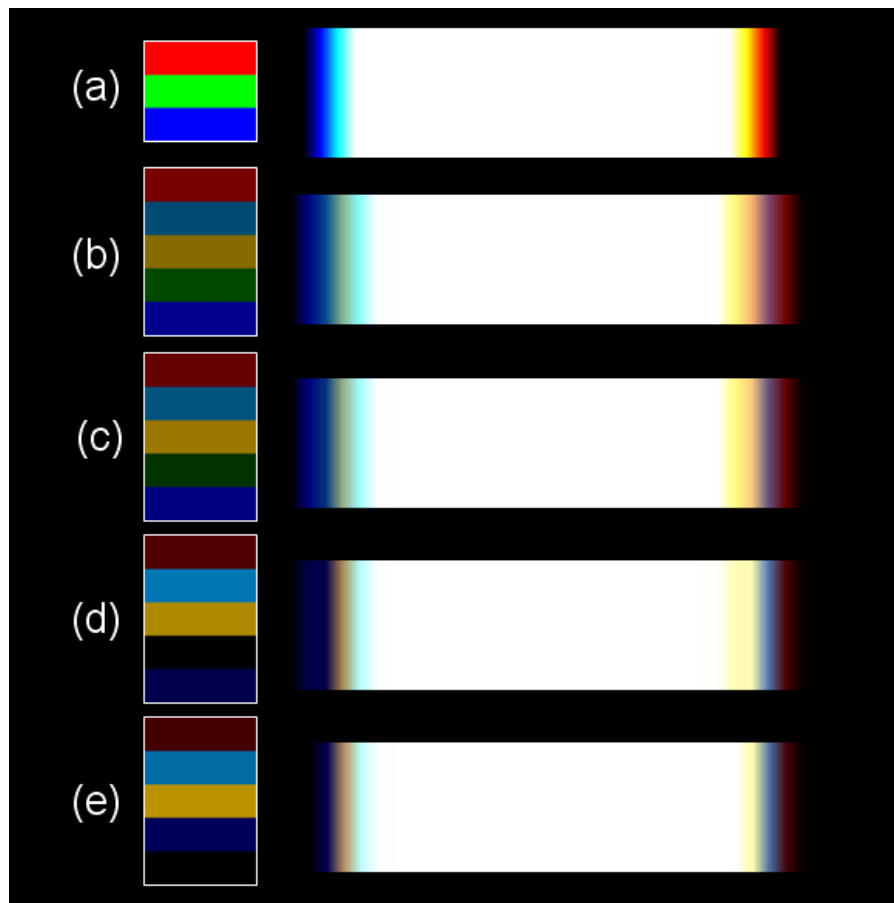


Figure 2.10 Simulated CBU with different color weighting ratios.

Table 2.2 shows some choices of color ratios leading to a fairly small CBU for five-primary in representing white color. We would choose the most appropriate ratio after considering the least color shift (Δuv) at different viewing angle [10] [17], highest brightness, and least CBU. Usually, the solution for the least color shift might not be the same as that for the highest brightness or least CBU, and we need to compromise between these factors. If the CBU is acceptable, we could choose the ratio with the highest brightness. When showing the lower gray level of white (i.e. lower brightness), we could choose the ratio with the least color shift but not necessarily with the highest brightness.

Table 2.2 Color ratios and color shift in IPS mode LCDs

R (%)	G (%)	B (%)	Y (%)	C (%)	Brightness (a.u.)	Δuv
0.93	0.00	13.39	43.84	41.84	467.62	0.0361
0.92	0.00	13.22	43.29	42.57	473.55	0.0358
0.91	0.00	13.29	42.64	43.16	480.78	0.0357
0.75	0.00	13.25	44.13	41.86	464.52	0.0360
0.75	0.00	13.45	44.03	41.77	465.56	0.0361
0.74	0.00	13.31	43.59	42.36	470.30	0.0359
2.31	0.00	13.11	40.67	43.91	485.82	0.0358
1.77	0.00	13.24	41.63	43.35	492.14	0.0359
1.75	0.00	13.09	41.14	44.02	484.61	0.0356

Figure 2.11 shows the simulated CBU for yellow and cyan objects. It is easy to realize that a five-primary LCD has no CBU when displaying these two color tones. Unlike a three-primary LCD which generates yellow by mixing red and green, or cyan by mixing green and blue, the five-primary LCD can just use yellow or cyan LEDs to display these two colors. Ideally, there would be no CBU.

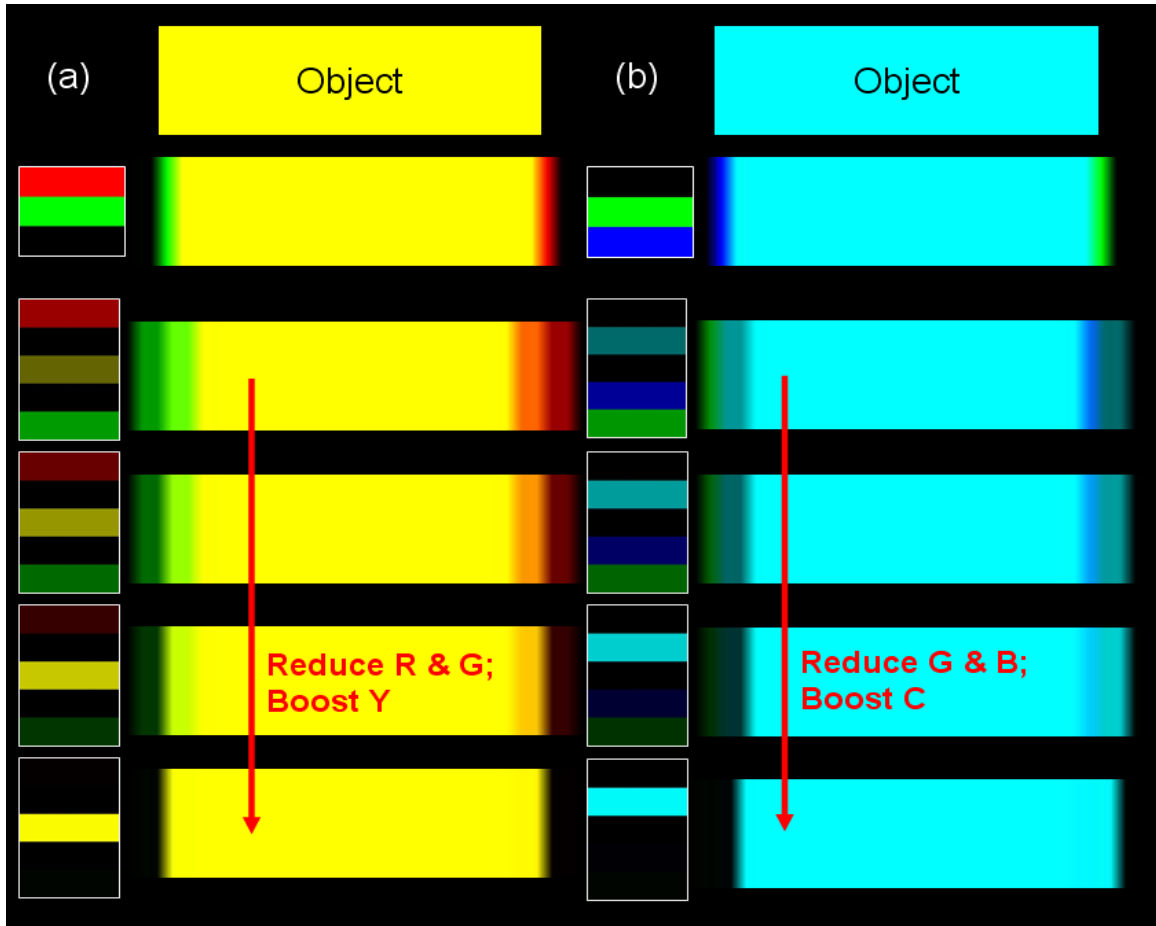


Figure 2.11 Simulated CBU of yellow and cyan objects.

Figure 2.12 shows another two arbitrary colors represented by three-primary and five-primary LCDs. Based on the similar method of showing white color object, we boost the ratio of yellow and cyan to get compressed CBU in five-primary. Under proper color sequence and weighting ratios, the CBU of a five-primary display is not always larger than that of three-primary. On the contrary, after optimization the five-primary LCD could exhibit a smaller CBU than the conventional three-primary.

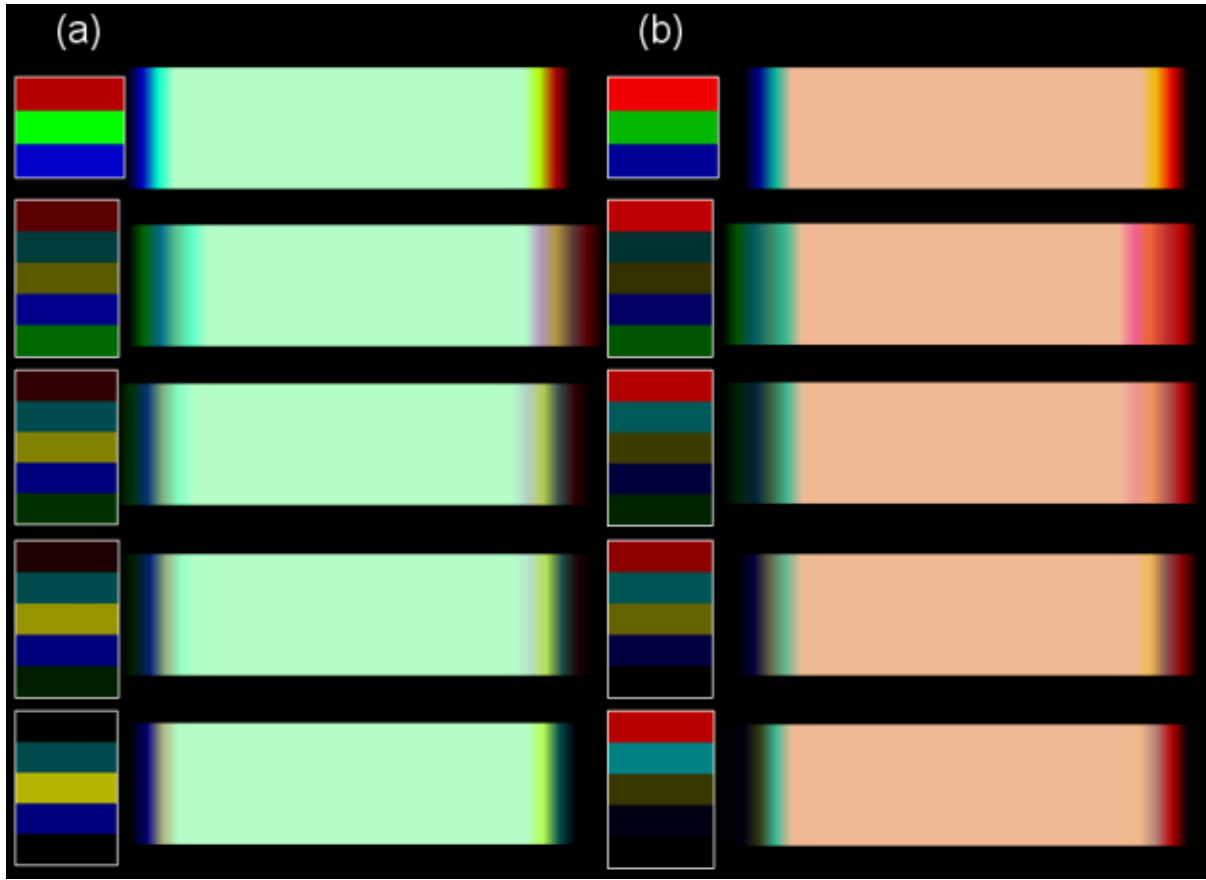


Figure 2.12 Simulated CBU of two arbitrary colors. The bottom figures show compressed CBU after adjusting the color weighting ratios.

Figure 2.13 shows the color coordinates of LEDs and color gamut of our five-primary display. Because of the additional yellow and cyan sources, the color gamut could achieve ~140% NTSC and it provides a very good color reproduction.

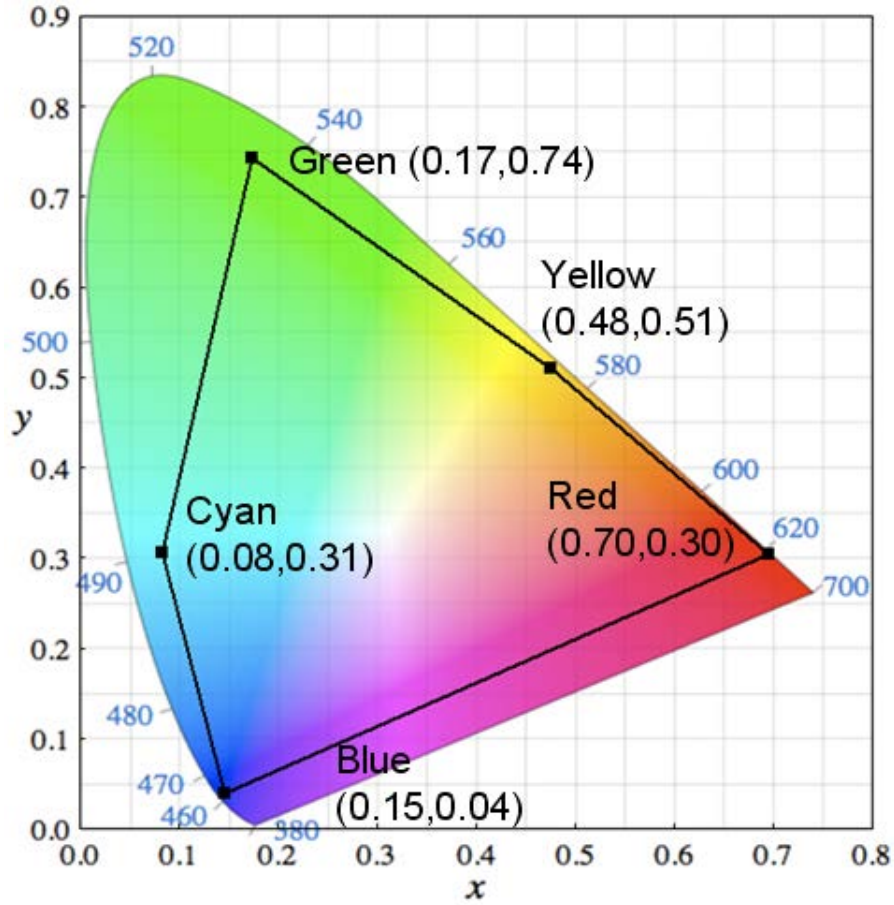


Figure 2.13 Color coordinates and gamut for five-primary LCDs.

We also compare the brightness and numbers of LEDs required between three-primary and five-primary FSC LCDs. In Table 2.3, the luminance intensity means the capability or maximum brightness of a single LED. To satisfy the color ratio we want, we estimate the LED number for each color. Brightness in Table 2.3 means the actual brightness of each color when showing the white color. We notice that not all the LEDs emit light at its maximum luminance. When showing the white color (CIE illuminant D65), the three-primary LCDs have the total brightness of 37.31 (a.u.) during each frame time (i.e., 3/540 Hz). For the five-primary LCDs, the

total brightness would be 70.23 (a.u.). However, under the same sub-frame rate (i.e. 540 Hz) as three-primary, the five-primary LCDs take more time (i.e. 5/540 Hz) to complete each frame. Therefore, the brightness that we perceive in five-primary FSC LCDs should be multiplied by a factor of 3/5. After considering the field sequential factor for five-primary, we find the brightness of 42.14 (a.u.) in reality. Therefore, the brightness for five-primary is 13% higher than three-primary FSC LCDs.

Table 2.3 The required LED numbers for showing white color (CIE illuminant D65).

Three-primary LCD			
	R	G	B
Ratio (%)	26.80	67.68	5.52
Luminance Intensity (mcd)	10k	37.7k	9.3k
LED Number	1	1	1
Brightness (a.u.)	10	25.25	2.06
Total Brightness: 37.31			

Five-primary LCD					
	R	G	B	Y	C
Ratio (%)	1.77	0.00	13.24	41.63	43.35
Luminance Intensity (mcd)	10k	37.7k	9.3k	6.15k	6.4k
LED Number	1	1	1	5	5
Brightness (a.u.)	1.24	0.00	9.30	29.24	30.45
Total Brightness : 70.23					

2.4 Discussion and Conclusion

From our simulations, we can suppress CBU effectively by choosing proper color order and ratios in the five-primary LCDs. However, a major challenge in our design is the relative low brightness of yellow and cyan LEDs (as of today). From Table 2.3, we realize that the LED numbers we need for yellow and cyan are much more than other primaries. Actually, many LED manufacturers already delve into developing high power yellow and cyan LEDs, and they have obtained promising results and progress recently. We believe this issue could be resolved in the near future.

Another difficulty we encounter is how to present our simulated CBU correctly in the three-primary displays. In the three-primary displays, we combine red and green to generate yellow, or green and blue to generate cyan. However, in the five-primary display, there are particular yellow and cyan sources that are more saturated and brighter. Therefore, it is impossible to display the same yellow and cyan colors in three-primary display as shown in five-primary displays. In addition, as restricted by the limited brightness of green we cannot generate and display very bright yellow and cyan when showing the simulated patterns of CBU in a three-primary display. The intrinsic difference between three-primary and five-primary displays becomes a problem during our optimization process. It causes an uncertain issue when we compromise between the CBU, color shift, and brightness to get the best ratio of each primary. This problem can be easily resolved once we use the five-primary display in the simulations and psychophysical experiments.

We have developed a method to reduce CBU in five-primary FSC displays. With the same sub-frame rate as three-primary, we effectively compress the CBU by adjusting the color

order and ratios. In our simulations, the color gamut is 140% NTSC which provides a very good color reproduction. The brightness is also increased by 13% in comparison to three-primary displays. We believe that once the CBU is reduced to an acceptable level, FSC LCD would become a strong contender for next-generation display technology.

CHAPTER 3: BLUE PHASE LIQUID CRYSTAL DISPLAYS

3.1 Blue Phase Liquid Crystal

3.1.1 Introduction

In Chapters 1 and 2, we propose a five-primary method to reduce the CBU in FSC LCDs. In order to completely eliminate CBU, increasing the frame rate of the sequential color images is still a viable approach. In addition, the higher frame rate helps to reduce motion blur and improve image quality. The higher frame rate (e.g., >480 Hz) would need very fast response time of liquid crystal (e.g., <1 ms). Presently, the gray-to-gray response time of a nematic liquid crystal is about 5 ms which is still inadequate for FSC LCDs.

Recently, optically-isotropic liquid crystals, including polymer-stabilized blue phase (PSBP) and polymer-stabilized isotropic phase (PSIP) liquid crystals draw lots of attentions because of their submillisecond response time [41] [42] [43]. Blue-phase liquid crystals (BPLCs) are often observed in a very narrow temperature range (0.5-2K) between chiral nematic and isotropic phases. In Meiboom's model, BPLCs are comprised of double-twist cylinders arranged in a cubic lattice, where the coexistence of such cylinders and disclination lines stabilizes three-dimensional periodic structures as shown in Figure 3.1.

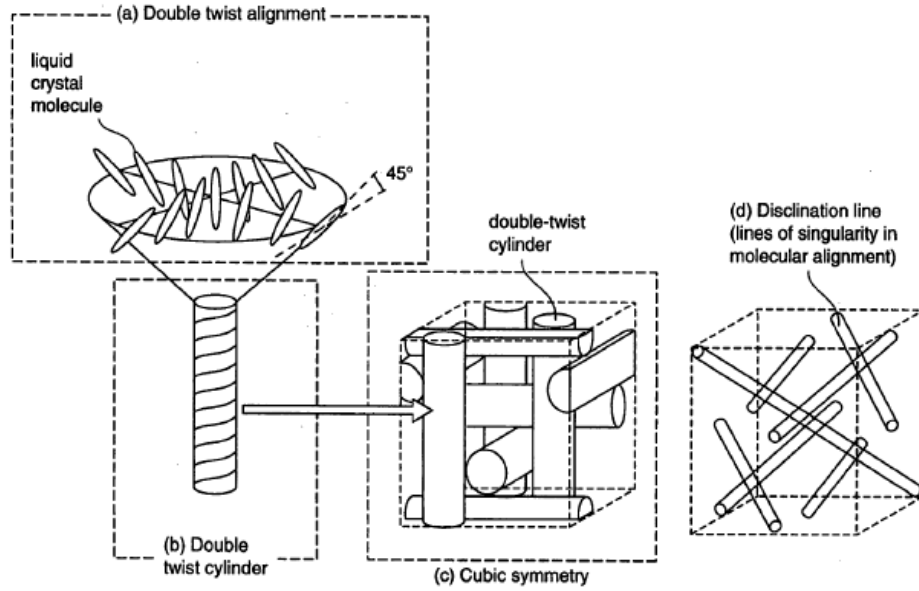


Figure 3.1 Double-twist alignment of LC molecules and cubic structure of BPLCs.

The temperature range of BPLCs can be expanded significantly by polymerizing a mixture of monomers that are localized at the disclination cores [41]. A polymer-stabilized BPLC with a temperature range wider than 60K including room temperature (260-326K) has been demonstrated. The wide temperature enables display applications.

The symmetric cubic structures in a PS-BPLC appear optically isotropic at zero electric field, but become anisotropic when a strong field is applied to induce birefringence. The microscopic structure of such induced birefringence is still not yet completely understood, but macroscopically it can be treated as Kerr effect in isotropic materials caused by the electric field-induced reorientation of polar molecules. The induced birefringence can be described by Kerr effect equation as:

$$\Delta n_{ind} = \lambda K E^2, \quad (1.1)$$

where λ is the wavelength of incident light, K is Kerr constant which depends on the wavelength, temperature and driving frequency [43, 44], and E is the applied electric fields. Kerr effect shows a fast response time (<1 ms) due to the short coherent length of BPLCs.

For display applications, several advantages make BPLCs quite attractive: 1) no need for alignment layer, 2) initially isotropic dark state, and 3) gray-to-gray response time in submillisecond range so that it has potential to be used for color sequential displays, 3D displays, or photonic devices.

3.1.2 Planar In-Plane-Switching BPLCD

For display applications, the BPLCs are usually driven by planar in-plane switching (IPS) electrodes, where the electric fields are substantially in lateral direction [30] [31]. Figure 3.2 shows a traditional planar IPS-based BPLCD. The substantial lateral electric fields would induce birefringence along the direction of electric fields, provided that the employed LC has a positive dielectric anisotropy. The BPLCs could be optically modeled as an isotropic sphere with $E=0$. Under crossed polarizers, the display shows a good dark state. As E increases, the induced Δn changes the sphere into an ellipsoid like a uniaxial medium where the optic axis is along the electric field vector. Therefore, the polarized incident light would experience a double refraction and accumulate certain phase retardation. As a result, the light would transmit through the crossed linear polarizers. The transmittance depends on the applied voltage.

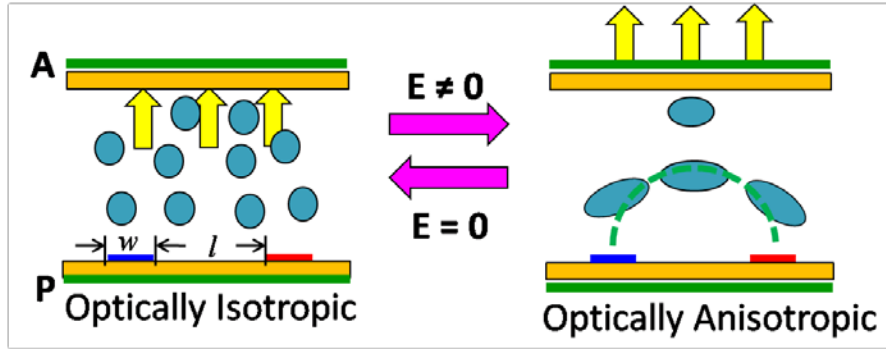


Figure 3.2 Operation principle of a planar IPS BPLCD between crossed polarizers: (a) $E=0$, and (b) $E>0$.

Planar IPS is a popular and mature technology which is widely used in nematic LCDs, such as iPhones and iPads. In an planar IPS BPLC cell, the electric fields have limited penetration depth into the BPLC layer so that the induced birefringence only happens in less than $\sim 3 \mu\text{m}$ thickness [45]. The cell gap does not affect the optical property when it is larger than $3 \mu\text{m}$. Therefore, the electro-optic properties of a planar IPS BPLCD are insensitive to the cell gap.

The operating voltage is a critical issue for planar IPS BPLCDs. A BPLC material with a large Kerr constant ($K \sim 10 \text{ nm/V}^2$) has been recently developed to reduce the driving voltage from over $100 \text{ V}_{\text{rms}}$ to $\sim 50 \text{ V}_{\text{rms}}$. We can also optimize the electrode width and electrode gap to reduce the operation voltage. From the simulated results, smaller electrode width and gap help to reduce driving voltage with tradeoff in transmittance. However, these voltages are still far beyond the acceptable range of mainstream amorphous-silicon thin film transistors (TFTs), and higher driving voltage also dramatically increases power consumption. Another problem of planar IPS structure is that the electric field direction and intensity profile are not uniform. Therefore, some dead zones exist with very weak or vertical electric fields above the electrodes.

These dead zones do not contribute to light transmittance, resulting in a reduced optical efficiency (<70%). Moreover, in a planar IPS mode the nonuniform electric fields are particularly strong near electrode edges which could cause lattice deformation, known as electrostriction effect, leading to hysteresis [46] [47].

Therefore, besides developing new BPLC materials with a large Kerr constant, designing new electrodes and driving mechanism play equally important roles for achieving low operation voltage, high transmittance, and hysteresis-free blue-phase LCDs.

3.2 Reducing Voltage for Blue Phase Liquid Crystal Display

Planar IPS mode exhibits shortcomings in high operation voltage and relatively large hysteresis. To reduce voltage and hysteresis, some modified IPS structures have been proposed.

In order to overcome small penetration depth of the electric fields for IPS structure, a partitioned wall-shaped electrode configuration has been proposed [48]. The parallel wall-shaped electrodes contact top and bottom glass substrate and also work as spacers. In comparison to planar IPS, this structure can generate horizontal electric fields between electrodes and induce uniform birefringence throughout the entire cell gap. From simulation results, the operating voltage is reduced by $\sim 1.5X$ as compared to the planar IPS. However, this structure is difficult to fabricate and has very small aperture ratio which causes low transmittance. In addition, the wall-shaped electrodes would block the oblique backlight and sacrifice the brightness at large viewing angle.

For the traditional planar IPS structure, the horizontal electric field can be enhanced by reducing the electrode gap. However, the smaller electrode gap causes shallower penetration

depth which leads to a reduced optical efficiency. A protrusion electrode structure has been proposed for increasing the penetration depth of electric fields [45]. From the simulation results with 2 μm bottom electrode width, 1 μm top electrode width, 2 μm electrode height, and 3 μm electrode gap, the peak transmittance is $\sim 71\%$ (normalized to the transmittance of two parallel polarizers) at 13 V_{rms} . However, the manufacturing of such small protruded IPS electrodes is still a big challenge in industry. Samsung Electronics demonstrated a 15" BPLCD prototype in 2011 by using the protrusion structure of 4- μm electrode width, 4- μm electrode gap, and 2- μm electrode height. From the measured results, the peak operation voltage is reduced from $\sim 60 V_{\text{rms}}$ to $\sim 38 V_{\text{rms}}$. Semiconductor Energy Lab (SEL) also demonstrated a 6" protruded IPS BPLCD in 2012 with operating voltage $\sim 27 V_{\text{rms}}$. These results clearly show the improvement on operating voltage by using protrusion electrodes for blue-phase LCDs. Although SEL shows the lowest driving voltage reported so far, it is still too high for LCD applications. In addition, Samsung Electronics indicates that residual birefringence, hysteresis, and voltage holding ratio are still unsolved even with protruded electrodes.

The planar IPS electrode with an etched substrate [49] which generates double-penetrating fringe fields was also proposed. Because BPLCs fill the etched region, it helps to contribute the phase retardation and reduce the driving voltage. With 1–2 μm etching depth, the operating voltage is reduced by 30% as compared to the planar IPS. Further improvement by deeper etching is limited because the lateral electric fields only penetrate $\sim 3 \mu\text{m}$. This etched IPS BPLCD also exhibits a wider viewing angle because of the created multi-domain structures in the etched areas. However, this method complicates the manufacturing process and the driving voltage is still too high.

A corrugated electrode for BPLCD was proposed to reduce operating voltage and enhance the transmittance [50]. The periodic corrugated electrodes on the top and bottom substrates can generate a strong horizontal component of electric field to induce a large birefringence of BPLCs. Moreover, this field is uniformly distributed across the entire pixel area and penetrates deeply into the BPLC medium. The accumulated phase retardation along the beam path is large, resulting in high transmittance and low voltage. From simulations, the driving voltage can be reduced from ~ 50 V_{rms} for planar IPS to ~ 9.9 V_{rms} for corrugated structure. The transmittance is also improved ($\sim 85.6\%$) as compared to planar IPS ($\sim 65\%$) because of the uniform electric fields across the pixels and smaller dead zones. This result shows a possibility for TFT addressing and BPLCD applications. Unfortunately, the manufacturing process of the TFT on the corrugated structure is still an issue so far.

In addition to lateral electric fields discussed above, another possibility to drive BPLC devices is to use longitudinal field, which is proposed independently by us [51] and by Kim et al [52]. In Ref. [52], the normal incident backlight is split into two oblique angles by a bottom prism sheet. A top prism sheet is used to orient the oblique light back to the normal direction. The oblique light inside the BPLC can accumulate the necessary phase retardation for achieving continuous grayscales under applied vertical field. Because there is no patterned electrode inside the cell, the cell structure is much simpler than the protruded IPS. However, there are several intrinsic problems of this design. First, the split backlight by the bottom prism sheet would cause double images which in turn degrade the resolution and image quality. Second, the top and bottom prism sheets sandwiched between a polarizer and an analyzer would depolarize the incident backlight and decrease the contrast ratio dramatically. Furthermore, the driving voltage

is still too high for TFT addressing and the optical efficiency in this design is also questionable.

3.3 Vertical Field Switching BPLCD

Although abovementioned methods have been proposed to overcome the high voltage problem of BPLCDs, results are still unsatisfactory. Most of the proposed methods do increase the complexity of manufacturing process. Hysteresis is another important issue. Some of the designs are helpful for reducing hysteresis, but none is actually free from hysteresis. Here, we propose vertical field switching (VFS) for a BPLCD with obliquely incident light to achieve low voltage, high transmittance, and hysteresis-free operation [51] [53].

3.3.1 Device Structure

Figure 3.3 depicts our proposed VFS BPLC device structure. The electric field inside the cell is in the longitudinal direction, and only the incident light at an oblique angle ($0 < \theta < 90^\circ$) can experience the phase retardation effect. For a given BPLC layer thickness, a larger incident angle results in a larger phase retardation, which is helpful for lowering the operation voltage. Hence, we couple the backlight to a large output angle (e.g., $\theta \sim 70^\circ$) and keep it reasonably well collimated. The reason of a well-collimated light is to achieve better viewing symmetry. If the incident light is divergent, the portion with a smaller angle would accumulate less phase retardation and has lower gray levels, while the larger angle part would accumulate more phase retardation and result in higher gray levels. In this case, the divergent backlight would cause asymmetric brightness distribution when viewed from right side or left side of the panel after the light exits to the viewer's side. As a result, it will be difficult to obtain uniform brightness. The

well-collimated backlight is already adopted in some high brightness LCDs and 3D displays [54] [55].

In our design, the polarizer and analyzer are set at 45° and -45° azimuthal angles. The prism films (i.e., coupling films and turning film) are set at 90° as Figure 3.3 shows. We used the ray tracing software (i.e. LightTools) to simulate this structure. Referring to the commercialized prism film (e.g., 3M's brightness enhancement film), the refractive index of our prism films is ~ 1.59 and the thickness is $\sim 150\ \mu\text{m}$. The backlight has a reasonable Gaussian distribution (FWHM $\sim 30^\circ$) and the maximum intensity is at 70° .

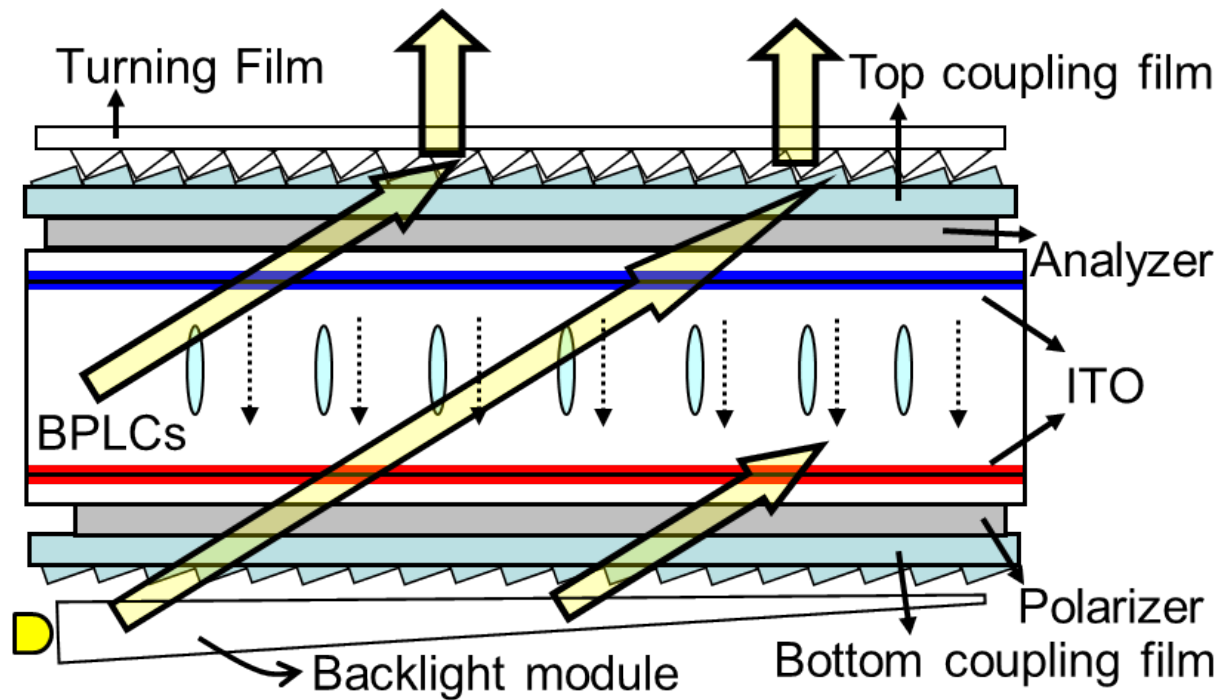


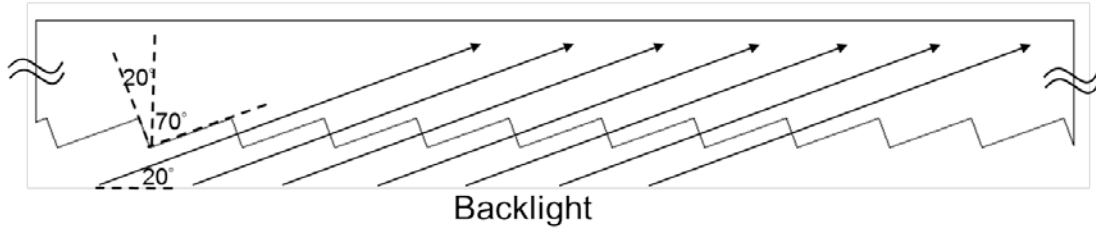
Figure 3.3 Device structure of the proposed VFS-BPLCD.

Figure 3.4(a) shows the structure of a bottom coupling film laminated on the bottom polarizer. It can substantially couple the oblique incident light to the bottom substrate and the

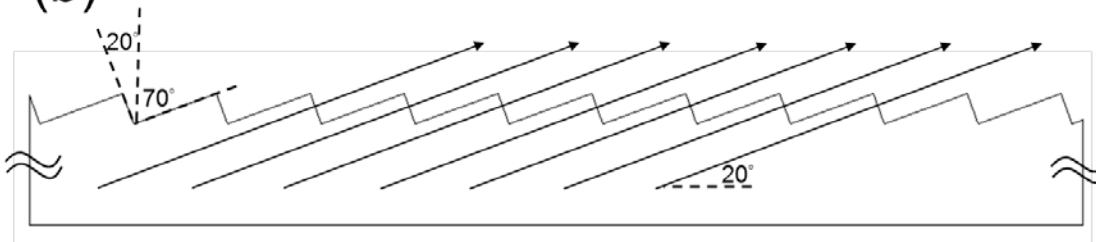
BPLC layer as well. The prismatic structure not only couples the oblique input light to the cell but also keeps a large incident angle in the BPLC layer. Without the bottom coupling film, the refraction angle in the BPLC layer will be reduced dramatically according to Snell's law. As a result, the phase retardation will be smaller and the operating voltage will be higher. Therefore, how to optimize the prism structure is important to the VFS mode. The prism pitch should be smaller than each pixel size of the LCD; it could range from $\sim 5\ \mu\text{m}$ to $\sim 50\ \mu\text{m}$.

Figure 3.4(b) shows the structure of a top coupling film. Without this top coupling film, the oblique light will be trapped in the cell module because of total internal reflection (TIR). Therefore, the major function of the top coupling film is to couple the oblique light to the air. The prism structures with internal angles of 70° - 20° - 90° can efficiently couple the light out of the substrate. A pair of top and bottom coupling films plays an important role on keeping a large incident angle in the VFS LCDs. Figure 3.4(c) depicts the structure of the turning film. It can steer the direction of the oblique light to the viewer's position by TIR without any energy loss. The pitch of the turning film is designed to be the same as that of the top coupling film. Therefore, the turning film can be easily laminated or placed on the top coupling film. Because the backlight that we used is well collimated, the turning film with regular prisms is suitable for the narrow-view application. The angle of the turning film should be optimized according to the profiles and angle of the backlight. To realize wide viewing angle, we can use irregular prism, or using the round shaped prisms to spread the light to multiple directions as shown in Figure 3.4(d). The round shaped prisms should provide a wider viewing angle and more uniform image. It should also be more durable than triangular prisms.

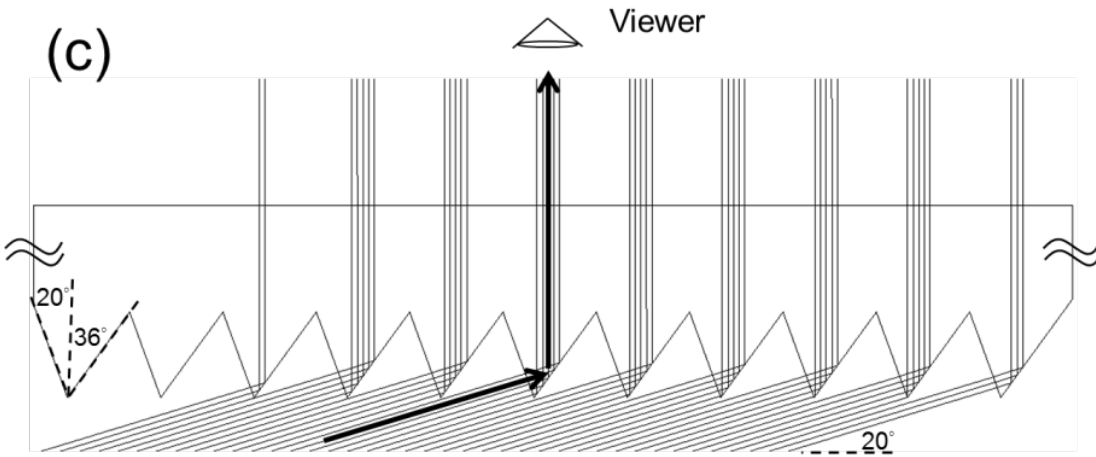
(a)



(b)



(c)



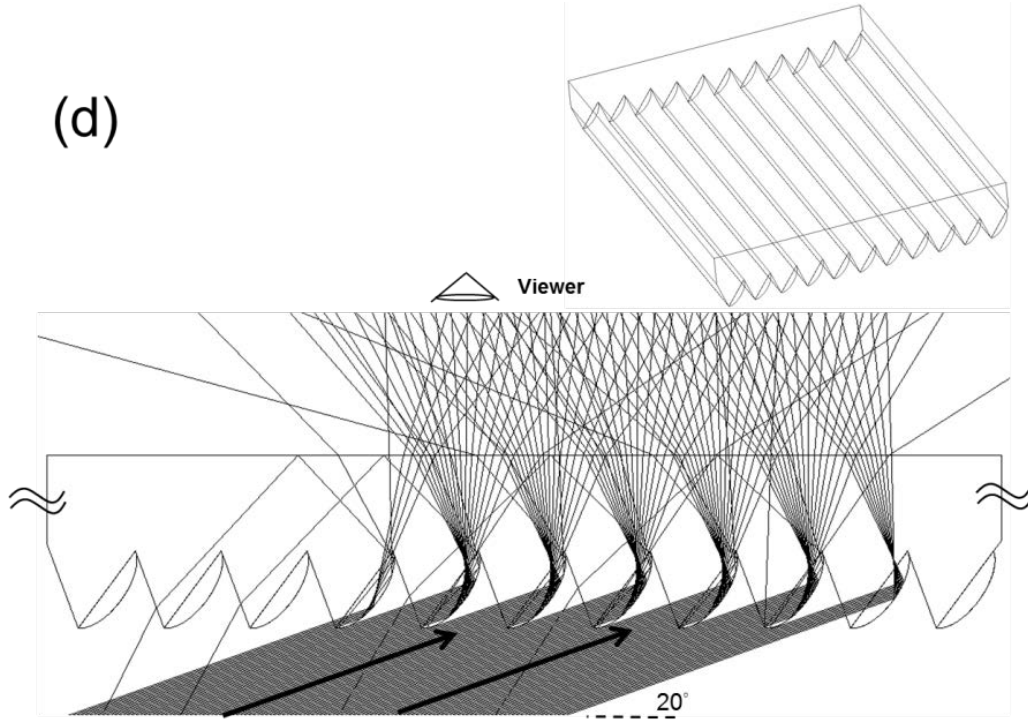


Figure 3.4 Structures of (a) bottom coupling film, (b) top coupling film, (c) turning film with regular-angle prisms, and (d) turning film with round shaped prisms.

3.3.2 Experiments and Simulations

We performed some experiments to confirm the advantages of our VFS device over the conventional planar IPS structure. Figure 3.5 shows our experimental setup. To simulate the beam path shown in Figure 3.3, we prepared a transparent container filled with Glycerol ($n=1.47$ @ $\lambda=633$ nm). The BPLC cell was immersed in Glycerol and it could be rotated freely. Because of matched index between glass and Glycerol, the light can pass through the BPLC without refraction and in a very large angle.

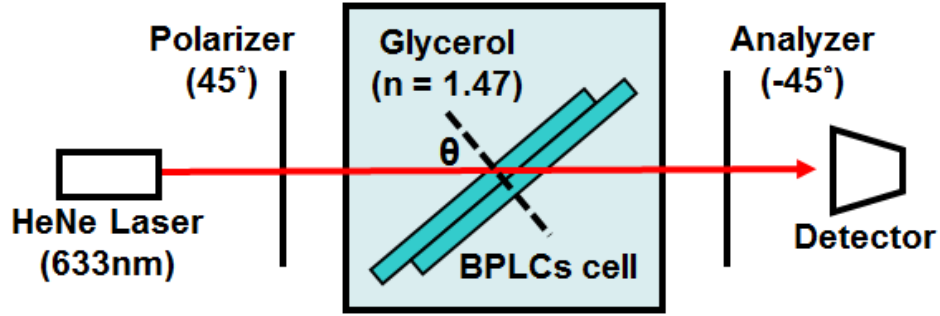


Figure 3.5 Experimental setup for characterizing the VFS cell.

We prepared a polymer-stabilized BPLC material from Chisso JC-BP01M [56]. The LC host has a dielectric anisotropy $\Delta\epsilon \sim 94$ and birefringence $\Delta n \sim 0.17$. The phase transition temperature of the precursor is BP 42.4°C N* during the cooling process and N* 44.5°C BP during the heating process, where N* denotes chiral nematic phase. The phase transition temperature between isotropic phase and blue phase was not easy to determine precisely because Bragg reflection occurred at ~ 350 nm. UV stabilization curing process was performed at 44°C for 30 min. with an intensity of 2 mW/cm^2 . After UV curing, the blue-phase temperature range was widened from $<0^\circ\text{C}$ to $\sim 70^\circ\text{C}$. To make a fair comparison, we used the same material for both IPS and VFS cells. The IPS cell has patterned ITO electrodes with $10 \mu\text{m}$ electrode width and $10 \mu\text{m}$ electrode gap, and $7.5 \mu\text{m}$ cell gap. For the VFS cell, both top and bottom glass substrates were coated with thin ITO electrodes; no polyimide layer was used. The cell gap we used was $d \sim 5.74 \mu\text{m}$.

Figure 3.6 depicts the measured voltage-dependent transmittance (VT) curves (at $\lambda = 633$ nm and $T \sim 23^\circ\text{C}$) of the IPS cell and VFS cell at $\theta = 70^\circ$. For the IPS cell measured at normal

incidence, the peak voltage occurs at $V_p \sim 50 V_{rms}$. For the VFS cell at $\theta=70^\circ$, its $V_p \sim 16 V_{rms}$ which is $\sim 3.2X$ lower than that of IPS structure. To further reduce operating voltage, we could use a larger Kerr constant BPLC or increase the incident angle.

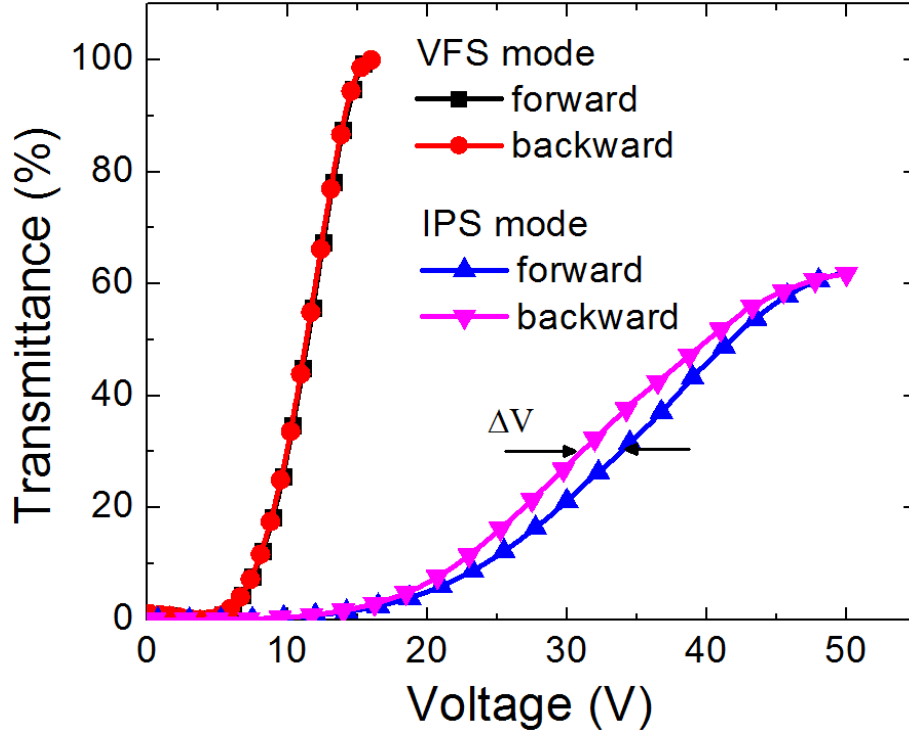


Figure 3.6 Measured VT curves and hysteresis of IPS and VFS cells. $\lambda=633$ nm.

Hysteresis is a common phenomenon for polymer-stabilized liquid crystal devices [46] [47]. For display applications, hysteresis affects the accuracy of grayscale control and should be eliminated. Hysteresis is defined by the voltage difference (ΔV) at half-maximum transmittance when we scan the voltage forward and backward. From Figure 3.6, the measured $\Delta V/V_p$ is $\sim 5.8\%$ for the IPS cell. For our new VFS cell with $d=5.74 \mu m$ and $\theta=70^\circ$, it is free from hysteresis! The reason is that our VFS cell has a weak electric field ($E \sim 2.8 V/\mu m$) so that the electrostriction effect does not occur. On the contrary, in an IPS cell the generated electric fields

are not uniform spatially. The electric fields are much stronger near the pixel edges than those in the electrode gap. The peak electric fields could cause lattice deformation locally which results in hysteresis.

To validate this hypothesis, we applied different voltages (up to 40 V_{rms}) to our VFS cell and measured their hysteresis at $\theta=70^\circ$. Figure 3.7 shows the field intensity versus corresponding phase retardation under the specified voltages. The black line represents the ascending curve, while red cycles, blue triangles, and green squares denote the descending curves from 40 V_{rms}, 28 V_{rms}, and 20 V_{rms}, respectively. From Figure 3.7, we find the accumulated phase increases almost linearly and then gradually saturates as the electric field exceeds $\sim 6\text{V}/\mu\text{m}$. For the $V=20\text{ V}_{\text{rms}}$ curve ($E\sim 3.5\text{ V}/\mu\text{m}$ in our $5.74\text{-}\mu\text{m}$ VFS cell), the forward and backward curves overlap very well and no hysteresis is observed. Therefore, the critical field (E_c) for a hysteresis-free BPLC using Chisso JC-BP01M is $\sim 3.5\text{ V}/\mu\text{m}$. In our VFS cell, the electric field is uniform, thus it provides a reliable way for determining the critical field for a PS BPLC. On the other hand, for an IPS cell the electric field near electrode edges is often higher than $3.5\text{ V}/\mu\text{m}$ so that it exhibits a noticeable hysteresis.

Residual birefringence is another serious problem for IPS BP-LCDs [57]. It causes light leakage at dark state and degrades the contrast ratio. In an IPS cell, the residual birefringence arises in the region with strong field. In a VFS cell, the required field intensity for producing 1π phase retardation is relatively weak. Thus, the resultant residual birefringence is negligible.

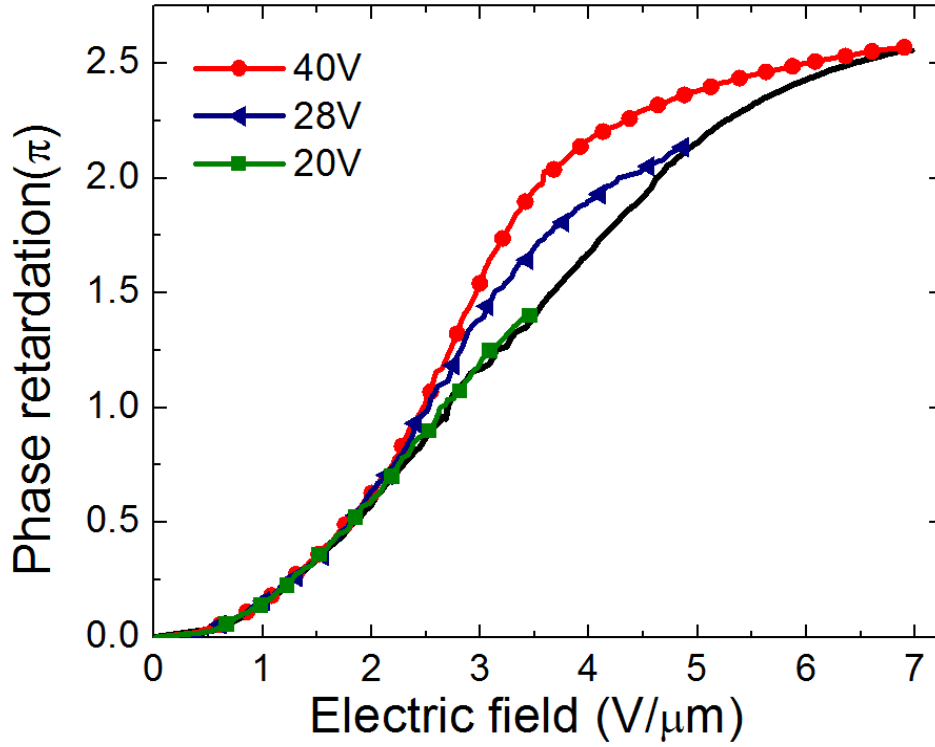


Figure 3.7 Measured phase retardation vs. electric field intensity under different applied voltages.
 $\lambda=633$ nm.

We also compared the response time of our VFS cell with IPS cell at 23°C. Figure 3.8(a) shows the gray-to-gray response time of the IPS cell while Figure 3.8(b) shows the measured response time of our new VFS cell. The applied voltage swings from 0 to 16 V_{rms} (@ 100Hz) for the VFS cell, and 0 to ~46 V_{rms} for the IPS cell. We find that IPS cell has a very slow rise time especially in the low gray level transition. Our VFS mode shows much faster rise time and fall time as compared to the IPS cell. Again, this is attributed to the smaller LC reorientation angle and uniform field of the VFS cell.

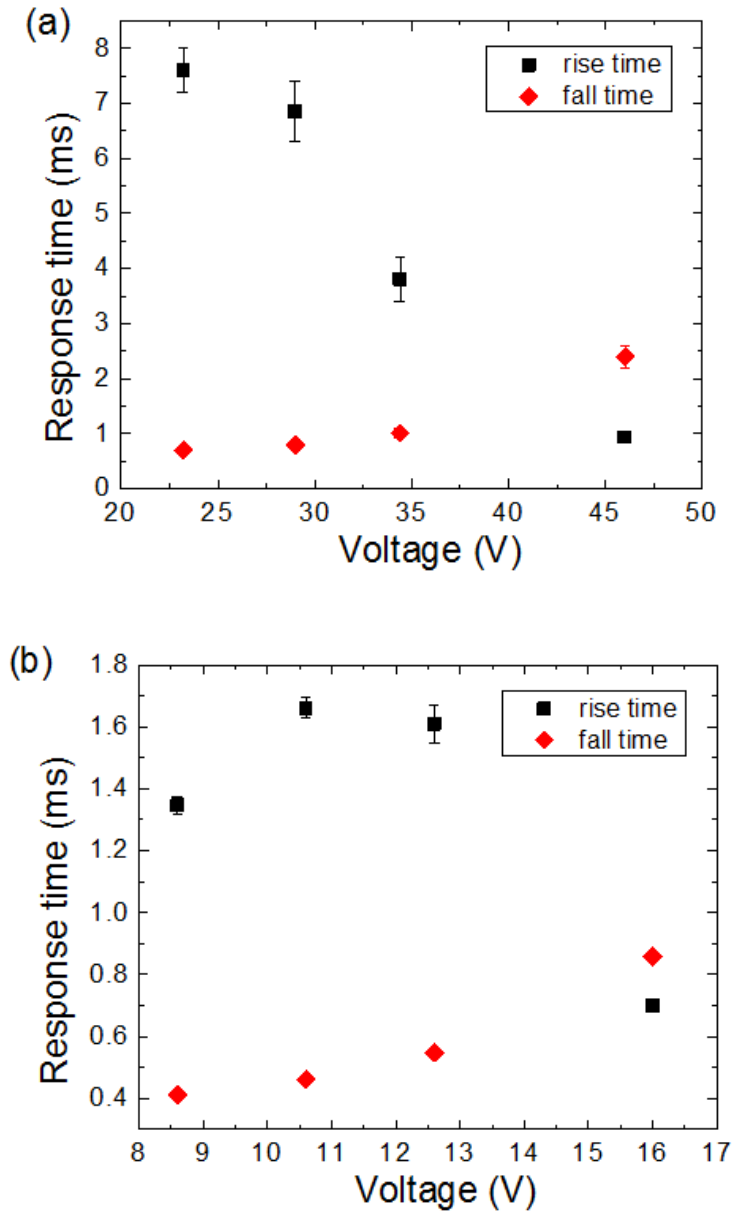


Figure 3.8 Measured response time of (a) IPS cell and (b) VFS cell. $\lambda=633$ nm.

Unlike an IPS cell whose VT curve is insensitive to the cell gap, the peak transmittance voltage of our VFS cell is dependent on the cell gap. Here, two factors have to be considered: induced birefringence and effective cell gap. At a given voltage V , as the cell gap d decreases the

electric field E gets stronger because $E=V/d$. According to Kerr effect, the induced birefringence is proportional to E^2 . Thus, the induced birefringence is larger as the cell gap decreases. On the other hand, for a given incident angle the beam path in the BPLC cell for accumulating phase retardation decreases as the cell gap decreases. Therefore, there ought to be an optimal cell gap for achieving certain phase retardation. If the cell gap is too thin, although the induced birefringence is large, the optical beam path is decreased so that the accumulated phase may not be adequate for achieving maximum transmittance. Moreover, the saturation phenomenon in the high field region should be also considered. In a real situation, the induced birefringence will gradually saturate as the electric field increases. Therefore, the driving voltage could not decrease indefinitely when we use an ultra-thin cell gap, as described by the extended Kerr effect equation [58].

In the extended Kerr effect model, the induced birefringence is expressed as follows:

$$\Delta n = \Delta n_{sat} \left(1 - \exp \left[- \left(\frac{E}{E_s} \right)^2 \right] \right), \quad (1.2)$$

where Δn_{sat} stands for the saturated induced birefringence and E_s represents the saturation field. From the measured results in Figure 3.6, our PS-BPLC material has $K \sim 7.5 \text{ nm/V}^2$ at $\lambda = 633 \text{ nm}$ in the low field region, with $\Delta n_{sat} \sim 0.17$ and $E_s \sim 6.0 \text{ V}/\mu\text{m}$. The Kerr constant extracted from VFS cell is $\sim 70\%$ smaller than that from IPS cell. A possible explanation is as follows. In an IPS cell, the electric field varies largely from electrode edges to the center of electrode gap. Therefore, the extracted Kerr constant thru curve fitting has a larger uncertainty.

Figure 3.9 shows the simulated VT curves for $d = 5\mu\text{m}$, $2\mu\text{m}$, and $1\mu\text{m}$ at $\lambda = 550 \text{ nm}$. For display applications, we often optimize the device design at $\lambda = 550 \text{ nm}$. To obtain the Kerr

constant at this wavelength, we use the value measured at $\lambda=633$ nm and then extrapolate it following the dispersion relation [59]. For the 1- μm BPLC cell, the induced birefringence gradually saturates so that the maximum phase retardation reaches $\sim 1\pi$ at a fairly high voltage. As compared to the IPS structure whose VT curve is insensitive to the cell gap, the electro-optic effects of VFS are dependent on the cell gap. We can optimize the cell gap according to the material properties and incident angle to obtain a proper operation voltage. If we would compromise for a lower transmittance, we could use a thinner cell gap to trade for a lower operating voltage. For example, from Figure 3.9 the 1- μm VFS cell has an operating voltage of $6 V_{\text{rms}}$ at 70% transmittance, which is the typical transmittance of an IPS cell. If we want to boost the transmittance to 90% for the 1- μm VFS cell, then we can increase the operating voltage to $7.7 V_{\text{rms}}$. A caution should be taken that if we use a thinner cell gap to reduce driving voltage, the electric field might exceed the critical field (E_c) for causing hysteresis. The critical voltage for the 5 μm , 2 μm , and 1 μm cells is $17.5 V_{\text{rms}}$, $7.0 V_{\text{rms}}$, and $3.5 V_{\text{rms}}$, respectively.

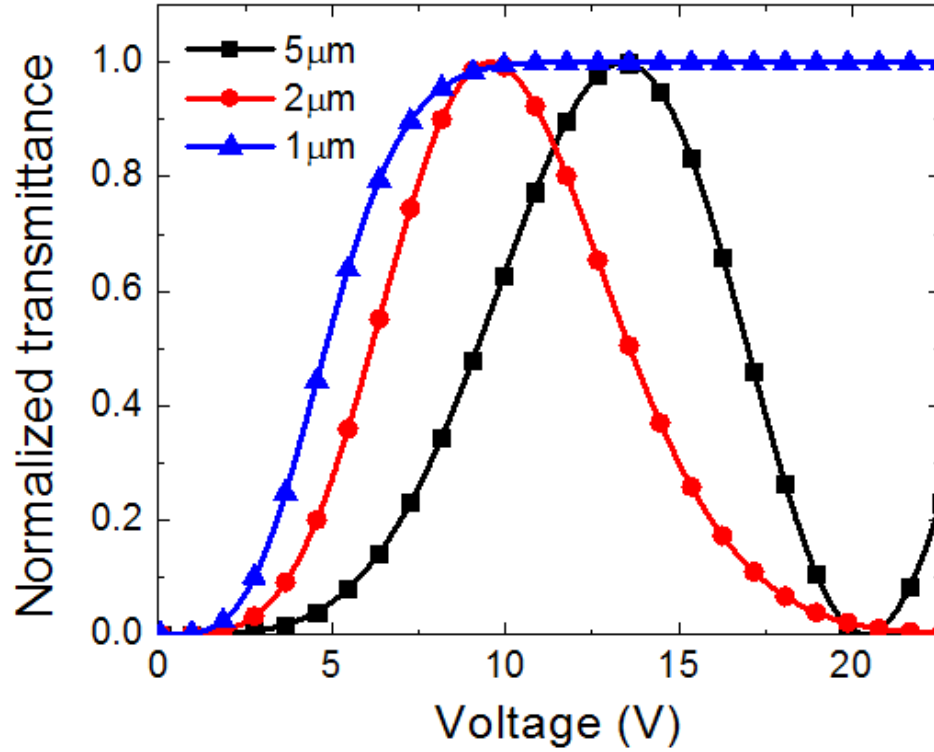


Figure 3.9 Simulated VT curves under different cell gap ($d=1\mu\text{m}$, $2\mu\text{m}$, and $5\mu\text{m}$) for the VFS cell. Incident angle= 70° and $\lambda=550\text{nm}$.

Based on the extended Kerr effect, we simulated the cell gap versus the driving voltage at $\lambda=550\text{ nm}$ as shown in Figure 3.10. As the cell gap decreases, the driving voltage decreases and then reaches a minimum. For the case of $\theta=70^\circ$ and $d\sim 1.5\mu\text{m}$, the minimum peak voltage occurs at $V_p\sim 9\text{ V}_{\text{rms}}$. As stated above, we can optimize cell gap according to the material properties and incident angle to obtain the minimum voltage. For the BPLC layer under a longitudinal field, the induced birefringence Δn is along the electric field and behaves as a C-plate [60]. The phase retardation Γ equals 1π for the first maximum transmittance and can be expressed as:

$$\Gamma = \frac{2\pi}{\lambda} n_o d \left[\sqrt{1 - \frac{(n_g \sin \theta_0)^2}{n_e^2}} - \sqrt{1 - \frac{(n_g \sin \theta_0)^2}{n_o^2}} \right] = \pi, \quad (1.3)$$

where d is the cell gap, n_g is the refractive index of Glycerol (Figure 3.5), θ_0 is the incident angle, and n_o and n_e are the ordinary and extraordinary refractive indices of the BPLC. We also assume the following equations hold for n_o and n_e [20]:

$$n_o = n_i - \frac{1}{3} \Delta n; n_e = n_i + \frac{2}{3} \Delta n, \quad (1.4)$$

where n_i is the isotropic refractive index of BPLC in the voltage-off state, and Δn is the induced birefringence under an external electric field. After combining equations (1.2), (1.3), and (1.4), we derive (by neglecting algebraic derivation) following analytical solution of cell gap d for the minimum operating voltage:

$$d = \frac{\lambda n_i \sqrt{n_i^2 - n_g^2 \sin^2 \theta}}{n_g^2 \sin^2 \theta \cdot \Delta n_s (\sqrt{5} - 1)}, \quad (1.5)$$

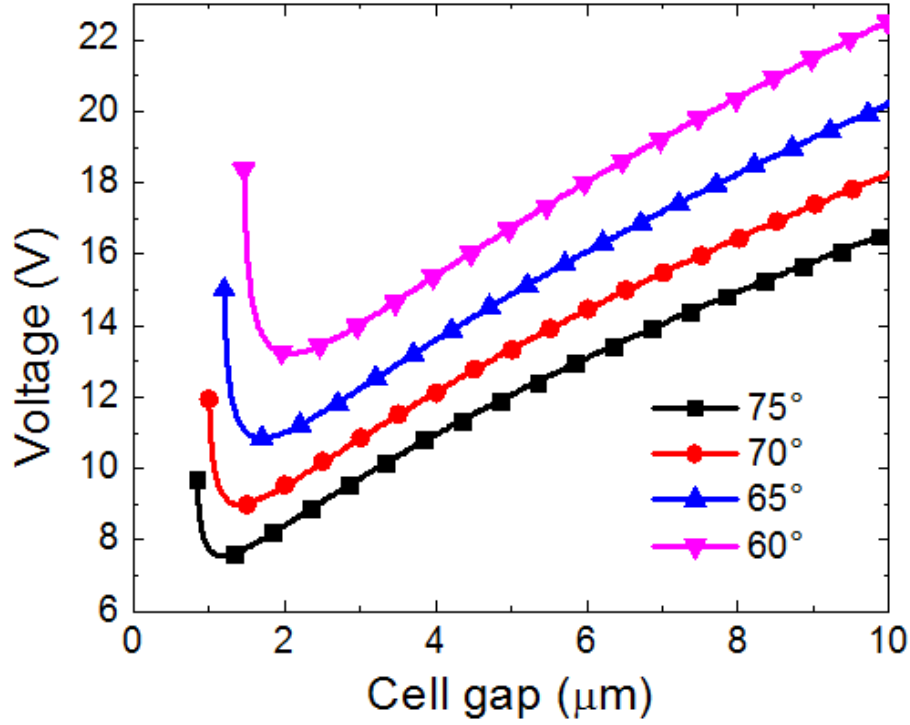


Figure 3.10 Simulated operating voltage vs. cell gap at different incident angles of VFS cells.
 $\lambda=550$ nm and Kerr constant is assumed to be $K \sim 7.5$ nm/V².

The operating voltage is roughly proportional to the inverse square root of Kerr constant under low fields [31] [58]. From Kerr effect equation, we can get Kerr constant $K = \Delta n_s / (\lambda E_s^2)$. Therefore, BPLC materials with high Δn_s and low E_s are crucial for enhancing Kerr constant, which subsequently corresponds to the lower operation voltage. Figure 3.11 shows the operating voltage versus cell gap with different Kerr constants. The incident angle is 70° and the wavelength is $\lambda=550$ nm. The cyan squares, blue triangles, and red circles denote the same Kerr constant but with different Δn_s and E_s respectively. When the Kerr constant is doubled (i.e. $K=15$ nm/V² at $\lambda=633$ nm), the operating voltage is reduced from ~ 10.9 V_{rms} to ~ 7.4 V_{rms} in a 3- μ m cell gap. We notice that if we can use a BPLC with high Δn_s in an ultra-thin cell gap (e.g. ~ 1.1

μm), the driving voltage could be further reduced to below 5V. To get such a large Δn_s , the host LC should have a fairly high birefringence. However, this kind of liquid crystal usually has UV stability issue and high viscosity which is unfavorable for response time. Another strategy to get large Kerr constant is to reduce E_s by using materials with a large dielectric anisotropy which would also inevitably increase the viscosity. Therefore, how to lower the operation voltage while keeping fast response time remains a critical challenge for future BPLC development.

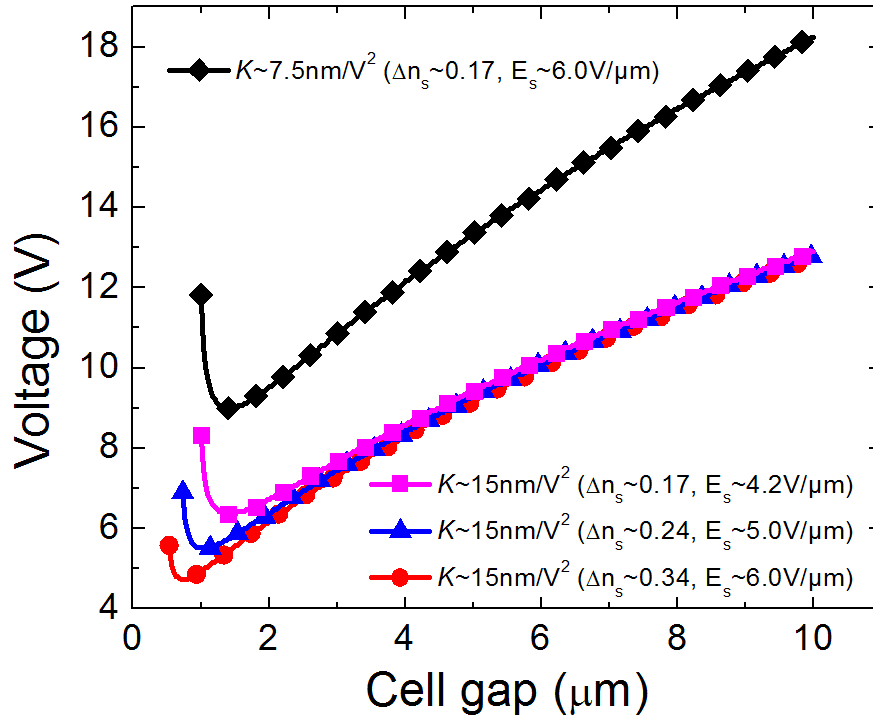


Figure 3.11 Simulated operating voltage vs. cell gap with different Kerr constants.

The optical efficiency (normalized to two parallel polarizers) of an IPS BPLC cell is generally limited to $\sim 70\%$ due to some dead zones above the electrodes. Our VFS cell could in principle achieve 100% transmittance because of its uniform vertical fields without dead zones. The major optical loss comes from Fresnel reflection of the coupling films and turning films.

From our simulations, the optical efficiency for the employed films is over 85%. Crosstalk between two adjacent pixels would also affect the transmittance of our VFS BPLC. As shown in Figure 3.12, the width W of crosstalk equals $d/\cot\theta$, here d is the cell gap, and θ is the incident angle. Therefore, the transmittance ratio becomes $1-W/p$, here p is each pixel width. Let us assume $d=3\mu\text{m}$, $\theta=70^\circ$, and $p=180\mu\text{m}$, the transmittance would be 95%. We can fabricate TFT structure in the crosstalk region and add black matrix on it. Therefore, VFS should have a comparable or higher optical efficiency than IPS.

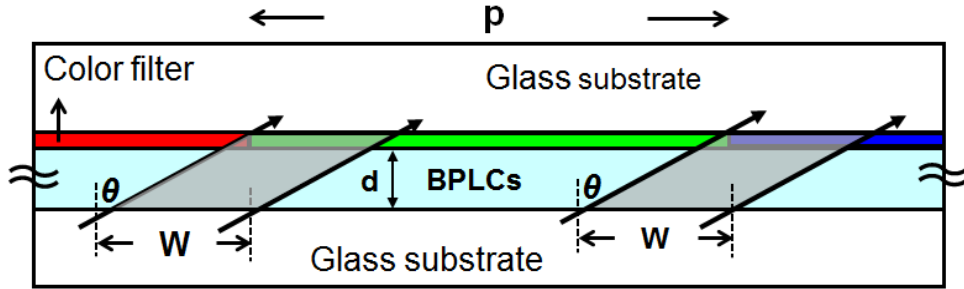


Figure 3.12 Possible crosstalk in a VFS BPLCD.

Achieving wide viewing angle is a major challenge for the VFS mode. Because the backlight's incident angle is fairly large through the polarizer and analyzer, the extinction ratio of polarizer and analyzer degrade dramatically. As a result, the intrinsic contrast ratio is very poor for the case of oblique incident light in VFS BPLCD. We need to design some phase compensation methods and retardation films to improve the intrinsic contrast ratio. Since we adopt the directional backlight with fairly narrow FWHM for VFS BPLCDs, this design is suitable for narrow-view applications. To widen the viewing angle, we can design the irregular prism structure of turning film [53] or a front diffuser [61] to orient and steer backlight to different viewing angles. We can also add a polymer-dispersed liquid crystal (PDLC) [62] [63]

layer in front of the panel to work as a dynamic diffuser. The scattering degree of the PDLC layer can be controlled by the applied voltage. Therefore, we can realize the tunable viewing angle display which is suitable for both private and public environments.

3.4 Summary

The VFS mode offers superior performances to IPS in lower operating voltage, higher transmittance, free from hysteresis, no residual birefringence, and faster response time. Its cell structure is very simple, but it requires sophisticated phase compensation scheme to achieve wide view. On the other hand, IPS requires protrusion electrodes to reduce operation voltage, but its phase compensation scheme for achieving wide view is relatively simple. The VFS mode is particularly attractive for displays and photonic devices that require fast response time.

CHAPTER 4: WIDE VIEWING ANGLE OF VFS BPLCD

From our introductions in the previous chapters, most BPLC devices utilize planar IPS or protruded IPS. Planar IPS has wide view, but its operating voltage is high and hysteresis is fairly large because the lateral field is spatially nonuniform and the peak electric field near electrode edges is high. Protruded electrodes lower the operation voltage, but the tradeoff is increased fabrication complexity.

To overcome the fabrication problem, we proposed vertical field switching (VFS) for BPLCDs. With this novel VFS mode, the operating voltage is greatly reduced and hysteresis is completely suppressed. However, how to achieve wide view becomes a challenge.

In this chapter, we present several approaches for improving the contrast ratio (CR) and viewing angle of VFS BPLCDs. We also analyze the pros and cons of each method.

4.1 Light Leakage in VFS BPLCD

Figure 4.1 depicts the angular distribution of the directional backlight [54] [55] for VFS BPLCDs. A directional backlight with oblique output ($\theta \sim 70^\circ$) is adopted. A larger incident angle results in a larger phase retardation which helps to lower the operating voltage. Typically, the directional backlight has a divergence angle (full width at half maximum FWHM) smaller than 20° . The more collimated backlight is preferred, but we also need to consider the optical efficiency and brightness uniformity.

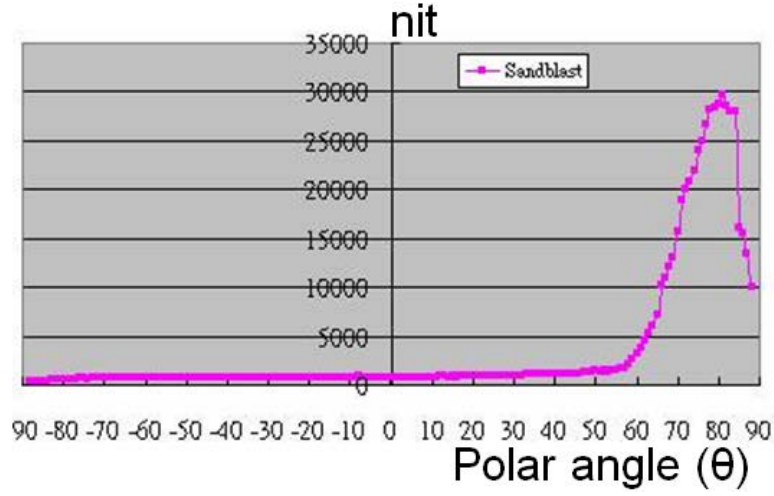


Figure 4.1 Directional backlight's angular distribution.

The polar coordinate in our device and simulations is defined in Figure 4.2. Because the backlight passes the polarizer and analyzer obliquely ($\theta \sim 70^\circ$, $\phi \sim 270^\circ$), there is light leakage at the dark state if the polarizer and analyzer are set at $\phi = 45^\circ$ and -45° as a conventional LCD [64]. To minimize light leakage, we can rotate the absorption axes of polarizer and analyzer along $\phi = 71.12^\circ$ and -71.12° respectively as shown in Figure 4.3(a), in which the polarizer and the analyzer are crossed at the backlight angle ($\theta = 70^\circ$, $\phi = 270^\circ$) as Figure 4.3(b) shows.

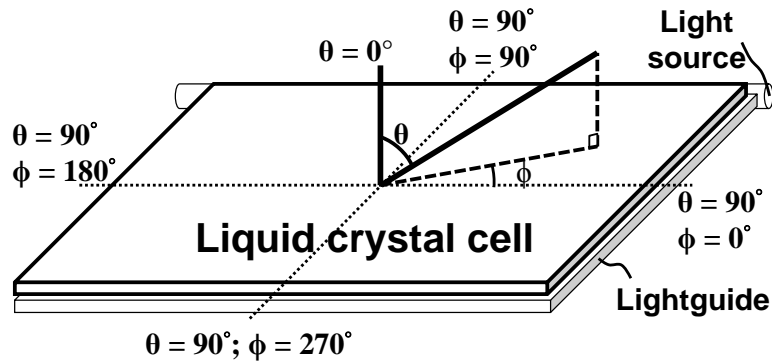


Figure 4.2 Polar coordinate of the VFS-BPLCD.

We used commercial software, LCD Master (Shintech), and Nitto Denko's polarizer and analyzer (SEG1425DU) in our simulations. The BPLC composite is optically isotropic with $n_i=1.55$ at the voltage-off state. As the voltage increases, Kerr effect-induced birefringence gradually increases. At $V=16 \text{ V}_{\text{rms}}$ in which the phase retardation $\delta=\pi$ at 70° incident angle of our VFS cell, the measured $n_o=1.54$ and $n_e=1.57$ at $\lambda=633 \text{ nm}$. The cell gap is $4.74\mu\text{m}$. Figure 4.3(c) shows the simulated isocontrast contours of Figure 4.3(b) after the incident oblique backlight is steered to the normal direction by a turning film. Although the polarizer and analyzer are crossed at $(\theta=70^\circ, \phi=270^\circ)$, the intrinsic CR is much lower than that of the crossed polarizers at normal incidence. Because the extinction ratio of the analyzer decreases drastically as the polar angle θ increases, in which the smaller effective absorption coefficient causes light leakage in the dark state. Therefore, how to enhance the intrinsic CR and widen the isocontrast contours becomes an urgent task for VFS BPLCDs.

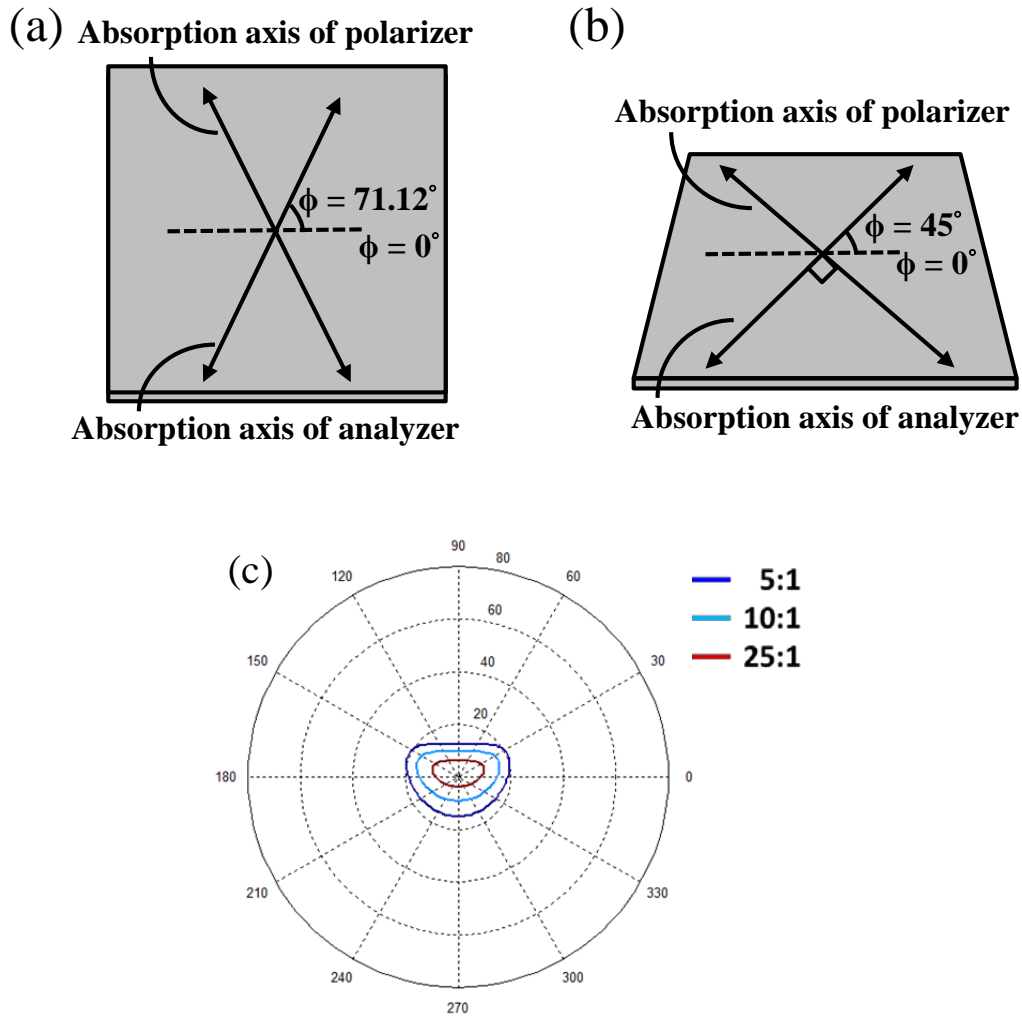


Figure 4.3 Change in the effective angle between the polarizer and the analyzer: (a) normal observation ($\theta=0^\circ$), (b) oblique observation ($\theta=70^\circ$); (c) simulated isocontrast contours.

4.2 Film Compensation Principles

As plotted in Figure 4.3(c), the polarizer and analyzer at $\phi=71.12^\circ$ and -71.12° leads to a fairly poor contrast ratio and narrow viewing angle. We could design retardation films to widen the isocontrast contours. However, the maximum CR (or the intrinsic CR) is not improved. On

the other hand, we could reduce the azimuthal angle ϕ to enhance the effective absorption coefficient and improve the intrinsic CR. In this case, the polarizer and analyzer are not mutually perpendicular at the viewing angle of $\theta=70^\circ$ and $\phi=270^\circ$. It would be even harder to design the phase compensation films to widen the isocontrast contour for a small ϕ . According to our experience, we should find a balance between high CR and wide isocontrast contour by choosing a proper ϕ between the polarizer and the analyzer.

Figure 4.4(a) shows our first proposed optical configuration for VFS BPLCD. The absorption axes of polarizer and analyzer are along $\phi = 45^\circ$ and -45° respectively. Because the effective angles between polarizer and analyzer become 12.88° and -12.88° rather than mutually perpendicular at oblique incident angle ($\theta=70^\circ$, $\phi=270^\circ$), the noticeable light leakage degrades the CR dramatically. We add two identical biaxial films set at $\phi=38.5^\circ$ and -38.5° to reduce the light leakage. The N_z factor, which is defined as $(n_x - n_z)/(n_x - n_y)$, is 0.54 for both biaxial films, and $d(n_x - n_y) = 256$ nm, here d is the biaxial film thickness.

Figure 4.4(b) shows the compensation process for the dark state on the Poincaré sphere. At normal incidence, i.e., $\theta=0^\circ$, the polarization state after polarizer P_0 is the same as the absorption axis of analyzer A_0 . However, the effective angle between the polarizer and the analyzer changes as the incident backlight tilts away from normal (e.g., $\theta=70^\circ$, $\phi=270^\circ$). Therefore, the transmittance state P_1 deviates from analyzer A_1 and the light leakage happens. We add two biaxial films to compensate the separation of P_1 from A_1 . Biaxial film 1 shifts the polarization state from P_1 to P_0 , and subsequently biaxial film 2 moves the polarization state from P_0 to A_1 . As a result, light leakage is suppressed substantially. Figure 4.4(c) shows the simulated CR and isocontrast contours optimized at incident angle ($\theta=70^\circ$, $\phi=270^\circ$) for $\lambda=550$

nm. From Figure 4.4(c), CR>1000:1 covers $\sim 10^\circ$ viewing cone which is sufficient for the employed directional backlight (FWHM $< 20^\circ$) in our VFS BPLCD. In order to widen the viewing angle, a front diffuser [61] [65] or a curve shaped turning film [53] can be applied to spread the directional backlight to the observer for achieving wide view.

Figure 4.4(d) shows the simulated isocontrast contours and optical configuration which is optimized for a smaller incident polar angle $\theta=60^\circ$, $\phi=270^\circ$. The polarizer and analyzer are still set at $\phi=45^\circ$ and -45° . Two identical biaxial films ($N_z=0.63$, $d(n_x-n_y)=260$ nm) are set at $\phi=42^\circ$ and -42° . Under a smaller polar angle θ , Figure 4.4(d) shows wider isocontrast contours as compared to Figure 4.4(c). However, a smaller incident angle θ corresponds to a lower induced birefringence of a VFS BPLC which leads to a higher operating voltage. Recently, Merck reported a high Kerr-constant BPLC material [66]. If we use this material, we can choose a smaller incident angle to obtain 1π phase retardation. A smaller incident angle helps to enlarge the isocontrast contours.

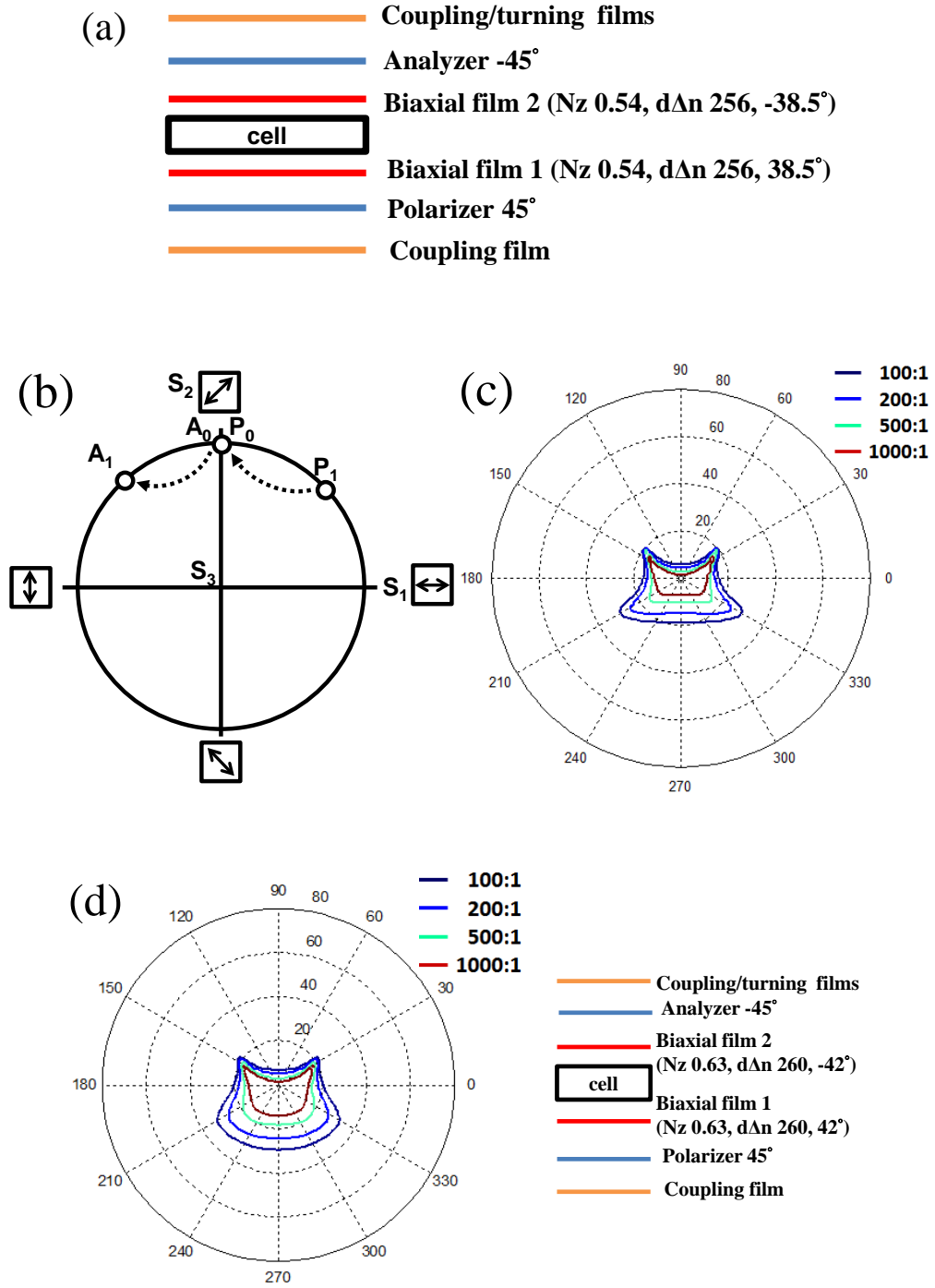


Figure 4.4 Biaxial film-compensated VFS BPLCD: (a) device configuration, (b) compensation principle on Poincare sphere, and simulated isocontrast contours at incident angle $\theta=70^\circ$ (c) and $\theta=60^\circ$ (d). $\lambda=550$ nm.

Let us return to the backlight angle ($\theta=70^\circ$, $\phi=270^\circ$) but varying the polarizer/analyzer angle. Figure 4.5(a) shows the isocontrast contours at a smaller angle ($\phi=40^\circ$ and -40°) between the polarizer and the analyzer. Two biaxial films ($N_z=0.506$, $d(n_x-n_y)=259$ nm) are set at $\phi=36^\circ$ and -36° . Figure 4.5(b) shows the isocontrast contours when the polarizer and the analyzer are further reduced to $\phi=30^\circ$ and -30° . The incident angle of backlight is still at ($\theta=70^\circ$, $\phi=270^\circ$). Two biaxial films ($N_z=0.44$, $d(n_x-n_y)=264$ nm) are set at $\phi=31^\circ$ and -31° . Comparing Figure 4.4(c), Figure 4.5(a), and Figure 4.5(b), we find the contour size for CR=1000:1 is similar but the contour shape changes as the absorption angle ϕ between the polarizer and analyzer varies. For practical applications, we should also consider the output profile of the directional backlight in order to choose an appropriate ϕ and the matched contour shape.

Figure 4.6 shows the isocontrast contours optimized for a smaller incident polar angle ($\theta=60^\circ$, $\phi=270^\circ$). The polarizer and the analyzer are set at $\phi=30^\circ$ and -30° . Two identical biaxial films ($N_z=0.4775$, $d(n_x-n_y)=264.5$ nm) are set at $\phi=32.5^\circ$ and -32.5° . From Figure 4.4(d) and Figure 4.6, a smaller incident polar angle could result in larger contours.

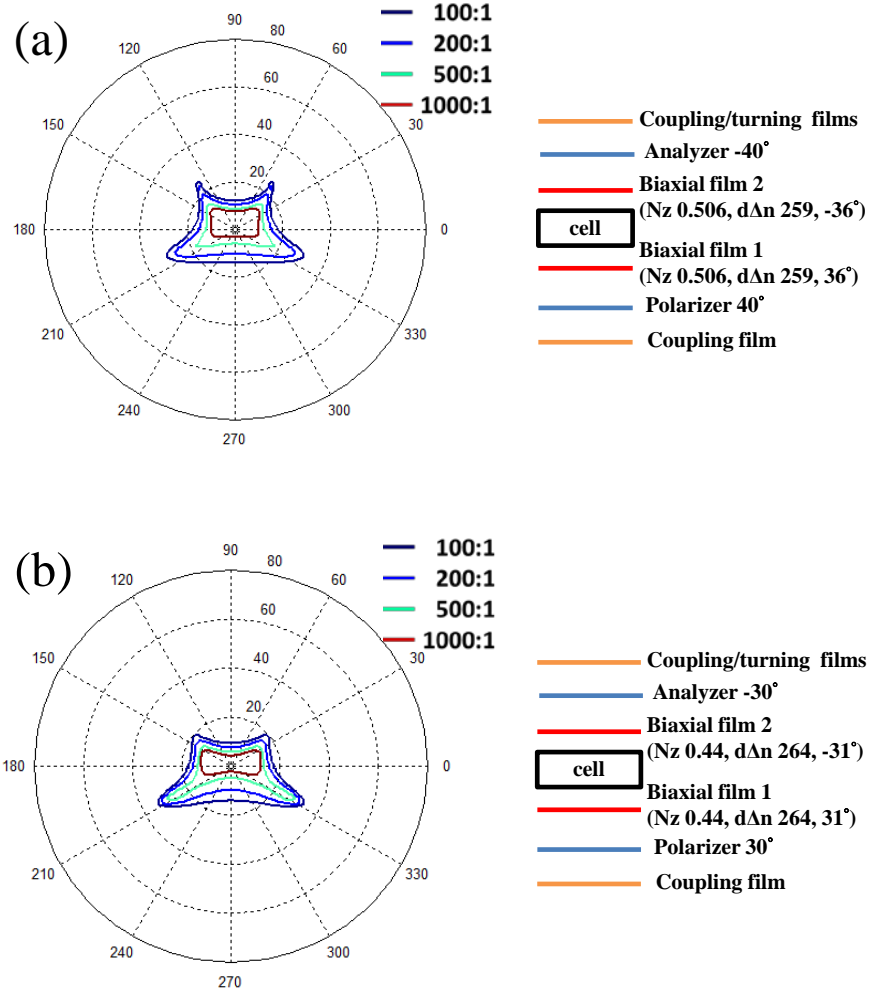


Figure 4.5 Simulated isocontrast contours of biaxial film-compensated VFS BPLCD: (a) $\phi=40^\circ$ and -40° and (b) $\phi=30^\circ$ and -30° .

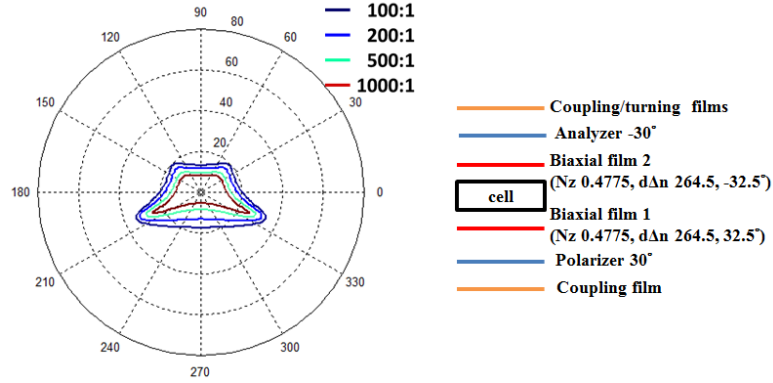


Figure 4.6 Isocontrast contours and film configurations of a VFS BPLCD with incident angle $\theta=60^\circ$.

Figure 4.7(a) shows another compensation method by adding four biaxial films. The polarizer and the analyzer are set at $\phi=30^\circ$ and -30° . Two identical biaxial films 1 and 4 ($N_z=0.851$, $d(n_x-n_y)=281\text{nm}$) are set at $\phi=25.75^\circ$ and -25.75° . Identical biaxial films 2 and 3 ($N_z=0.3984$, $d(n_x-n_y)=272\text{nm}$) are set at $\phi=29.72^\circ$ and -29.72° . The compensation process is shown on the Poincaré sphere in Figure 4.7(b). As compared with previous examples, the additional two biaxial films are designed to compensate the varied effective angle between the polarizer and the analyzer due to different azimuthal angle ϕ . P_2 denotes the polarization state at $\theta=70^\circ$, $\phi=300^\circ$. P_2 deviates from P_1 which represents the transmittance state at $\theta=70^\circ$, $\phi=270^\circ$. The biaxial film 1 can compensate the effect of varied ϕ and shift the polarization state from P_2 to P_1 . The biaxial films 2 and 3 shift the polarization state from P_1 to A_1 . Finally, the biaxial film 4 shifts the polarization state to absorption axis of the analyzer A_2 . Figure 4.7(c) shows the CR contours. Because of two additional biaxial films to compensate the effect of varied azimuthal angle ϕ , the CR contours exhibit a more circular shape which is similar to the output profile of the direction backlight.

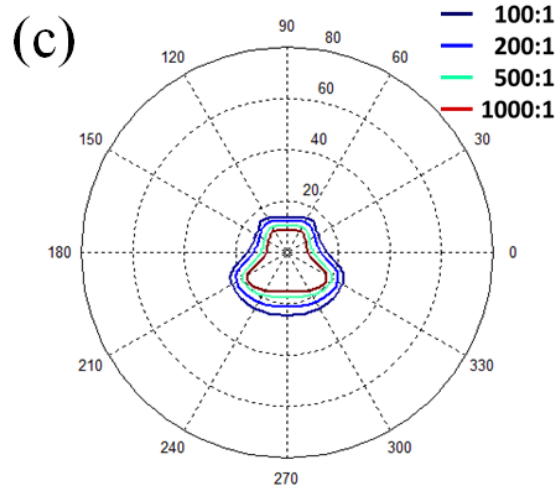
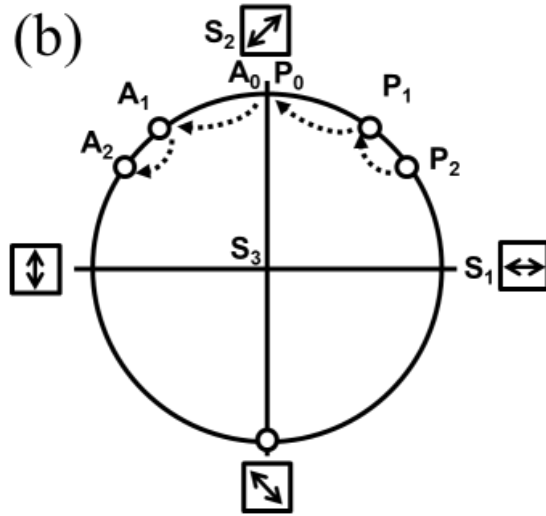
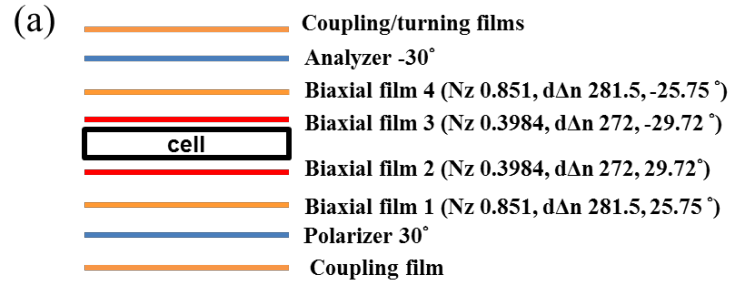


Figure 4.7 Optical configuration of the proposed VFS BPLCD: (a) film configuration, (b) compensation principle, and (c) isocontrast contours.

Figure 4.8(a) shows another example of four biaxial films. The polarizer and analyzer are set at $\phi=45^\circ$ and -45° . The biaxial films 1 and 4 ($N_z=0.575$, $d(n_x-n_y)=256$ nm) are set at $\phi=40^\circ$ and -40° . The biaxial films 2 and 3 ($N_z=0.5$, $d(n_x-n_y)=137$ nm) are set at $\phi=90^\circ$ and $\phi=0^\circ$, respectively. From the Poincaré sphere in Figure 4.8(b), biaxial film 1 shifts the polarization state from P_1 to P_0 . Biaxial film 2 shifts the linear polarization state P_0 to circular polarization C_1 , and then biaxial film 3 changes the circular polarization C_1 back to linear P_0 . Finally the biaxial film 4 rotates the transmission state P_0 to align with the absorption axis of analyzer A_1 . Here, P_0 and A_0 are for the normal incident $\theta=0^\circ$. P_1 and A_1 deviate from P_0 and A_0 due to the oblique incidence ($\theta=70^\circ$, $\phi=270^\circ$) of the directional backlight.

Because the circularly polarized light C_1 is independent of the azimuthal angle ϕ in the BPLC material, it helps to improve the brightness state of the VFS BPLCD. Actually, we also tried to use one biaxial film to shift the polarization state from P_1 to C_1 directly and another biaxial film to shift the polarization state from C_1 to A_1 . However, this simpler configuration is very sensitive to the polar angle θ and our results are not promising. Figure 4.8(c) shows the isocontrast contours when the directional backlight is at ($\theta=70^\circ$, $\phi=270^\circ$). Figure 4.8(d) shows the isocontrast contours optimized for the incident angle ($\theta=60^\circ$, $\phi=270^\circ$) of the directional backlight. The polarizer and the analyzer are set along $\phi=45^\circ$ and -45° . The biaxial films 1 and 4 ($N_z=0.63$ and $d(n_x-n_y)=260$ nm) are set at $\phi=42^\circ$ and -42° . The biaxial films 2 and 3 ($N_z=0.5$ and $d(n_x-n_y)=137$ nm) are set at $\phi=90^\circ$ and 0° , respectively. Figure 4.8(d) exhibits wider isocontrast contours than Figure 4.8(c) because of the smaller incident angle.

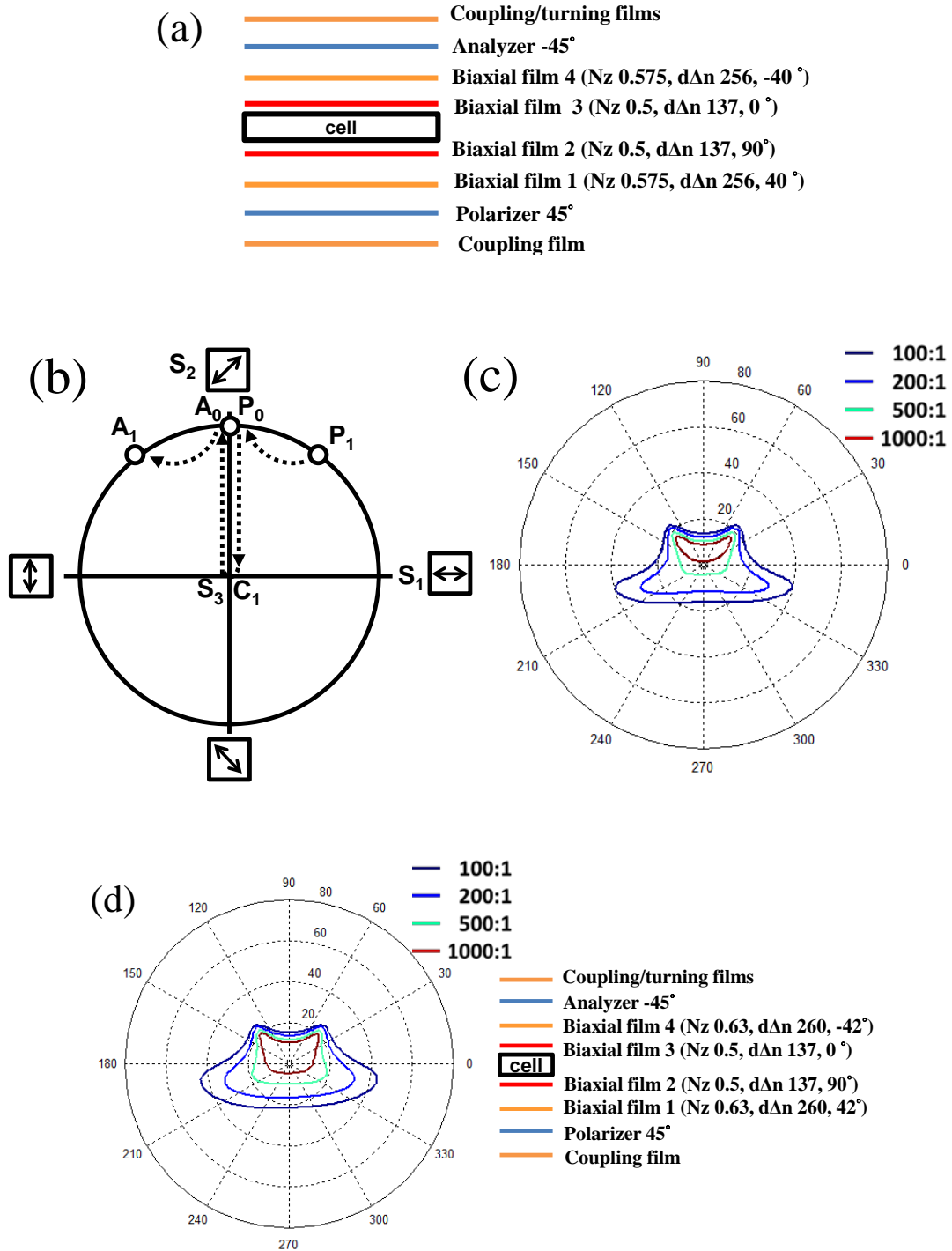


Figure 4.8 Optical configuration of a VFS BPLCD with 4 biaxial films: (a) film configuration, (b) compensation principle, and simulated isocontrast contours at $\theta=70^\circ$ (c) and $\theta=60^\circ$ (d).

In all the above examples, the backlight passes the analyzer obliquely. If the coupling film and turning film are laminated between the analyzer and the BPLC cell, the light would pass the analyzer at normal angle and the analyzer would exhibit a good extinction ratio. Moreover, better image quality can be obtained if the coupling film and turning film are closer to the image plane (i.e., pixels of the LCD panel). Similarly, if we can place the polarizer outside the bottom coupling film [Figure 4.9(a)], the directional backlight travels inside the polarizer at a smaller angle according to Snell's law. Hence, the extinction ratio of the polarizers and the device CR are all improved. A tradeoff is that the backlight might be depolarized by the turning films and the coupling film. As a result, we need additional retardation films to compensate for the depolarization effect.

Figure 4.9(a) shows the schematic view of our approach. The polarizer and analyzer are at $\phi=0^\circ$ and 90° , respectively. A biaxial film 1 ($N_z=0.756$, $d(n_x-n_y)=254$ nm) is set $\phi=0^\circ$. The biaxial films 2 and 3 ($N_z=0.501$, $d(n_x-n_y)=137.5$ nm) are set $\phi=-45^\circ$ and 45° . A C-film ($n_o=1.5095$, $n_e=1.511$, and thickness $d=48\mu\text{m}$) and an A-film ($n_o=1.5095$, $n_e=1.511$, thickness $d=70\mu\text{m}$, and optical axis $\phi=0^\circ$) are laminated between the biaxial film 2 and the top coupling film. Figure 4.9(b) shows the compensation process of the dark state on Poincaré sphere. For an oblique incidence ($\theta=70^\circ$, $\phi=270^\circ$), the transmission state P_0 is on the absorption axis of the analyzer A_0 and we get good dark state. However, when the azimuthal angle changes, such as $\phi=315^\circ$, the polarization state P_1 and the absorption axis A_1 deviates from P_0 and A_0 . Biaxial film 1 does not change the polarization state P_0 at $\phi=270^\circ$ but can shift the polarization from P_1 to P_0 at $\phi=315^\circ$. Biaxial film 2 changes the linear polarization P_0 to circular C_1 and biaxial film 3 would change the circular light from C_1 to linear P_0 . The C-film and A-film are designed to

shift P_0 to A_3 via A_2 . Finally, the top coupling film and turning film would depolarize the light A_3 and move A_3 to A_1 ; the absorption axis of the analyzer. Figure 4.9(c) is a plot of the simulated isocontrast contours. The contours are improved noticeably because the polarizer and the analyzer exhibit larger extinction ratio at a small incident angle.

Figure 4.10 shows another example by laminating bottom coupling film on the polarizer. The absorption axis of the polarizer and the analyzer are at $\phi=0^\circ$ and 90° , respectively. Biaxial film 1 ($N_z=0.568$, $d(n_x-n_y)=209.6$ nm) is set at $\phi=0^\circ$. Identical biaxial films 2 and 3 ($N_z=0.501$, $d(n_x-n_y)=137.5$ nm) are set at $\phi=-45^\circ$ and 45° . A C-film ($n_o=1.5095$, $n_e=1.511$, and thickness $d=40\mu\text{m}$) and an A-film ($n_o=1.5095$, $n_e=1.511$, thickness $d=60\mu\text{m}$, and optical axis $\phi=0^\circ$) are laminated between the biaxial film 3 and the top coupling film. Figure 4.10(b) shows the compensation process on Poincaré sphere for the dark state, which is the same as Figure 4.10(b). Figure 4.10(c) is a plot of the simulated isocontrast contours. Because the backlight's incident angle inside the polarizer is larger in Figure 4.10 ($\theta\sim 70^\circ$) than that in Figure 4.9 ($\theta\sim 39^\circ$), Figure 4.10(c) shows smaller isocontrast contours than Figure 4.9(c).

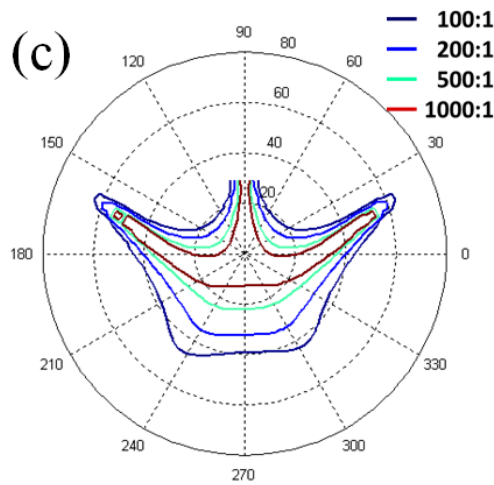
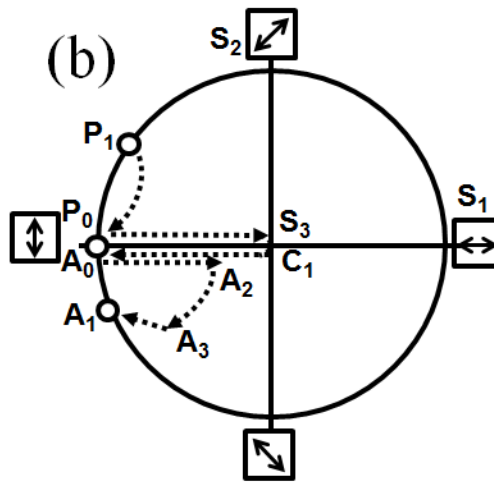
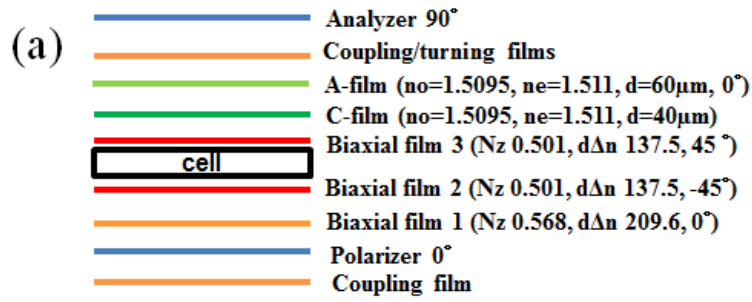


Figure 4.10 Film-compensated VFS BPLCD with bottom coupling film laminated to the polarizer: (a) film configuration, (b) compensation principle, and (c) simulated isocontrast contours.

Figure 4.11 shows another compensation process for dark state based on the same configuration as Figure 4.9. Here, biaxial film 1 ($N_z=0.756$ and $d(n_x-n_y)=254$ nm, and $\phi=0^\circ$) can compensate the polarization state from P_1 to P_0 for an azimuthal angle deviated from $\phi=270^\circ$. Biaxial film 2 ($N_z=0.6738$ and $d(n_x-n_y)=275$ nm, and $\phi=112.5^\circ$) shifts P_0 to P_2 . Biaxial film 3 ($N_z=0.9328$ and $d(n_x-n_y)=275$ nm, and $\phi=22.5^\circ$) shifts P_2 back to P_0 . A C-film ($n_o=1.5095$, $n_e=1.511$, and thickness $d=65\mu\text{m}$) plus an A-film ($n_o=1.5095$, $n_e=1.511$, $d=70\mu\text{m}$, and $\phi=0^\circ$) shift P_0 to P_4 . Finally, the depolarization by the coupling film and turning film would shift P_4 to A_1 . Figure 4.11(c) depicts the isocontrast contours optimized for the backlight at incident angle $\theta=70^\circ$, $\phi=270^\circ$. Figure 4.9(c) shows better isocontrast contours than Figure 4.11(c) because we chose circularly polarized light as the middle state in Figure 4.9 which is less sensitive to the azimuthal angle ϕ .

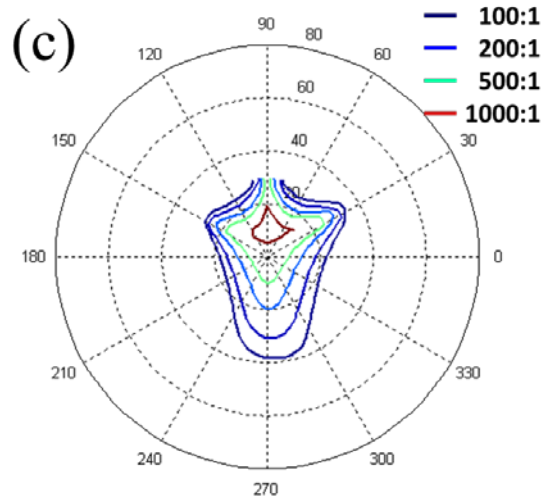
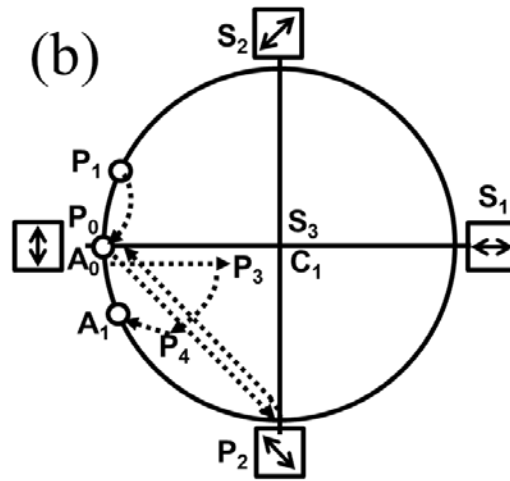
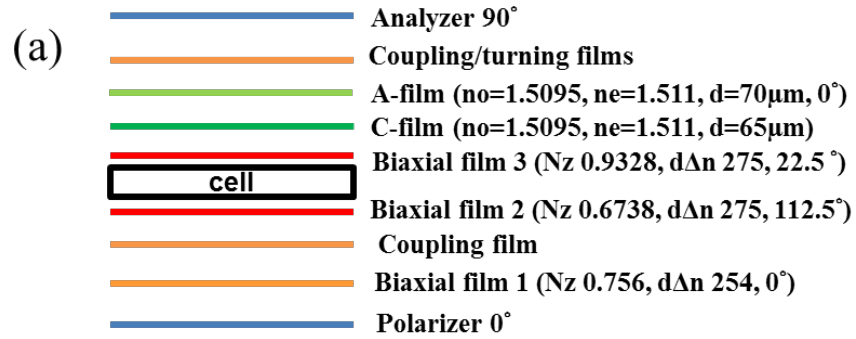


Figure 4.11 Another version of biaxial and A/C-films compensated VFS BPLCD: (a) film configuration, (b) compensation principle, and (c) simulated isocontrast contours.

4.3 Wire-Grid Polarizer for VFS BPLCDs

We also explore the compensation method using wire-grid polarizers (WGP) [67] instead of conventional dichroic sheet polarizer (Figure 4.12). Actually, a WGP can substitute conventional polarizer in all above discussed examples. Because a WGP retains a good extinction ratio at large incident angle (e.g., $\theta=70^\circ$), it helps to improve the CR. However, one shortcoming of WGP is that it reflects up to 50% of the ambient light which would degrade the CR. Thus, it is better to use WGP as the inner polarizer while keeping a sheet polarizer as the outer polarizer [68].

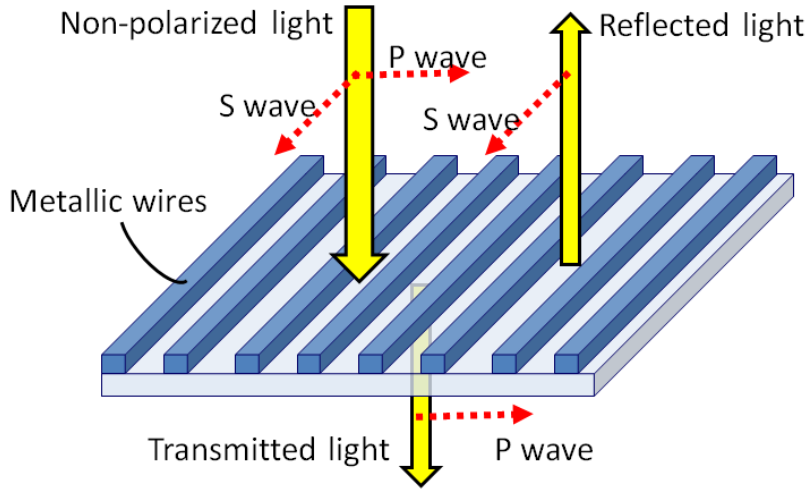


Figure 4.12 Schematic drawing of a wire-grid polarizer.

In Figure 4.13(a), we show a special case by setting the absorption axis of a WGP at $\phi=90^\circ$ and a dichroic sheet analyzer at $\phi=0^\circ$. Usually, we do not set the dichroic polarizer at $\phi=90^\circ$ because of its poor extinction ratio at an oblique incidence ($\theta=70^\circ$, $\phi=270^\circ$). The biaxial films 1 and 2 ($N_z=0.81$, $d(n_x-n_y)=317.35$ nm) are set at $\phi=0^\circ$ and 90° , and biaxial films 3 and 4 ($N_z=0.5$ and $d(n_x-n_y)=137$ nm) are at $\phi=45^\circ$ and -45° , respectively. Figure 4.13(b) shows the

compensation process of dark state by biaxial films on Poincaré sphere. When the oblique directional backlight ($\theta=70^\circ$, $\phi=270^\circ$) passes through a WGP, it becomes linearly polarized P_0 . Biaxial film 1 does not change the polarization state at $\phi=270^\circ$, but biaxial film 2 would shift the linear light from P_0 to circular C_1 . Biaxial film 3 would shift the circular light from C_1 to linear which is parallel to the absorption axis of the analyzer A_0 and biaxial film 4 does not change the polarization state. Therefore, we can get a good dark state at ($\theta=70^\circ$, $\phi=270^\circ$). However, as the azimuthal incident angle changes (e.g., $\theta=70^\circ$, $\phi=300^\circ$), the polarization state P_1 deviates from P_0 and the absorption axis A_1 deviates from A_0 . Biaxial film 1 can move P_1 back to P_0 at different azimuthal angle (e.g., from $\phi=225^\circ$ to $\phi=315^\circ$). Next, biaxial films 2 and 3 shift the polarization state from P_0 to P_2 via C_1 . Finally, biaxial film 4 reorients the linearly polarized light P_2 to be parallel to the absorption axis of the analyzer A_1 . As a result, the light leakage is suppressed substantially. From the isocontrast contours shown in Figure 4.13(c), the WGP is insensitive to the polar angle θ along $\phi=90^\circ/270^\circ$ and provides wide isocontrast contours along its absorption axis. This special characteristic allows us to adopt 2D light-distribution backlight and front diffuser [69].

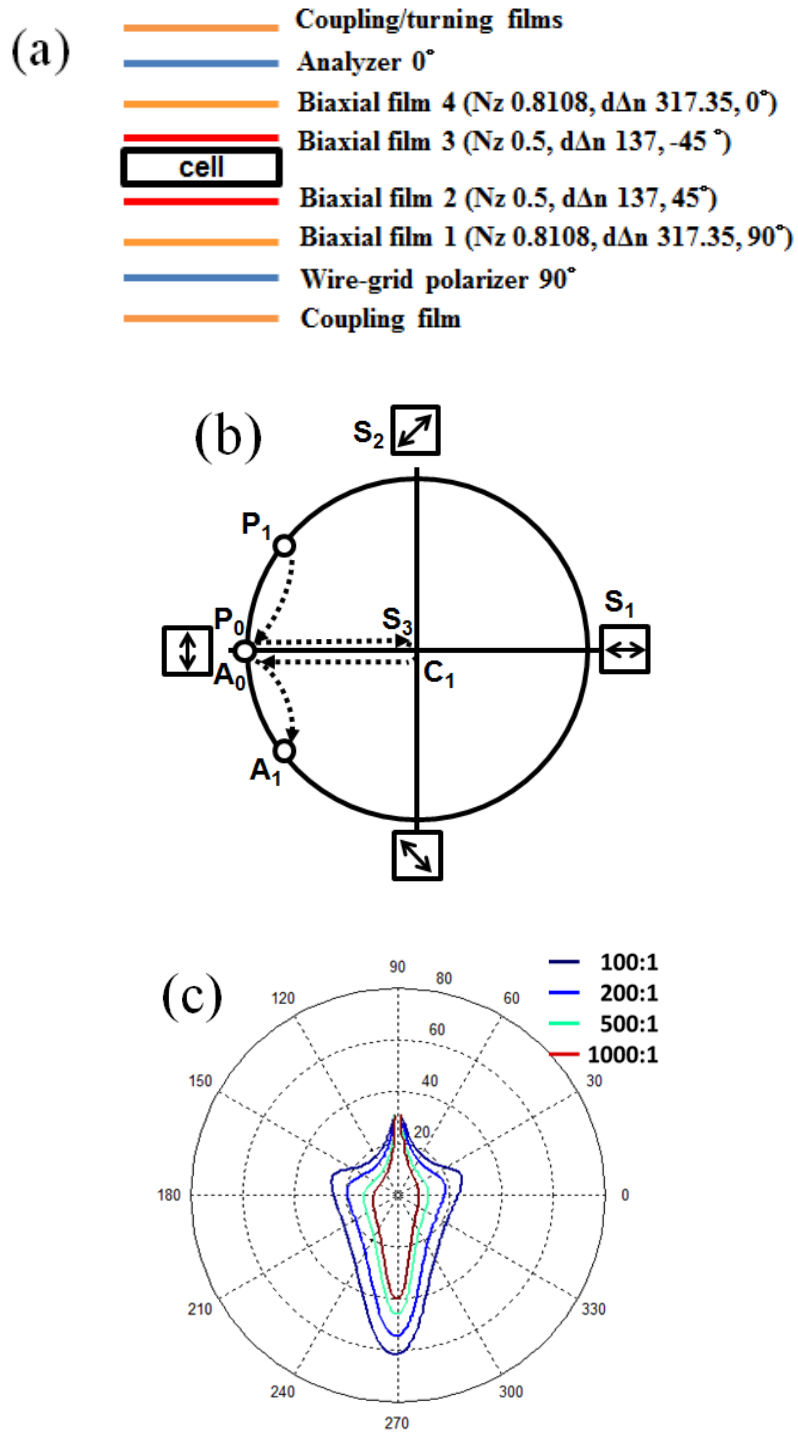


Figure 4.13 Optical configuration of the proposed VFS-BPLCD, (a) film configuration, (b) compensation principle, and (c) simulated isocontrast contours.

4.4 E-type Analyzer for VFS BPLCDs

The conventional LCDs adopt O-type analyzer in which ordinary ray is transmitted and extraordinary ray is strongly absorbed. For an O-type polarizer [Figure 4.14(a)], the extinction ratio for E-wave attenuates gradually as the incident plane is parallel to the c-axis and the polar angle increases. While in Figure 4.14(b), the E-type polarizer [70] [71] can preserve a large extinction ratio for O-wave at different polar angles as the incident plane is perpendicular to the c-axis. Therefore, the polarization purity remains reasonably good at large incident angles for E-type polarizer.

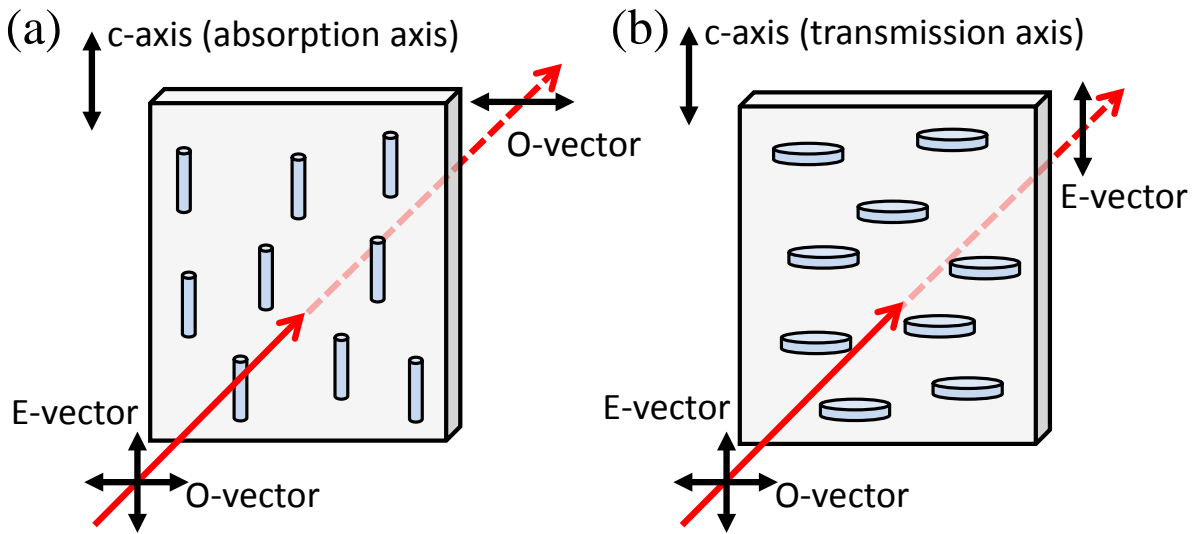


Figure 4.14 Schematic drawing of an (a) O-type polarizer and (b) E-type polarizer.

Here, we propose a new design by using E-type analyzer instead of O-type for VFS BPLCD. As shown in Figure 4.15(a), the absorption axis of a conventional O-type polarizer is along $\phi=0^\circ$. The c-axis (i.e., transmission axis) of an E-type analyzer is along $\phi=0^\circ$. Two biaxial

films 1 and 2 ($N_z=0.5$, $d(n_x-n_y)=137.5$ nm) are set at $\phi=-45^\circ$ and 45° .

Figure 4.15(b) shows the compensation process on Poincaré sphere for achieving dark state. The polarization state is always at P_0 for different polar angles while the oblique backlight ($\phi=270^\circ$) passing through the polarizer. The transmitted light P_0 is polarized along the absorption axis of the E-type analyzer and a good dark state is obtained. For an E-type analyzer, all the light polarized perpendicular to the c-axis will be absorbed. Therefore, the absorption axis can be represented by the red circle in Figure 4.15(b). For any incident light with azimuthal angle ϕ deviated from 270° , the transmitted state would shift from P_0 to another state, such as P , and is still on the red circle (i.e. absorption axis). Therefore, our configuration shows a good dark state which is insensitive to θ and ϕ . No additional retardation film is needed to compensate the light leakage at dark state for different polar and azimuthal angles. In order to improve the bright state at different viewing angles, we add biaxial film 1 to shift the linear polarization P_1 to circular C_1 . Biaxial film 2 shifts the circularly polarized light C_1 back to A_1 ; the absorption axis of analyzer. Figure 4.15(c) shows the simulated isocontrast contours optimized at incident angle ($\theta=70^\circ$, $\phi=270^\circ$). The E-type analyzer provides very wide isocontrast contours because it retains good extinction ratio for different θ and ϕ .

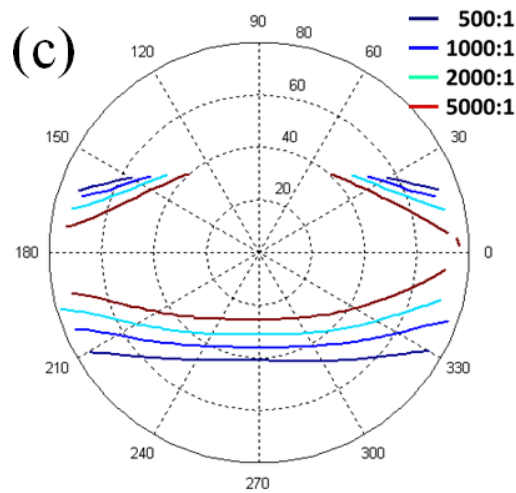
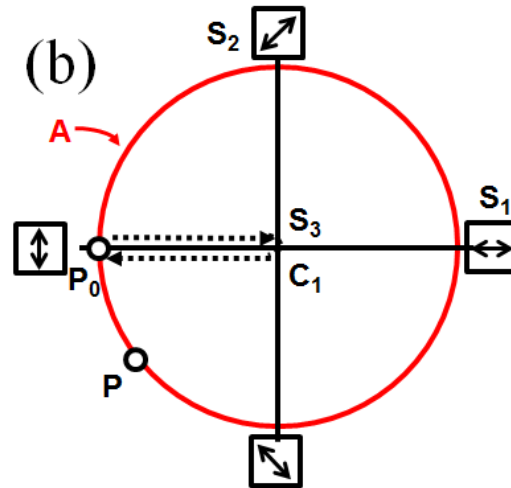
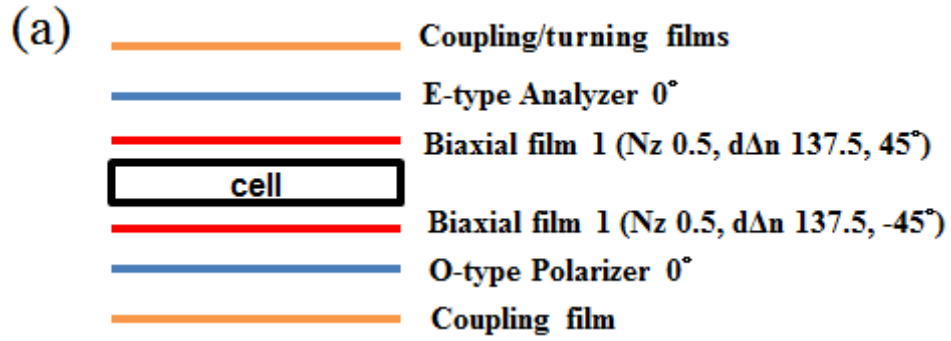


Figure 4.15 Proposed VFS BPLCD using an O-type polarizer and an E-type analyzer: (a) film configuration, (b) compensation principle, and (c) simulated isocontrast contours.

4.5 Discussions

We have proposed several device structures for improving the viewing angle of VFS BPLCD. With phase compensation films, we are able to enhance the intrinsic CR at normal direction and enlarge the isocontrast contours. Since VFS BPLCD uses a directional backlight (FWHM<20°), the high contrast contours should be larger than $\pm 10^\circ$ viewing cone. If the oblique backlight is more collimated (e.g., FWHM<10°), we could choose the simplest configuration with two biaxial films. Otherwise, we need more retardation films to obtain wider isocontrast contours. Reducing the incident angle of a directional backlight can also enlarge the isocontrast contours. However, we need BPLC material with a higher Kerr-constant or we should apply a higher operating voltage. The E-type analyzer shows the best performance for VFS BPLCD. However, the E-type analyzer is presently not available commercially. To achieve wide view, a front diffusor or curved turning film can also be considered. The high contrast images are steered or diffused to different viewing directions. This kind of surface-diffusion LCD [65] helps to eliminate color shift and gray level inversion at different viewing angle.

CHAPTER 5: SUMMARY

We investigate and study the principles of multi-primary displays. From our results, multi-primaries (RGBYC) can enlarge the color gamut to have a better color reproduction and also enhance the brightness of the display.

We also applied the five-primary theorem on the FSC LCDs. We propose a method and algorithm to reduce the CBU by using an optimized color ratio and order. Without increasing the frame rate, we can reduce the CBU and keep the advantages of multi-primaries.

In order to totally suppress the CBU and motion blur of FSC LCDs, it is necessary to enhance the frame rates of sequential color images. Higher frame rates would require a very fast response time of liquid crystal ($< 1\text{ms}$). PS-BPLC shows potential in FSC LCDs because of its submillisecond response time. However, large operating voltage of BPLC is always a big issue for TFT addressing by using the conventional planar IPS structure. Protruded IPS can help to reduce the voltage, but the hysteresis and residual birefringence still exists. Moreover, protruded IPS makes the manufacturing much more difficult and the record low voltage ($\sim 27\text{ V}_{\text{rms}}$) still needs to be further reduced.

We propose a novel device design of VFS BPLCD. We have investigated the device physics and electro-optical properties. The main research discoveries and achievements are as follows:

1. VFS mode offers several superior performances to IPS or other proposed structures. First, we reduce the operating voltage to 16 V_{rms} in our experiment and estimate the operating voltage can be lower to 10 V_{rms} by optimizing cell gap which enables BPLCD for TFT addressing. Second, we solve the problem of hysteresis for PSBPLC material. As

compared to other methods with serious hysteresis, VFS has much lower driving voltage so that the hysteresis becomes negligible. A hysteresis-free device is very important when showing the correct grayscale in display applications. Third, we observed no residual birefringence which was reported in other driving methods for BPLCD. The residual birefringence will cause light leakage in the dark state and degrade the contrast ratio of the BPLCD. Fourth, from our measurement, VFS reveals faster response time than IPS BPLCD. IPS shows very slow response time in the low gray level transition. VFS shows fast response time in both low and high gray level transitions.

2. VFS cell provides a reliable way to determine the property of BPLC material. In fact, the electric field direction and intensity is not uniform in the IPS cell. We can only measure the average BPLC molecular orientation under different electric fields. It is not easy and precise to locally analyze the interaction between the BPLC molecule and a specific electric field in an IPS cell. Since VFS cell has uniform fields inside, its electro-optic property should also be uniform. Using a VFS cell, we are able to establish correlation between hysteresis and electric fields. We define a critical electric field for a hysteresis-free device. Below this critical field, hysteresis is negligible. When the applied field is larger than the critical field, the deformation of polymer network also causes the slow response time. This critical field is dependent on the strength and stability of the polymer networks.
3. Unlike IPS, the operation voltage of a VFS cell is cell gap sensitive. Therefore, we can get an optimized cell gap for achieving minimum operation voltage. From our measured results and calculations, we estimate the driving voltage should be lower than $10 V_{\text{rms}}$ if

the cell gap is $\sim 3 \mu\text{m}$. We also derived the analytical solution for the optimized cell gap, and studied the relation between incident angle and operation voltage.

VFS cell structure is very simple, but it requires sophisticated phase compensation scheme to achieve wide view. We design and optimize the dual biaxial films to enhance the intrinsic contrast ratio of VFS cell. We also propose to use wire-grid polarizer or E-type analyzer to get a better performance. In order to steer the directional backlight to multiple directions, we propose to add a front diffuser or use curve shaped prism film to get a wide viewing angle. This surface-diffusion display has less color shift and gray level inversion as compared to the conventional LCDs.

Overall, VFS overcomes most of the problems encountered in IPS BPLCDs and the cell structure is simple for manufacturing. It is particularly attractive for display and photonic devices that require fast response time, such as FSC LCDs using RGB LED backlight, or 3D displays. We believe our work will make an important impact on the display technologies and VFS BPLCDs would be a strong competitor in the next generation.

LIST OF REFERENCES

- [1] J. H. Lee, D. N. Liu, and S. T. Wu, "Introduction to Flat Panel Displays," *New York: Wiley*, 2008.
- [2] P. Yeh and C. Gu, "Optics of Liquid Crystal Displays," *Wiley, New York*, 1999.
- [3] D. K. Yang and S. T. Wu, "Fundamentals of Liquid Crystal Devices," *Wiley, New York*, 2006, 2006.
- [4] R. A. Soref, "Field Effects in Nematic Liquid-Crystals Obtained with Interdigital Electrodes," *Journal of Applied Physics*, vol. 45, pp. 5466-5468, 1974.
- [5] M. Ohe, M. Yoneya, and K. Kondo, "Switching of negative and positive dielectro-anisotropic liquid crystals by in-plane electric fields," *Journal of Applied Physics*, vol. 82, pp. 528-535, Jul 15 1997.
- [6] S. H. Lee, S. L. Lee, and H. Y. Kim, "Electro-optic characteristics and switching principle of a nematic liquid crystal cell controlled by fringe-field switching," *Applied Physics Letters*, vol. 73, pp. 2881-2883, Nov 16 1998.
- [7] G. Hollemann, B. Braun, P. Heist, J. Symanowski, and U. Krause, "High-power laser projection displays," *Proc. SPIE*, 2001, vol. 4294, pp. 36-46, 2001.
- [8] K. V. Chellappan, E. Erden, and H. Urey, "Laser-based displays: a review," *Applied Optics*, vol. 49, pp. F79-F98, Sep 1 2010.
- [9] G. Harbers and C. Hoelen, "High Performance LCD Backlighting using High Intensity Red, Green and Blue Light Emitting Diodes," *SID Dig. Tech. papers*, vol. 32, pp. 702-705, 2001.

- [10] R. Lu, Q. Hong, Z. B. Ge, and S. T. Wu, "Color shift reduction of a multi-domain IPS-LCD using RGB-LED backlight," *Optics Express*, vol. 14, pp. 6243-6252, Jun 26 2006.
- [11] R. B. Lu, S. Gauza, and S. T. Wu, "LED-lit LCD TVs," *Molecular Crystals and Liquid Crystals*, vol. 488, pp. 246-259, 2008.
- [12] T. Igarashi, T. Kusunoki, and K. Ohno, "A new CCFL for wide-color-gamut LCD TV," *Proc. EuroDisplay*, pp. 233-236, 2005.
- [13] T. Ajito, T. Obi, M. Yamaguchi, and N. Ohyama, "Expanding color gamut reproduced by six-primary projection display," *Proc. SPIE*, vol. 3954, pp. 130-137, 2000.
- [14] E. Chino, K. Tajiri, H. Kawakami, H. Ohira, K. Kamijo, H. Kaneko, S. Kato, Y. Ozawa, T. Kurumisawa, K. Inoue, K. Endo, H. Moriya, T. Aragaki, and K. Murai, "Development of wide-Color-Gamut Mobile Displays with Four primary-color LCDs," *SID Dig. Tech. Papers*, vol. 37, pp. 1221-1224, 2006.
- [15] Y. C. Yang, K. Song, S. G. Rho, N. S. Rho, S. J. Hong, K. B. Deul, M. Hong, K. Chung, W. H. Choe, S. Lee, C. Y. Kim, S. H. Lee, and H. R. Kim, "Development of six primary-color LCD," *SID Dig. Tech. Papers*, vol. 36, pp. 1210-1213, 2005.
- [16] H. Sugiura, H. Kaneko, S. Kagawa, M. Ozawa, H. Tanizoe, H. Katou, T. Kimura, and H. Ueno, "Improved six-primary-color 23-in. WXGA LCD using six-color LEDs," *SID Dig. Tech. Papers*, vol. 36, pp. 1126-1129, 2005.
- [17] S. Ueki, K. Nakamura, Y. Yoshida, T. Mori, K. Tomizawa, Y. Narutaki, Y. Itoh, and K. Okamoto, "Five-primary-color 60-inch LCD with novel wide color gamut and wide viewing angle," *SID Dig. Tech. Papers*, vol. 40, pp. 927-930, 2009.
- [18] S. Roth, N. Weiss, M. Ben-Chorin, I. Ben-David, and C. H. Chen, "Multi-primary LCD

- for TV applications," *SID Dig. Tech. Papers*, vol. 38, pp. 34-37, 2007.
- [19] M. F. Schiekkel and Fahrensc.K, "Deformation of Nematic Liquid Crystals with Vertical Orientation in Electrical Fields," *Applied Physics Letters*, vol. 19, pp. 391-&, 1971.
 - [20] A. Takeda, S. Kataoka, T. Sasaki, H. Chida, H. Tsuda, K. Ohmuro, Y. Koike, T. Sasabayashi, and K. Okamoto, "A Super-High-Image-Quality Multi-Domain Vertical Alignment LCD by New Rubbing-Less Technology," *SID Symposium Digest*, vol. 29, pp. 1077-1079, 1998.
 - [21] P. Green and L. MacDonald, "Colour Engineering," *New York: Wiley*, 2002.
 - [22] S. Roth, I. Ben-David, M. Ben-Chorin, D. Eliav, and O. Ben-David, "Wide gamut, high brightness multiple primaries single panel projection displays," *SID Dig. Tech. Papers*, vol. 34, pp. 118-121, 2003.
 - [23] M. F. Weber, C. A. Stover, L. R. Gilbert, T. J. Nevitt, and A. J. Ouderkirk, "Giant birefringent optics in multilayer polymer mirrors," *Science*, vol. 287, pp. 2451-2456, Mar 31 2000.
 - [24] Y. Li, T. X. Wu, and S. T. Wu, "Design Optimization of Reflective Polarizers for LCD Backlight Recycling," *Journal of Display Technology*, vol. 5, pp. 335-340, Aug 2009.
 - [25] F. Yamada, H. Nakamura, Y. Sakaguchi, and Y. Taira, "Sequentialcolor LCD based on OCB with an LED backlight," vol. 10, pp. 81-85, 2002.
 - [26] J. H. Lee, X. Y. Zhu, and S. T. Wu, "Novel color-sequential transfective liquid crystal displays," *Journal of Display Technology*, vol. 3, pp. 2-8, Mar 2007.
 - [27] S. Gauza, X. Zhu, W. Piecek, R. Dabrowski, and S. T. Wu, "Fast switching liquid crystals for color-sequential LCDs," *Journal of Display Technology*, vol. 3, pp. 250-252, Sep

2007.

- [28] L. Arend, J. Lubin, J. Gille, and J. Larimer, "Color breakup in sequentially scanned LCDs," *SID Symp. Dig. Tech. Papers*, vol. 25, pp. 201-204, 1994.
- [29] S. T. Wu, "Nematic Liquid-Crystal Modulator with Response-Time Less Than 100- μ s at Room-Temperature," *Applied Physics Letters*, vol. 57, pp. 986-988, Sep 3 1990.
- [30] Z. B. Ge, L. H. Rao, S. Gauza, and S. T. Wu, "Modeling of Blue Phase Liquid Crystal Displays," *Journal of Display Technology*, vol. 5, pp. 250-256, Jul 2009.
- [31] Z. B. Ge, S. Gauza, M. Z. Jiao, H. Q. Xianyu, and S. T. Wu, "Electro-optics of polymer-stabilized blue phase liquid crystal displays," *Applied Physics Letters*, vol. 94, Mar 9 2009.
- [32] K. M. Chen, S. Gauza, H. Q. Xianyu, and S. T. Wu, "Submillisecond Gray-Level Response Time of a Polymer-Stabilized Blue-Phase Liquid Crystal," *Journal of Display Technology*, vol. 6, pp. 49-51, Feb 2010.
- [33] M. Mori, T. Hatada, K. Ishikawa, T. Saishouji, O. Wada, J. Nakamura, and N. Terashima, "Mechanism of color breakup in field-sequential color projectors," *J. SID*, vol. 7, pp. 257-259, 1999.
- [34] H. Yamakita, M. Sakai, Y. Taniguchi, J. Asayama, and K. Adachi, "Field-sequential color LCD driven by optimized method for color breakup reduction," *Int. Display Workshop*, vol. 12, pp. 83-86, 2005.
- [35] K. Sekiya, T. Miyashita, and T. Uchida, "A simple and practical way to cope with color breakup on field sequential color LCDs," *SID Symp. Dig. Tech. Papers*, pp. 1661-1664, 2006.

- [36] N. Koma and T. Uchida, "A new field-sequential-color LCD without moving-object color break-up," *J. Soc. Inf. Display*, vol. 11, pp. 413-417, 2003.
- [37] C. H. Chen, F. C. Lin, Y. T. Hsu, Y. P. Huang, and H. P. D. Shieh, "A Field Sequential Color LCD Based on Color Fields Arrangement for Color Breakup and Flicker Reduction," *Journal of Display Technology*, vol. 5, pp. 34-39, Jan-Mar 2009.
- [38] F. C. Lin, Y. P. Huang, C. M. Wei, and H. P. Shieh, "Color-breakup suppression and low-power consumption by using the Stencil FSC method in field-sequential LCDs," *J. Soc. Inf. Display*, vol. 17, pp. 221-227, 2007.
- [39] H. C. Cheng, I. Ben-David, and S. T. Wu, "Five-Primary-Color LCDs," *Journal of Display Technology*, vol. 6, pp. 3-7, Jan 2010.
- [40] E. Langendijk, S. Swinkels, D. Eliav, and M. Chorin, "Suppression of color breakup in color-sequential multiprimary projection displays," *J. Soc. Inf. Display*, vol. 14, pp. 325-329, 2006.
- [41] H. Kikuchi, M. Yokota, Y. Hisakado, H. Yang, and T. Kajiyama, "Polymer-stabilized liquid crystal blue phases," *Nature Materials*, vol. 1, pp. 64-68, Sep 2002.
- [42] Y. Haseba, H. Kikuchi, T. Nagamura, and T. Kajiyama, "Large electro-optic Kerr effect in nanostructured chiral liquid-crystal composites over a wide temperature range," *Advanced Materials*, vol. 17, pp. 2311-+, Oct 4 2005.
- [43] J. Yan, L. H. Rao, M. Z. Jiao, Y. Li, H. C. Cheng, and S. T. Wu, "Polymer-stabilized optically isotropic liquid crystals for next-generation display and photonics applications," *Journal of Materials Chemistry*, vol. 21, pp. 7870-7877, 2011.
- [44] G. Heppke, H. S. Kitzerow, and M. Krumrey, "Electric-Field Induced Variation of the

- Refractive-Index in Cholesteric Blue Phases," *Molecular Crystals and Liquid Crystals*, vol. 2, pp. 59-65, 1985.
- [45] L. H. Rao, Z. B. Ge, S. T. Wu, and S. H. Lee, "Low voltage blue-phase liquid crystal displays," *Applied Physics Letters*, vol. 95, Dec 7 2009.
 - [46] M. Sato and A. Yoshizawa, "Electro-optical switching in a blue phase III exhibited by a chiral liquid crystal oligomer," *Advanced Materials*, vol. 19, pp. 4145-+, Dec 3 2007.
 - [47] K. M. Chen, S. Gauza, H. Q. Xianyu, and S. T. Wu, "Hysteresis Effects in Blue-Phase Liquid Crystals," *Journal of Display Technology*, vol. 6, pp. 318-322, Aug 2010.
 - [48] M. Kim, M. S. Kim, B. G. Kang, M. K. Kim, S. Yoon, S. H. Lee, Z. B. Ge, L. H. Rao, S. Gauza, and S. T. Wu, "Wall-shaped electrodes for reducing the operation voltage of polymer-stabilized blue phase liquid crystal displays," *Journal of Physics D-Applied Physics*, vol. 42, Dec 7 2009.
 - [49] L. H. Rao, H. C. Cheng, and S. T. Wu, "Low Voltage Blue-Phase LCDs With Double-Penetrating Fringe Fields," *Journal of Display Technology*, vol. 6, pp. 287-289, Aug 2010.
 - [50] M. Z. Jiao, Y. Li, and S. T. Wu, "Low voltage and high transmittance blue-phase liquid crystal displays with corrugated electrodes," *Applied Physics Letters*, vol. 96, Jan 4 2010.
 - [51] H. C. Cheng, J. Yan, T. Ishinabe, and S. T. Wu, "Vertical field switching for blue-phase liquid crystal devices," *Applied Physics Letters*, vol. 98, Jun 27 2011.
 - [52] Y. H. Kim, S. T. Hur, C. S. Park, K. W. Park, S. W. Choi, S. W. Kang, and H. R. Kim, "A vertical-field-driven polymer-stabilized blue phase liquid crystal mode to obtain a higher transmittance and lower driving voltage," *Optics Express*, vol. 19, pp. 17427-17438, Aug

29 2011.

- [53] H. C. Cheng, J. Yan, T. Ishinabe, N. Sugiura, C. Y. Liu, T. H. Huang, C. Y. Tsai, C. H. Lin, and S. T. Wu, "Blue-Phase Liquid Crystal Displays With Vertical Field Switching," *Journal of Display Technology*, vol. 8, pp. 98-103, Feb 2012.
- [54] M. Oe and I. Chiba, "Plane light source unit," *US Patent 5126882*, 1992.
- [55] K. Kälantär, "A monolithic segmented functional light guide for 2-D dimming LCD backlight," *J. Soc. Inf. Display*, vol. 19, pp. 37-47, 2011.
- [56] L. H. Rao, J. Yan, S. T. Wu, S. I. Yamamoto, and Y. Haseba, "A large Kerr constant polymer-stabilized blue phase liquid crystal," *Applied Physics Letters*, vol. 98, Feb 21 2011.
- [57] H. Lee, H. J. Park, O. J. Kwon, S. J. Yun, J. H. Park, S. Hong, and S. T. Shin, "The world's first blue phase liquid crystal display," *SID Symposium Digest*, vol. 42, pp. 122-125, 2011.
- [58] J. Yan, H. C. Cheng, S. Gauza, Y. Li, M. Z. Jiao, L. H. Rao, and S. T. Wu, "Extended Kerr effect of polymer-stabilized blue-phase liquid crystals," *Applied Physics Letters*, vol. 96, Feb 15 2010.
- [59] M. Z. Jiao, J. Yan, and S. T. Wu, "Dispersion relation on the Kerr constant of a polymer-stabilized optically isotropic liquid crystal," *Physical Review E*, vol. 83, Apr 11 2011.
- [60] X. Y. Zhu, Z. B. Ge, and S. T. Wu, "Analytical Solutions for Uniaxial-Film-Compensated Wide-View Liquid Crystal Displays," *Journal of Display Technology*, vol. 2, pp. 2-20, Mar 2006.
- [61] H. Takemoto, T. Fuchida, S. Shutou, and M. Miyatake, "The performance of collimated

- backlight and front diffusing systems on several LC modes," *Proc. IDW' 09*, pp. 1907-1908, 2009.
- [62] G. Chidichimo, G. Arabia, A. Golemme, and J. W. Doane, "Electrooptic Properties of Polymer Dispersed Liquid-Crystals," *Liquid Crystals*, vol. 5, pp. 1443-1452, 1989.
- [63] C. D. Sheraw, L. Zhou, J. R. Huang, D. J. Gundlach, T. N. Jackson, M. G. Kane, I. G. Hill, M. S. Hammond, J. Campi, B. K. Greening, J. Francl, and J. West, "Organic thin-film transistor-driven polymer-dispersed liquid crystal displays on flexible polymeric substrates," *Applied Physics Letters*, vol. 80, pp. 1088-1090, Feb 11 2002.
- [64] X. Y. Zhu, Z. B. Ge, and S. T. Wu, "Analytical Solutions for Uniaxial-Film-Compensated Wide-View Liquid Crystal Displays (vol 2, pg 2, 2006)," *Journal of Display Technology*, vol. 2, pp. 312-312, Sep 2006.
- [65] K. Nakamura, T. Fuchida, K. Yamagata, A. Nishimura, T. Takita, and H. Takemoto, "Optical design of front diffuser for collimated backlight and front diffusing system," *Proc. IDW*, pp. 475-477, 2011.
- [66] M. Wittek, N. Tanaka, D. Wilkes, M. Bremer, D. Pauluth, M. K. Memmer, J. Canisius, A. Yeh, R. Yan, and K. Skjonnemand, "New materials for polymer-stabilized blue phase," *SID Symp. Dig.*, vol. xx, pp. xx-xx, 2012.
- [67] S. W. Ahn, K. D. Lee, J. S. Kim, S. H. Kim, J. D. Park, S. H. Lee, and P. W. Yoon, "Fabrication of a 50 nm half-pitch wire grid polarizer using nanoimprint lithography," *Nanotechnology*, vol. 16, pp. 1874-1877, Sep 2005.
- [68] Z. B. Ge and S. T. Wu, "Nanowire grid polarizer for energy efficient and wide-view liquid crystal displays," *Applied Physics Letters*, vol. 93, Sep 22 2008.

- [69] M. Nishizawa, K. Kusama, K. Sekiya, B. Katagiri, T. Kawakami, and T. Uchida, "Investigation of novel diffuser films for 2D light-distribution control," *Proc. IDW*, pp. 1385-1388, 2011.
- [70] Y. Bobrov and V. Novak, "Determination of anisotropic complex refractive indices of thin film e-polarizers," *Molecular Materials*, vol. 14, pp. 21-31, 2001.
- [71] P. I. Lazarev and M. V. Paukshto, "Low-leakage off-angle in E-polarizers," *J. Soc. Inf. Display*, vol. 9, pp. 101-105, 2001.

LIST OF PUBLICATIONS

Journal Publications:

- [1] H. C. Cheng, J. Yan, T. Ishinabe, C. H. Lin, K. H. Liu, and S. T. Wu, “Improving the viewing angle of a vertical field switching blue-phase LCD,” *J. Display Technol.* **8**, xx-xx (submitted, May 2012).
- [2] S. He, J. H. Lee, H. C. Cheng, J. Yan, and S. T. Wu, “Fast-response blue-phase liquid crystal for color sequential displays,” *J. Display Technol.* **8**, 352-356 (June, 2012).
- [3] H. C. Cheng, and S. T. Wu, “Sunlight readable transmissive LCDs,” *J. Display Technol.* **8**, pp. 183-185 (2012).
- [4] H. C. Cheng, J. Yan, T. Ishinabe, N. Sugiura, C. Y. Liu, T. H. Huang, C. Y. Tsai, C. H. Lin, and S. T. Wu, “Blue-phase liquid crystal displays with vertical field switching,” *J. Display Technol.* **8**, pp. 98-103 (2012).
- [5] H. C. Cheng, J. Yan, T. Ishinabe, and S. T. Wu, “Vertical field switching for blue-phase liquid crystal devices,” *Appl. Phys. Lett.* **98**, 261102 (June 27, 2011).
- [6] J. Yan, L. Rao, M Jiao, Y. Li, H. C. Cheng, and S. T. Wu, “Polymer-stabilized optically isotropic liquid crystals for next-generation display and photonics applications,” (Feature article) *J. Mater. Chem.* **21**, 7870-7877 (May, 2011).
- [7] H. C. Cheng, S. Xu, Y. Liu, S. Levi, and S. T. Wu, “Adaptive mechanical-wetting lens actuated by ferrofluids,” *Opt. Commun.* **284**, 2118-2121 (April 15, 2011).
- [8] Linghui Rao, H. C. Cheng, and S. T. Wu, “Low voltage blue-phase LCDs with double-penetrating fringe fields,” *J. Display Technol.* **6**, pp. 287-289 (2010).

- [9] H. C. Cheng, L. Rao, and S. T. Wu, "Color breakup suppression in field-sequential five-primary-color LCDs," *J. Display Technol.* 6, pp. 229-234 (2010).
- [10] J. Yan, H. C. Cheng, S. Gauza, Y. Li, M. Jiao, L. Rao, and S. T. Wu, "Extended Kerr effect of polymer-stabilized blue-phase liquid crystals," *Appl. Phys. Lett.* 96, 071105 (2010).
- [11] H. C. Cheng, I. Ben-David, and S. T. Wu, "Five-primary-color LCDs," *J. Display Technol.* 6, pp. 3-7 (2010).

Conference Proceedings:

- [1] H. C. Cheng, J. Yan, T. Ishinabe, C. Y. Tsai, C. H. Lin, T. H. Huang, K.H. Liu, C.Y. Liu, N. Sugiura, W. L. Liao, and S. T. Wu, "Low-voltage and hysteresis-free blue-phase LCD with vertical field switching," *SID Symposium Digest*, vol. 43, pp. 15-17, 2012.
- [2] S. He, J. H. Lee, J. Yan, H. C. Cheng, C. Y. Tsai, C. H. Lin, T. H. Huang, K.H. Liu, C.Y. Liu, N. Sugiura, W. L. Liao, and S. T. Wu, "Submillisecond-response blue-phase liquid crystal for color sequential projection displays," *SID Symposium Digest*, vol. 43, pp. 918-921, 2012.
- [3] H. C. Cheng, J. Yan, T. Ishinabe, and S. T. Wu, "A low voltage and hysteresis-free blue-phase LCD," *Proc. of Electronic Displays Conference*, 2012.
- [4] H. C. Cheng, J. Yan, T. Ishinabe, and S. T. Wu, "The dawn of blue-phase liquid crystal displays," *Proc. of IDW*, pp. 21-24, 2011.
- [5] J. Yan, H. C. Cheng, L. Rao, T. Ishinabe and S. T. Wu, "Emerging polymer-stabilized blue phase liquid crystal display," *Proc. of China Display/Asia Display*, pp. 69-72, 2011.
- [6] H. C. Cheng, J. Yan, T. Ishinabe, Y. R. Chuang, C. H. Lin, and S. T. Wu, "A low voltage and

- hysteresis-free blue-phase LCD,” *Proc. of IMID*, pp. 263-264, 2011.
- [7] H. C. Cheng, and S. T. Wu, “Sunlight readable transmissive LCDs,” *SID Symposium Digest*, vol. 42, pp. 1711-1713, 2011.
- [8] J. Yan, H. C. Cheng, S. Gauza, Y. Li, M. Jiao, L. Rao, and S. T. Wu, "Extended Kerr effect in a polymer-stabilized blue-phase liquid crystal composite," *SID Symposium Digest*, vol. 41, pp. 87-89, 2010.
- [9] H. C. Cheng, and S. T. Wu, “Color breakup suppression in field-sequential five-primary-color LCDs,” *SID Symposium Digest*, vol. 41, pp. 152-154, 2010.

Patents:

- [1] H. C. Cheng, J. Yan, T. Ishinabe, C. H Lin, K.H. Liu, and S. T. Wu, “Display devices”, US Patent Pending (2012).
- [2] H. C. Cheng, J. Yan, T. Ishinabe, Y. R. Chuang, C. H. Lin, and S. T. Wu, “ Vertical field switching for optically-isotropic liquid crystal displays”, US Patent Pending (2011).
- [3] H. C. Cheng, Z. Ge, S. T. Wu, W.Y. Li, and C. K. Wei, “Transmissive LCD with reflective mode”, US Patent Pending (2009).